Dechanneling of 2 MeV He^+ in Gold

D. R. Wright

Department of Physics

A Thesis

submitted in partial fulfillment

of the requirements for the degree of

Master of Science

Brock University

St. Catharines, Ontario, Canada

February 1978

ABSTRACT

Thick gold single crystals of high quality were prepared for Rutherford Backscattering Dechanneling studies by electropolishing and annealing. The variation with temperature of the Random Fraction versus Depth spectrum for 2 MeV He^+ on $\langle 110 \rangle$ gold was extracted from measured Aligned and Random (Energy) Spectra. The measured dechanneling rate showed a sixfold increase in going from 41°K to 293°K and is in reasonable agreement with calculations made using the Steady Increase in Transverse Energy (SITE) approximation.

ACKNOWLEDGEMENTS

I would like to thank my thesis supervisor, Dr. J. A. Moore, for his guidance and exceptional patience throughout this project.

It is also a pleasure to thank Janet Hastie, for typing this thesis with great speed and accuracy; Vicki Migus, for assistance with the diagrams; the technical staff at the McMaster University electron microscope; everyone at the Solid State Physics branch of Chalk River Nuclear Laboratories, for advice and assistance with the dechanneling measurements; J. F. Ziegler and H. H. Andersen, for communicating their recent Stopping Power data; M. L. Swanson and J. A. Davies, for supplying the thick gold single crystals. Special thanks are due to J. Lori at C. R. N. L. for his expert maintenance of the channeling facility throughout our round-the-clock experiments.

Financial support for this project was received from the National Research Council of Canada and is greatly appreciated.

To

My Parents

TABLE OF CONTENTS

LIST OF DIAGRAMS AND PLATES

LIST OF TABLES

CHAPTER ONE

INTRODUCTION

I.1 THE CHANNELING EFFECT

When a beam of energetic particles (e.g., MeV He^+ or H^+) is incident on a single crystal target, the depth of penetration of the beam and the yield of physical processes, requiring small impact parameters, are found to be strongly dependent on the relative orientation of the single crystal with the beam direction. This is known as the Channeling Effect. Many instances of this effect were discovered in the early 1960's. For example, when a beam of energetic particles was incident along low-index directions or planes of a single crystal, it was found that the yield of atoms ejected or "sputtered" from the target decreased sharply[1]; the particles in the beam penetrated the target to anomalously large depths[2-6] and had lower energy losses on traversing the crystal[7]; the nuclear reaction yield for (p,γ) reactions in silicon[8] and for (p, n) reactions in Cu[9] dropped sharply. The reduction in yield is considerable. For 2.0 MeV He^+ particles incident on the <110> direction in gold, the Rutherford Back-scattering yield from the surface of the crystal is 2%-3% of that from an amorphous gold target. The channeling effect requires that the beam direction be within approximately 1° of the crystal axis or plane direction. A recent review of channeling phenomena, containing an extensive bibliography, has been given by Gemmell[10].

The Channeling Effect has been applied frequently to defect studies in crystals. For example, in an ion-implanted material, it is possible to

measure the location of the impurity atoms within the unit cell and the concentration of displaced atoms caused by the ion implantation damage[11-13].

I.2 THE CONTINUUM POTENTIAL

Lindhard[14] has given a comprehensive theoretical analysis of the Channeling Effect, in which he describes the axially channeled particle as one which travels almost parallel to the crystal axis, making a series of correlated glancing collisions with a row or "string" of target atoms. The channeled particle is steered between the rows and prevented from making small impact parameter (0.1 Å) collisions with the row atoms. A good approximation to the motion of the channeled particle moving swiftly past a string of atoms is given by using a Continuum Potential U(r), which is calculated (see Appendix A) by averaging the periodic string potential along the z-direction parallel to the string of atoms. U(r) may be expressed in terms of the interatomic potential, $V(\rho)$, between the particle and a string atom, i.e.,

$$U(r) = \frac{1}{d}\int_{-\infty}^{\infty} V(\rho)dz,$$

where d is the spacing between string atoms,

r is the distance from the particle to the string, and

$\rho^2 = r^2 + z^2$.

U(r) is independent of z. Therefore the channeled particle will only experience a force transverse to the string direction, which will tend to repel it towards the centre of the channel, and so prevent the occurrence of small impact parameter collisions with string atoms. Lindhard gives the Continuum Potential as

$$U(r) = \frac{2Z_1Z_2e^2}{4\pi\epsilon_0 d} \cdot \chi\left(\frac{r}{a}\right),$$

with the screening function

$$\chi\left(\frac{r}{a}\right) = \frac{1}{2} \ln\left(\frac{C^2a^2}{r^2} + 1\right),$$

where a is the Thomas-Fermi screening length of the ion-atom interaction, i.e.,

$$a = 0.8853 \cdot a_0 (Z_1^{2/3} + Z_2^{2/3})^{-1/2}$$

where a_0 is the Bohr radius, and

C is a fitting parameter for the screening;

$C = \sqrt{3}$ is found to give a good over-all fit.

I.3 CONSERVATION OF TRANSVERSE ENERGY

If inelastic energy losses are neglected, the total energy, E, of a channeled particle is conserved and, within the continuum potential approximation, the velocity component v_z is constant. Therefore we may simply consider the motion in the plane transverse to the channel axis.

$$E = K_{\parallel} + K_{\perp} + U(r) = \text{constant} \qquad (I.1)$$

where $K_{\parallel}$ is the component of kinetic energy parallel to the string,

$K_{\perp}$ is the component of kinetic energy perpendicular to the string,

and U(r) is the potential energy of the particle.

Since v_z is constant, $K_{\parallel}$ is constant. Therefore $K_{\perp} + U(r) = \text{constant}$, i.e., the total energy in the plane transverse to the atom string, $E_{\perp}$, is constant throughout the motion,

$$E_{\perp} = K_{\perp} + U(r) \qquad (I.2))$$

I.4. CRITICAL TRANSVERSE ENERGY, RANDOM AND CHANNELED TRAJECTORIES, RANDOM FRACTION.

The Continuum Potential approximation breaks down when the channeled particle approaches close enough to the atom row to begin to experience significant deflection from individual atoms. Thus the region of validity of this approximation can be found by demanding that, at the minimum distance of approach, the repulsion of a channeled particle from the string is due to the cumulative effect of scattering by many atoms. The distance travelled along the channel, during the time taken for a collision with the string, is required to be large compared with d. Lindhard uses this condition to find the Continuum Potential approximation to be valid for channeled particles having

$$E_{\perp} < E\psi_1^2,$$

where $\psi_1 = \left(\frac{2Z_1 Z_2 e^2}{4\pi\epsilon_0 \, dE}\right)^{1/2}$,

and E is the total energy of the particle. If a particle has approximately

$$E_{\perp} \geq E\psi_1^2 \qquad \text{or} \qquad \psi \geq \psi_1$$

where ψ is the instantaneous angle a particle makes with the channel axis, then its trajectory is such that it will feel individual atoms in the string, undergo close-encounter collisions and be scattered out of the channel. Once outside the channel, the particle will interact with the atoms as though the crystal is an amorphous material having a random distribution of atoms. Lindhard therefore calls $E\psi_1^2$ and ψ_1 the Critical Transverse Energy, $E_{\perp_c}$, and the Critical Angle, ψ_c, respectively. He uses these values to differentiate between particles which have Channeled

Trajectories ($E_\perp < E_{\perp_c}$) and those which have Random Trajectories ($E_\perp \geq E_{\perp_c}$). When a beam of particles is incident on a channel axis, then for a particular depth in the crystal, the Random Fraction is the ratio of the number of particles having random trajectories (at that depth) to the number of particles incident on the crystal. Small impact parameter collisions ($\ll a$) with string atoms are forbidden for channeled particles, but allowed for random beam particles.

I.5 DECHANNELING

In the Continuum Potential approximation, transverse energy is conserved and so the Random Fraction of the beam would be expected to remain constant with depth. However, it is found experimentally that the Random Fraction increases with depth. The implication is that a particle in the Channeled beam ($E_\perp < E\psi_1^2$) at depth z somehow increased its energy as it moved down the channel, until at a depth z' (z' > z), $E_\perp = E\psi_1^2$ and the particle made the transition to the random beam. This process of transition from the channeled beam to the random beam is known as Dechanneling.

I.6 THE DIFFUSION IN TRANSVERSE ENERGY

The increase in transverse energy was attributed to multiple scattering of the channeled particles by the vibrating target nuclei, electrons and defects. Particles having transverse energy between $E_\perp$ and $E_\perp + dE_\perp$ are uniformly distributed across their accessible area in transverse plane. As this group of particles moves down the channel, each particle will experience somewhat different multiple (and inelastic)

scattering. Hence, at a larger depth in the crystal, there will be a spread in transverse energy within this group of particles. This spreading, or diffusion, in transverse energy led to the formulation of a Diffusion Equation to describe the change in the distribution of transverse energy and to calculate the Random Fraction as a function of depth[14,15]. The Diffusion Equation has proved difficult to solve numerically.

I.7 THE STEADY INCREASE IN TRANSVERSE ENERGY (SITE) APPROXIMATION

If dechanneling is to be studied for depths less than a few microns, the calculations may sometimes be simplified by using the SITE approximation, in which diffusion in transverse energy is neglected[16-19]. From (I.2), $E_\perp = K_\perp + U(r)$ or

$$E_\perp = E\psi^2 + U(r) \qquad (I.3)$$

where E is the total incident energy of the particle and

ψ is the instantaneous angle of the particle's trajectory with the channel direction.

Then the average change in transverse energy with depth, $\left\langle \frac{dE_\perp}{dz} \right\rangle$, averaged over the accessible area in the transverse plane, for particles of transverse energy $E_\perp$, is given by

$$\left\langle \frac{dE_\perp}{dz} \right\rangle = E \left\langle \frac{d\psi^2}{dz} \right\rangle + \left\langle \psi^2 \frac{dE}{dz} \right\rangle + \left\langle \frac{dU(r)}{dz} \right\rangle \qquad (I.4)$$

where $E \left\langle d\psi^2/dz \right\rangle$ is the average increase in $E_\perp$ with depth due to the multiple scattering by nuclei, electrons and defects, if present. In a well-ordered crystal, defect scattering is neglected, and

$$E \left\langle \frac{d\psi^2}{dz} \right\rangle = \left\langle \left(\frac{dE_\perp}{dz} \right)_n \right\rangle + \left\langle \left(\frac{dE_\perp}{dz} \right)_e \right\rangle .$$

$\left\langle \psi^2 \frac{dE}{dz} \right\rangle$ is the average decrease in $E_\perp$ with depth due to energy loss from inelastic interactions with electrons (damping term), and

$\left\langle \frac{dU(r)}{dz} \right\rangle = 0$, since U(r) is independent of z.

Björkqvist[16] uses Lindhard's analysis to calculate the terms in (I.4) as a function of transverse energy for 2.0 MeV protons incident on the $\langle 100 \rangle$ direction in tungsten and for 1.5 MeV protons on the $\langle 111 \rangle$ in silicon, see Fig. I.1(a). This Figure shows that channeled particles, which have high transverse energies at the crystal surface, also have high $\left\langle \frac{dE_\perp}{dz} \right\rangle$ values and hence will be dechanneled at shallow depths. The assumption is made that, for these particles, diffusion in transverse energy is small enough to be neglected and that all particles incident on the crystal surface with a transverse energy $E_\perp$ will be dechanneled at the same depth below the surface. This is the basis of the SITE approximation.

I.8 DECHANNELING MEASUREMENTS IN WELL-ORDERED SINGLE CRYSTALS

Dechanneling measurements have been made for several well-ordered single crystals, e.g., silicon, tungsten, tantalum and, to a lesser extent, gold. In a typical study, dechanneling was investigated as a function of temperature, axial direction and particle type. Calculations, in which dechanneling by defects is presumed to be negligible, have been made using either the SITE approximation or with the diffusion in transverse energy included. Figure I.1(b) shows that agreements between the SITE calculations and the experimental results obtained by Foti et al.[18] for protons in silicon is reasonable. Figure I.2(a) shows the work of the Aarhus group with protons on silicon $\langle 110 \rangle$. Their calculations using

Figure I. 1(a)

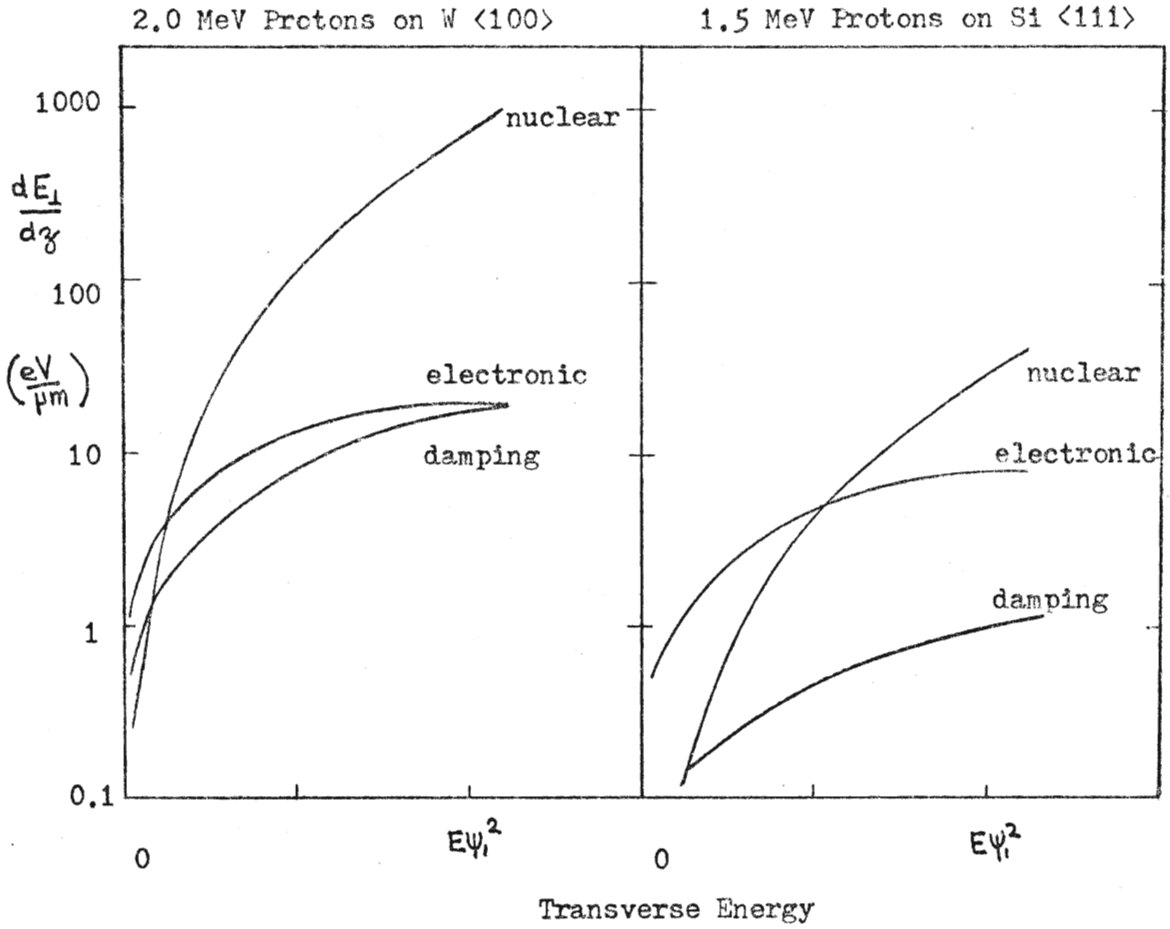

Figure I. 1(b)

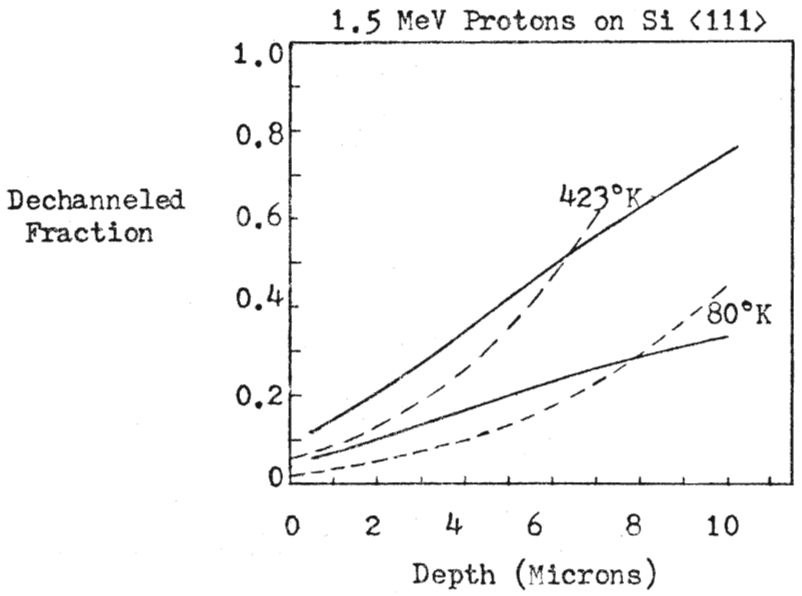

Experimental (——) and Theoretical (- - -) Dechanneled Fraction spectra obtained by Foti et al.

Figure I. 2(a)

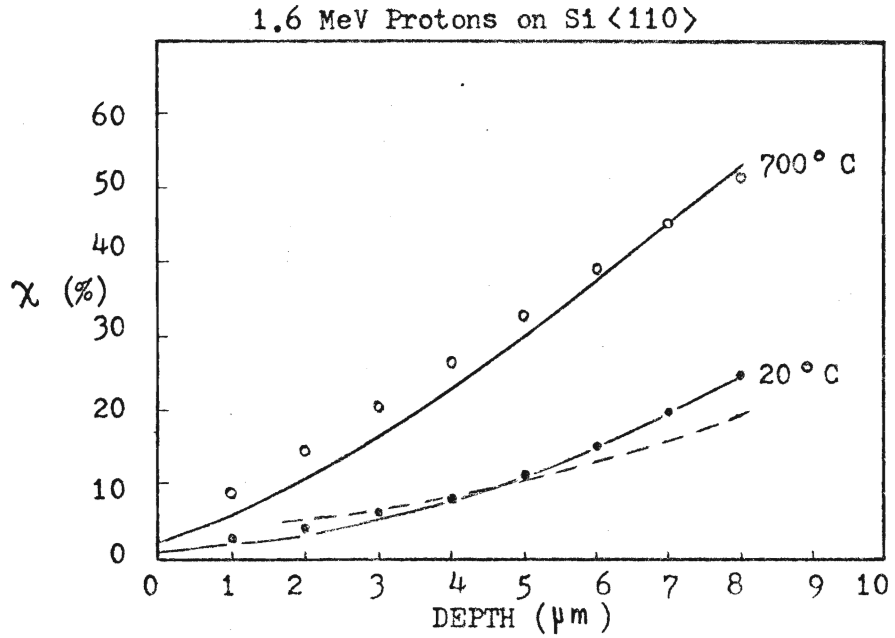

Measured points and calculated (by diffusion(——) and using SITE approximation (- - -)) Random fraction versus depth.

Figure I. 2(b)

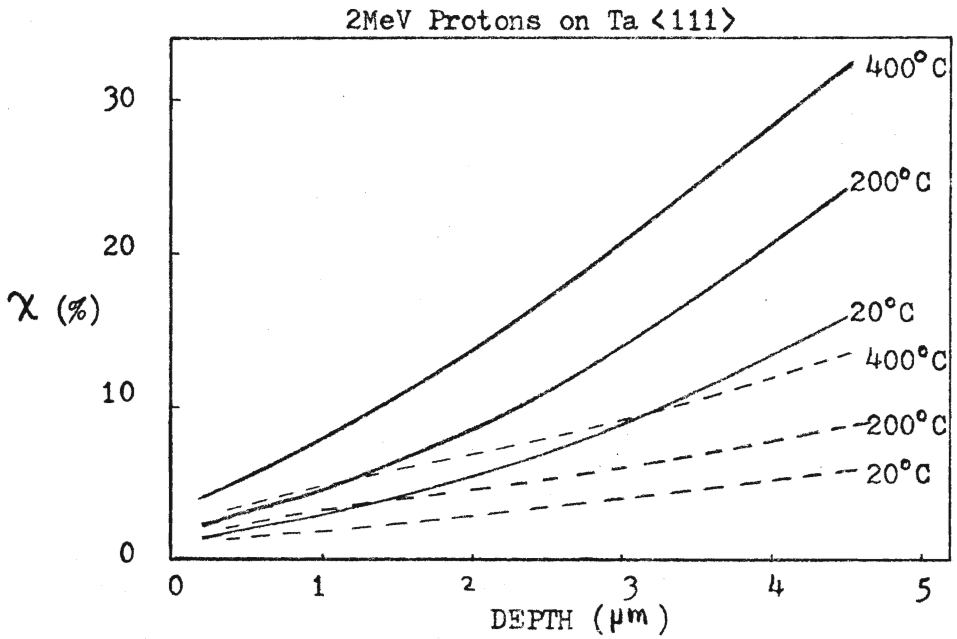

Measured (——) and calculated(- - -) by diffusion equation, Random Fraction versus Depth as a function of Temperature.

the SITE approximation[15] and those considering diffusion[23,24] are in agreement with each other and in reasonable agreement with experiment at shallow depths. They have also found good agreement between their diffusion calculations and experiment for protons in tungsten as a function of temperature and axial direction, but found discrepancies between measured and calculated values for other materials investigated (iron, niobium, molybdenum, tantalum). The calculated Random Fraction for tantalum was found to be lower than the experimental by between 50% and 100%[24], see Figure I.2(b).

I.9 DECHANNELING MEASUREMENTS IN DEFECTED SINGLE CRYSTALS

Dechanneling has also been used to study defected single crystals to obtain the defect concentration as a function of depth (defect concentration profile). This has been done by Picraux[21] using proton beams in silicon and by Pronko[20], Merkle et al.[25] at Argonne using He^+ beams in gold. Picraux, in his analysis, assumed that the defects lay in the channels (as interstitials) and the channeled particles directly interacted with the defects. On the other hand, Pronko assumed that the defects were only slightly off lattice sites, causing strains in the lattice, but did not directly cause backscattering of the channeled beam. The lattice strains, however, produced significant dechanneling by causing perturbations in the continuum potential.

Pronko, using the SITE approximation in a dechanneling analysis, was able to determine the broad features in the across-channel distribution of the misaligned atoms in the strained lattice.

I.10 OUTLINE OF THIS THESIS

Extensive theoretical and experimental dechanneling studies have been made for a few well-ordered single crystals, such as silicon and tungsten. To our knowledge, gold has received scant attention, except for some room temperature measurements included in the work of Merkle et al., and Pronko. Furthermore, gold is a particularly suitable element for dechanneling studies because:

(i) it is inert to reactions with the atmosphere, therefore it can be prepared with a relatively clean ordered surface,

(ii) it has a low Debye Temperature (170°K), hence one dominant dechanneling mechanism, namely thermal nuclear multiple scattering,

(iii) it can be prepared, as a single crystal, in either thin film or in bulk crystal form. Hence, gold can be used in defect dechanneling studies using the electron microscope and Rutherford backscattering.

In this thesis we will examine some aspects of a dechanneling study in gold. The thesis describes:

(i) the preparation of well-ordered gold single crystals,

(ii) measurement of dechanneling of 2 MeV He^+ in gold as a function of temperature and depth, and

(iii) comparison of experimental results with theoretical calculations based upon the SITE approximation.

CHAPTER TWO

RUTHERFORD BACKSCATTERING SPECTRA

In this experiment, measurement of the variation of the Random Fraction of the beam with depth, at various temperatures, is required. The detection technique used must therefore be able to distinguish between the scattering of random and channeled beam particles and to provide a means of measuring the depth at which scattering occurs.

The channeled particle cannot have $E_\perp > E_{\perp_c}$, where $E_{\perp_c} = U(r_c)$ $= E\psi_{1/2}^2 \cdot \ln\left(\frac{C^2a^2}{r_c^2} + 1\right)$, r_c is the closest distance of approach a channeled particle can have with the centre of the string of atoms and is approximately equal to the Thomas-Fermi screening parameter a.

On the other hand, random particles are not steered away from the string atoms and can experience small impact parameter collisions with a probability equal to that for an amorphous target. Rutherford Backscattering is the name given to the collision between a particle and a target atom, when the particle penetrates to a distance very much less than "a" from the nucleus of a target atom. For example, a 2.0 MeV He^+ particle making a head-on collision with a gold target atom approaches to 0.01a from the gold nucleus. Consequently, Rutherford Backscattering (R.B.S.) from a string atom is forbidden for channeled particles, but allowed for random particles. Furthermore, the energy of a backscattered particle leaving the target is a measure of the depth of the scattering below the crystal surface.

Rutherford Backscattering, therefore, is a means of distinguishing between random and channeled particles and, by measuring the ratio of aligned and non-aligned (random) yields from a crystal, the random fraction as a function of depth is determined[26]. This technique has been used in this work.

II.1 KINEMATICS

Figure II.1 represents an elastic collision, in laboratory co-ordinates, between a moving atom, of mass M_1, and a stationary target atom, of mass M_2. It can readily be shown, using the conservation of energy and of linear momentum, that $E_1 = k^2 E_0$

$$\text{where } k = \frac{M_1 \cos\theta_1}{M_1 + M_2} + \left[\left(\frac{M_1 \cos\theta_1}{M_1 + M_2} \right)^2 + \frac{M_2 - M_1}{M_1 + M_2} \right]^{1/2} \qquad \text{(II.1)}$$

for $M_2 > M_1$.

II.2 R.B.S. ENERGY SPECTRUM

Figure II.2 shows the beam-target geometry for Rutherford Backscattering. The incident beam consists of particles of mass M_1 and energy E_0 and the target atoms have mass M_2. Particles backscattered at a depth x into a detector located at an angle θ_1, leave the target with an energy $E_{1,x}$. E_1 is measured by a semiconductor detector and the distribution in E_1 is recorded by a multichannel analyser. The distribution in E_1 is called the R.B.S. energy spectrum.

Figure II. 1

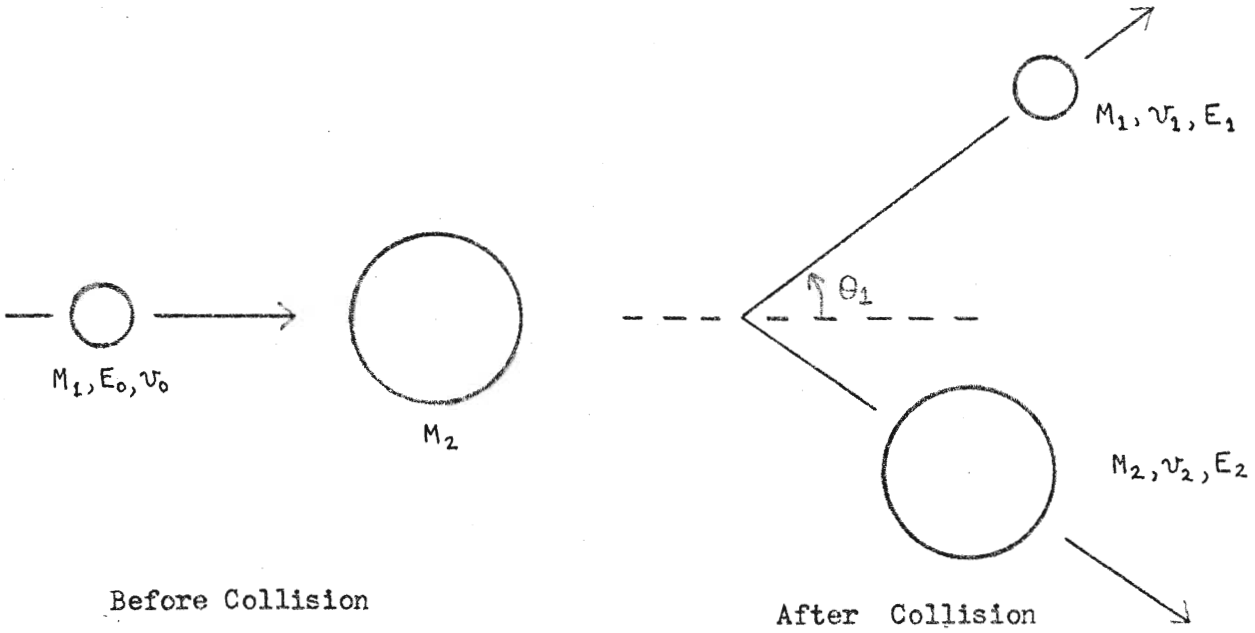

Before Collision

After Collision

Figure II. 2

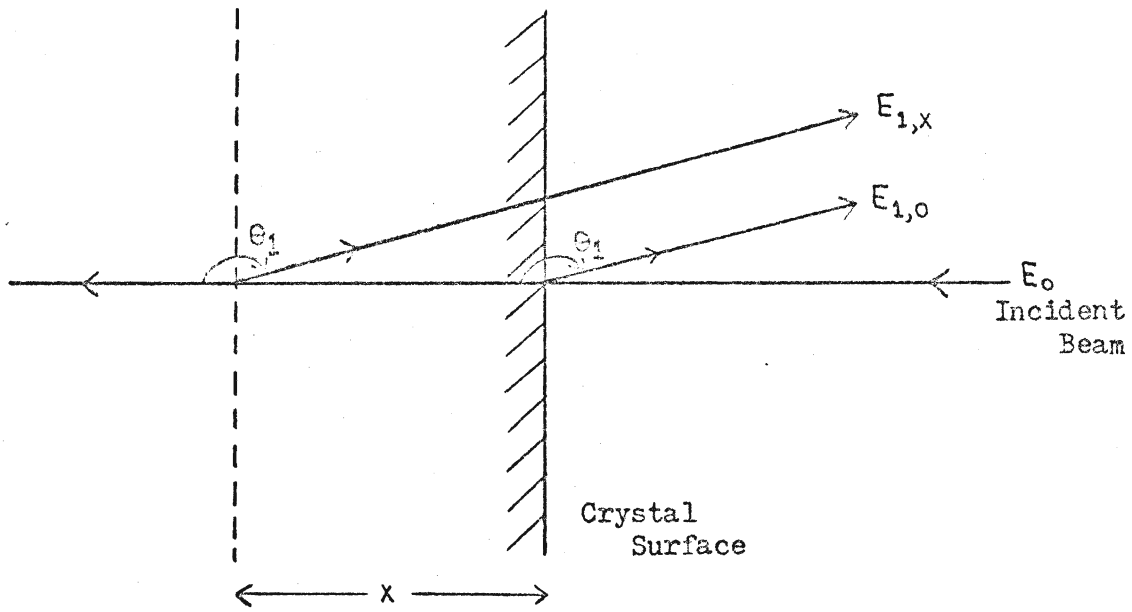

II.3 THE RANDOM SPECTRUM

For the case when the crystal target is not aligned with the beam, all particles have random trajectories and the R.B.S. spectrum is called the Random Spectrum.

II.3.1 DEPTH SCALE FOR RANDOM SPECTRUM

During their passage through the crystal, the particles lose energy by excitation and ionisation of the target atoms. The rate of energy loss is given by the stopping power, S(E). So, particles scattered at a depth x have a backscattered energy $E_{1,x}$, as recorded by the detector, given by:

$$E_{1,x} = k^2(\theta_1) \cdot \left[E_o - \int_A^B S(E) \cdot dl \right] - \int_B^C S(E)\, dl \qquad \text{(II.2)}$$

where the first line integral is along the incoming path and the second along the outgoing path. This expression enables one to make an energy-to-depth conversion[27].

II.3.2 THE SHAPE OF THE RANDOM SPECTRUM

Assuming that single scattering occurs, the number of particles, dN, scattered into the detector from a small depth interval of thickness dx located at a depth x below the crystal surface, see Figure II.3, is given by:

$$dN = N \cdot \eta \cdot dx \cdot d\Omega \cdot \frac{d\sigma}{d\Omega} \qquad \text{(II.3)}$$

where $d\Omega$ is the solid angle subtended by the detector,

n is the number of atoms per unit volume in the crystal,

N it the total number of particles incident on the crystal, and

$\frac{d\sigma}{d\Omega}$ is the Rutherford differential scatteringcross-section, given by:

$$\frac{d\sigma}{d\Omega} = \left(\frac{Z_1 Z_2 e^2}{2 \cdot 4\pi\epsilon_0} \cdot \frac{1}{2E} \right)^2 \cdot \frac{1}{\sin^4(\theta_1/2)} \qquad \text{(II.4)}$$

i.e., $\frac{d\sigma}{d\Omega} \propto \frac{1}{E^2}$, where E is the mean energy of beam particles in the interval dx.

If dE_1 is the range in values of E_1 of particles backscattered from the depth interval dx, then the Random (Energy) Spectrum refers to the variation of $\frac{dN}{dE_1}$ with E_1 (see Figure II.4) where (II.3) now becomes:

$$\frac{dN}{dE_1} = N \cdot n \cdot dx \cdot d\Omega \cdot \frac{d\sigma}{d\Omega} \cdot \frac{1}{dE_1} \qquad \text{(II.5)}$$

Therefore the Random Spectrum shape is determined by the variation of $\frac{1}{dE_1} \cdot \frac{d\sigma}{d\Omega}$ with E_1. Usually, but not always, $\frac{dN}{dE_1}$ increases monotonically as E_1 decreases and exhibits the shape shown in Figure II.4. $E_{1,0}$, the centre of the well-defined high energy edge, equals the energy of beam particles backscattered from the surface of the target and is a function of the mass ratio M_1/M_2 (see equation (II.1)). The slope of the high energy edge gives a measure of the energy (and hence depth) resolution of the detector.

Figure II. 3

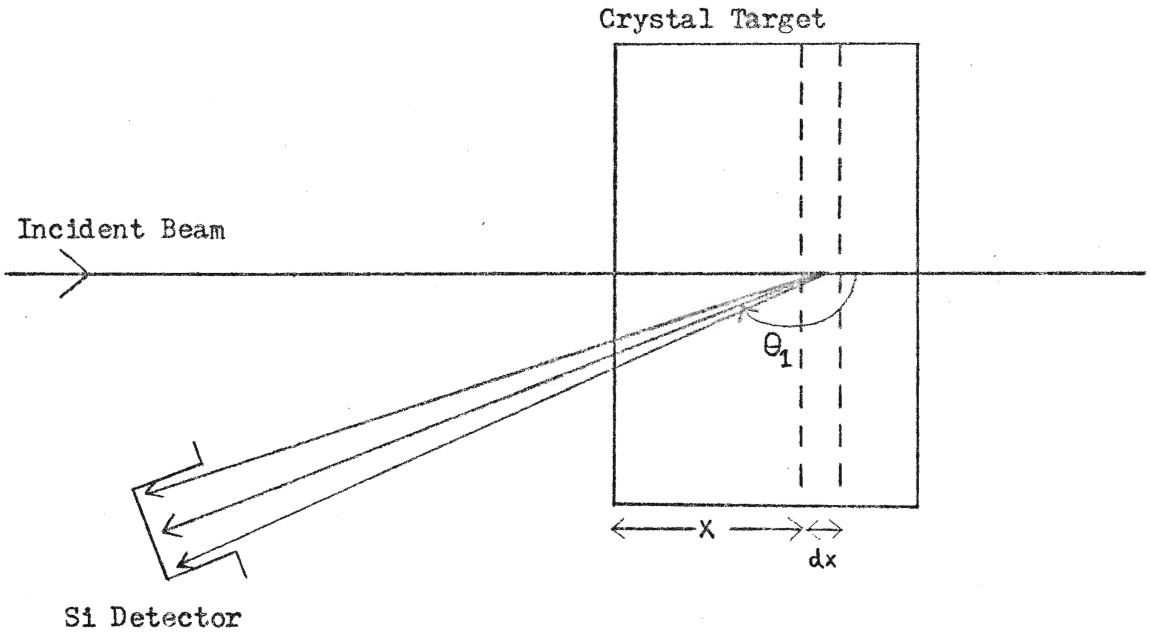

Figure II. 4

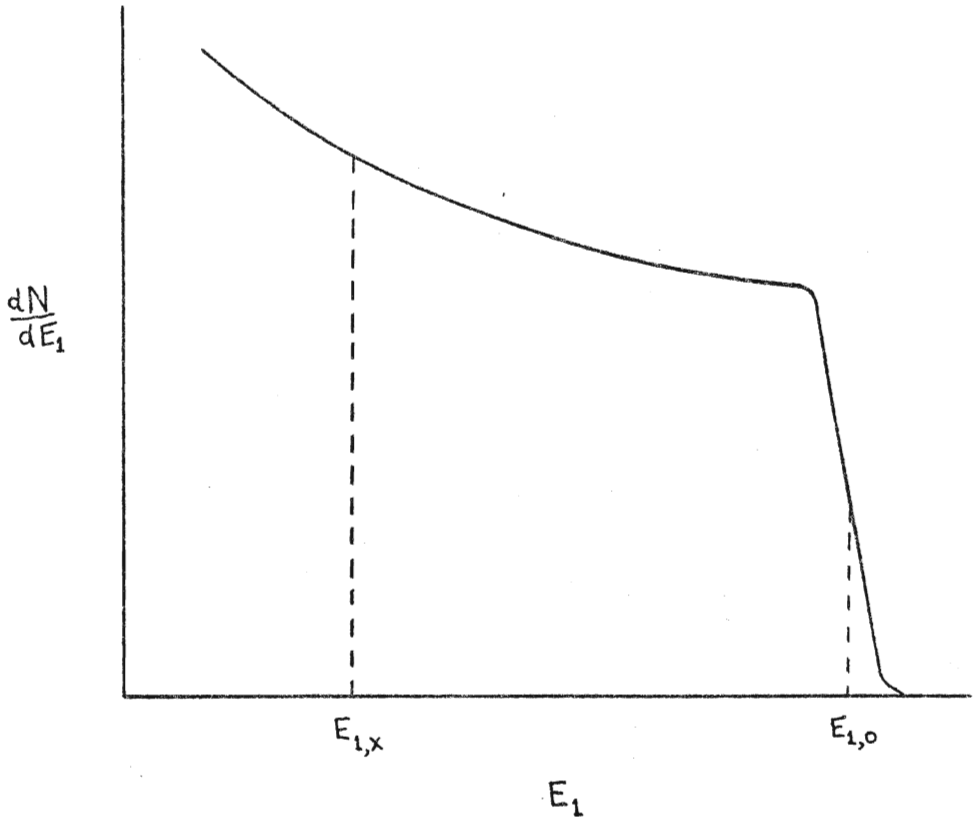

II.4 NUMERICAL ANALYSIS OF THE RANDOM SPECTRUM

II.4.1 CALCULATION OF THE DEPTH SCALE

With reference to Figure II.5, we require to find the relationship between the depth of the backscattering event, x_m (= mΔx), and the energy of the backscattered particle recorded by the detector, $E_{1,m}$. This is accomplished by the following numerical analysis of equation (II.2).

The depth x_m is divided into m equal intervals, each of thickness Δx. Summing along the incident beam particle path, we have:

$$E_{0,m} = E_{0,0} - \sum_{j=1}^{m} \{ S(E_{0,j-1}) . \Delta x \} \qquad \text{(II.6)}$$

where $E_{0,0}$ = Beam energy incident on target, and

$E_{0,m}$ = Beam particle energy after penetration to a depth m.Δx.

Summing along the path of the scattered beam particle gives:

$$E_{1,m} = \varepsilon_{1,0} - \sum_{l=1}^{m} \{ S(\varepsilon_{1,l-1}) . \frac{\Delta x}{\cos\theta_1} \} \qquad \text{(II.7)}$$

where

$$\varepsilon_{1,s} = \varepsilon_{1,0} - \sum_{p=1}^{s} \{ S(\varepsilon_{1,p-1}) . \frac{\Delta x}{\cos\theta_1} \} \; ; \; s \neq 0 \qquad \text{(II.8)}$$

and

$$\varepsilon_{1,0} = k^2 E_{0,m} \qquad \text{(II.9)}$$

Equations (II.6) to (II.9) have been used to calculate the relationship between x_m and $E_{1,m}$, using a value of Δx which gives satisfactory convergence.

Figure II. 5

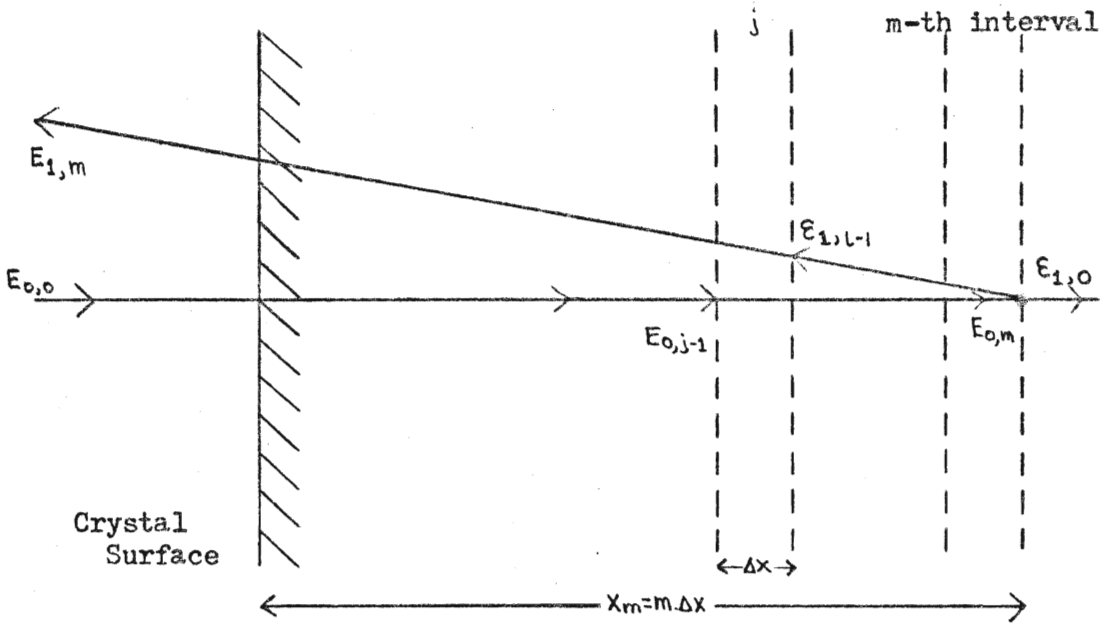
j
m-th interval
$E_{1,m}$
$\varepsilon_{1,j-1}$
$\varepsilon_{1,o}$
$E_{o,o}$
$E_{o,j-1}$
$E_{o,m}$
Crystal
Surface
Δx
$x_m = m.\Delta x$

II.4.2 CALCULATION OF THE SHAPE OF THE RANDOM SPECTRUM

The multichannel analyser used to record the energy spectrum is characterised by a relationship between back-scattered energy, $E_{1,m}$, and the analyser channel number, C_m. I.e.,

$$E_{1,m} = \Delta E_1 . C_m + b$$

where ΔE_1 is the energy width of each channel.

Let $\langle C \rangle_m$ be the mean channel number for particles backscattered from the m-th depth interval, hence

$$\langle C \rangle_m = \tfrac{1}{2} (C_m + C_{m-1}) .$$

Let $\langle \Delta N \rangle_m$ be the number of counts per channel at channel $\langle C \rangle_m$, hence

$$\langle \Delta N \rangle_m = \text{constant} . \frac{1}{\langle E_0 \rangle_m^2} . \frac{1}{(C_{m-1} - C_m)} ,$$

where $\langle E_0 \rangle_m$ is the mean energy of an incident beam particle in the m-th interval, i.e.,

$$\langle E_0 \rangle_m = \tfrac{1}{2} (E_{0,m-1} + E_{0,m}) .$$

A plot of $\langle \Delta N \rangle_m$ versus $\langle C \rangle_m$ represents the calculated random (energy) spectrum which is compared directly to the measured random spectrum by normalising the two plots at channel C_s, just behind the surface edge (see Figure II.6).

Figure II. 6.

Random Spectra. Calculated spectrum (- - -) normalized to measured spectrum (——) near front edge. Two measured thin film spectra are also shown, displaying tails not predicted by single Rutherford scattering theory.

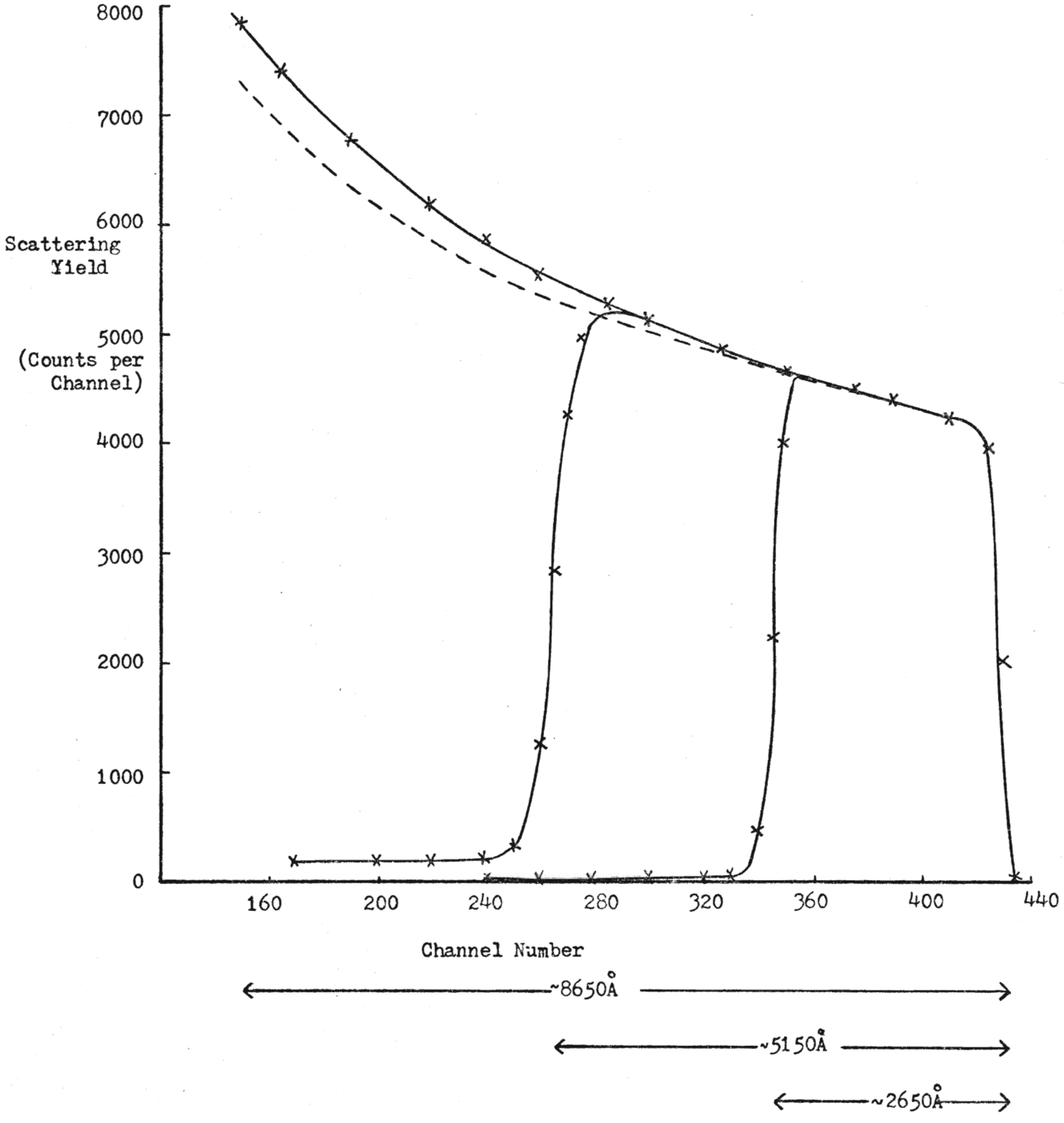

II.4.3 COMPARISON OF MEASURED AND CALCULATED RANDOM SPECTRA

Experimental random spectra have been taken for 2 MeV He^+ on gold. A variety of targets have been used, including thin film and bulk specimens in poly-crystalline and in single crystal form. The single crystal specimens were continuously rotated in order to reduce any channeling effects to essentially negligible amounts. All these measured spectra were found to have the same shape to within approximately 2%. The mean value of these measured spectra is plotted in Figure II.6, and the calculated spectrum normalised to this mean measured spectrum. Two measured spectra from thin films are also shown.

The calculated spectrum and the depth scale, calculated according to the analysis in sections II.4.2 and II.4.1, assume single scattering and use an empirical stopping power function S(E) given in the recent comprehensive compilation by Ziegler and Andersen[28].

The difference between the measured and calculated spectra appears to be a consequence of the effects producing the low energy "tails" which are evident in the measured thin film spectra. The origin of the low energy tails is uncertain, but may well be due to particles entering the detector as a result of more than one large-angle scattering. Figure II.6 shows that, at a depth of 6000 Å, the difference between the measured Random Spectrum and that calculated assuming s ingle Rutherford scattering is approximately 6%. Our assumption that single Rutherford scattering is the predominant mechanism for backscattering of 2 MeV He^+ from gold and the use of the Ziegler and Andersen stopping power data would appear to be valid. However, for 1 MeV protons in gold, a difference of 15% or greater between calculated and measured Random Spectra was found at depths greater

than 15,000 Å. In the absence of further data, this leads to corresponding uncertainties in the determination of the Random Fraction from the R.B.S. spectra of 1 MeV protons from gold. Consequently, this thesis is restricted to a study of the dechanneling of 2 MeV He^+ in gold.

II.5 THE ALIGNED SPECTRUM AND THE RANDOM FRACTION

The aligned spectrum refers to the backscattered energy spectrum taken with the crystal axis precisely aligned with the beam direction. If the crystal has no displacement defects, from which the channeled beam can backscatter, then only the random fraction of the beam can undergo backscattering. In this case, assuming single (R.B.S.) scattering and that the same energy to depth scale conversion applies to both the random and aligned spectra, then the Aligned Yield, dN', is given by:

$$dN' = N' . n . dx . d\Omega . \frac{d\sigma}{d\Omega} \qquad \text{(II.10)}$$

where N' is the number of particles in the random beam incident on the depth interval of thickness dx at a distance x below the crystal surface. The Random Fraction, χ, at that depth is defined as N'/N, where N is the total number of particles incident on the crystal. Hence, the ratio of the Aligned Yield to the Random Yield for that depth interval is given by:

$$\frac{dN'}{dN} = \frac{N' . n . dx . d\Omega . d\sigma/d\Omega}{N . n . dx . d\Omega . d\sigma/d\Omega} = \frac{N'}{N} = \chi(x)$$

using (II.3) and (II.10), and so the Random Fraction as a function of depth can be extracted from the measured Aligned and Random Spectra.

The general features of aligned spectra are shown in Figure II.7; a random spectrum is included for quantitative comparison. The increase (with increasing depth) of the aligned yield, and hence the dechanneling rate and the random fraction, with increase in temperature and defect concentration is illustrated schematically.

II.5.1 SURFACE PEAK IN THE ALIGNED SPECTRUM

The incident beam does not yet experience the channeling effect, at the surface, therefore it is not steered away from the surface atoms. Hence the aligned beam scatters from the surface atoms with normal probability and a normal (random) yield is always obtained from the surface atoms. The surface peak in the aligned spectrum is due to backscattering from any disordered gold atoms at the surface and/or the gold atoms at the ends of the atomic strings, the latter effect being temperature-dependent.

The number of atoms per unit area at the surface contributing to the surface peak can be calculated using the surface peak yield and the random yield from the surface region.[29]

If Y_{SA} is the surface peak yield in the aligned spectrum and Y_{SR} is the yield in the random spectrum from a surface element of thickness dx, then, for the same number of incident beam particles, N,

$$Y_{SA} = N \cdot n' \cdot dx' \cdot d\Omega \cdot \frac{d\sigma'}{d\Omega} ,$$

and

$$Y_{SR} = N \cdot n \cdot dx \cdot d\Omega \cdot \frac{d\sigma}{d\Omega} ,$$

where n'dx' is the number of atoms per unit area in the surface which can backscatter the aligned beam, and

Figure II. 7

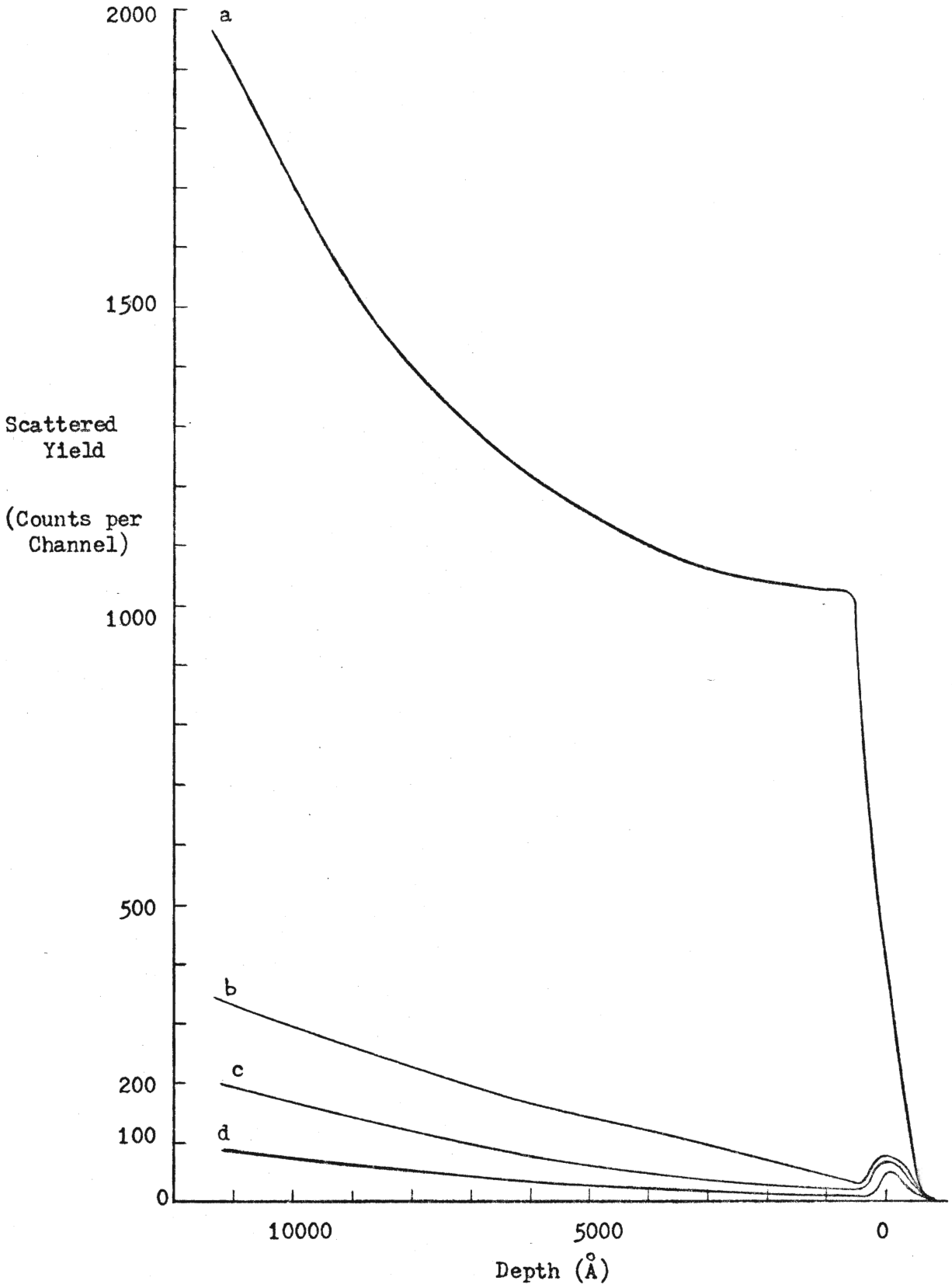

a) Random Spectrum
b) Aligned Spectrum, crystal with defects, room temperature
c) Aligned Spectrum, crystal without defects, room temperature
d) Aligned Spectrum, crystal without defects, low temperature.

$\frac{d\sigma'}{d\Omega} = \frac{d\sigma}{d\Omega}$, since backscattering occurs at the same depth (and hence energy) in each case.

Hence $$n'dx' = \frac{Y_{SA}}{Y_{SR}} . n.dx \quad .$$

Also $$n.dx. = \frac{n. \Delta E}{k^2.S_o + S_1/\cos\theta_1}$$

where S_0, S_1 are the stopping powers of the incident and backscattered beam respectively and ΔE is the difference in energy of particles from the front and rear surfaces of dx.[27]

For small values of dx, and with $\theta_1 = 150°$ and $k^2 = 0.92696$ for He^+ on gold, then $k^2 S_o + S_1/\cos\theta_1 \approx 2S_o$.

Therefore $$n'dx' = \frac{Y_{SA}}{Y_{SR}} . \frac{n.\Delta E}{2S_o} \quad .$$

Y_{SA}, Y_{SR} and ΔE can be measured and S_0 taken from the tables of Ziegler and Andersen.[28]

From the observed variation of n'dx' with temperature, the number of disordered gold atoms per unit area at the surface can be deduced.

II.5.2 MINIMUM YIELD, χ_{min}

χ_{min} is the value of the Aligned Fraction in the surface region. In a well-ordered crystal, it is essentially the fractional area for which channeled trajectories are not possible when a beam is aligned with a channel axis. Within this area, the initial transverse energy is greater than the critical value $E_{\perp_c}$.

Lindhard[14] has approximated χ_{min} by:

$$\chi_{min} \approx n.d.\pi.(a^2 + \rho^2) + \chi_3 \ ,$$

where n is the number of atoms per unit volume in the crystal,

d is the interatomic spacing along the string,

a is the Thomas-Fermi screening length,

ρ is the r.m.s. thermal vibrational amplitude at the crystal temperature.

χ_3 refers to the component of the Random Fraction due to single Rutherford scattering of particles in the aligned beam through angles greater than ψ_1 by atoms in the surface disorder layer.[14]

$$\chi_3 \approx \frac{n.\Delta z.\pi.Z_1^2.Z_2^2.e^4}{(4\pi\epsilon_0)^2.E^2\psi_1^2}$$

Better agreement between experimental and calculated χ_{min} values has been obtained by Barrett[39], who used Monte Carlo calculations to obtain the expression,

$$\chi_{min} = n.d.\pi.(3(\pm 0.2)\rho^2 + 0.2(\pm 0.1)a^2).$$

This expression generally gives good agreement with experimental values obtained from crystals with minimal surface disorder.

CHAPTER THREE

THE STEADY INCREASE IN TRANSVERSE ENERGY (SITE) APPROXIMATION

If $\left\langle \frac{dE}{dz} \right\rangle$ increases rapidly with $E_\perp$, then particles having high initial transverse energy, $E_{\perp_0}$, will be dechanneled at shallow depths, before diffusion (i.e., spread) in their transverse energy becomes appreciable. In such cases, diffusion in $E_\perp$ can be neglected and we assume that the transverse energy of the particle increases steadily with depth, such that $\left\langle \frac{dE_\perp}{dz} \right\rangle = \left(\frac{dE_\perp}{dz} \right)$. This is the basic assumption of the SITE approximation.[14] We have calculated $\left\langle \frac{dE_{\perp_0}}{dz} \right\rangle$ versus $E_{\perp_0}$ for 2 MeV He^+ in $\langle 110 \rangle$ gold, see Figure III.1, using the analyses of Lindhard[14] and Foti[18]. It can be seen from this figure that the criterion for using the SITE approximation is fulfilled in this case.

The depth z', at which a particle having initial transverse energy $E_{\perp_0}'$ will be dechanneled, is given by:

$$z' = \int_{E_{\perp_0}'}^{E_{\perp_c}} \frac{dE_\perp}{(dE_\perp/dz)} ,$$

where $E_{\perp_c}$ is the critical transverse energy. Particles having $E_{\perp_0} > E_{\perp_0}'$ will also be in the random beam at depth z'. Therefore,

$$\int_{E_{\perp_0}'}^{\infty} p(E_{\perp_0})\, dE_{\perp_0}$$

will give the Random Fraction of the beam at depth z', where $p(E_{\perp_0})$ is the initial transverse energy probability distribution. By selecting different $E_{\perp_0}'$ values and using this procedure, the Random Fraction as a function of depth can be calculated.

The following outline of the SITE approximation is due to Lindhard[14] and Foti *et al.*[18]

Figure III. 1

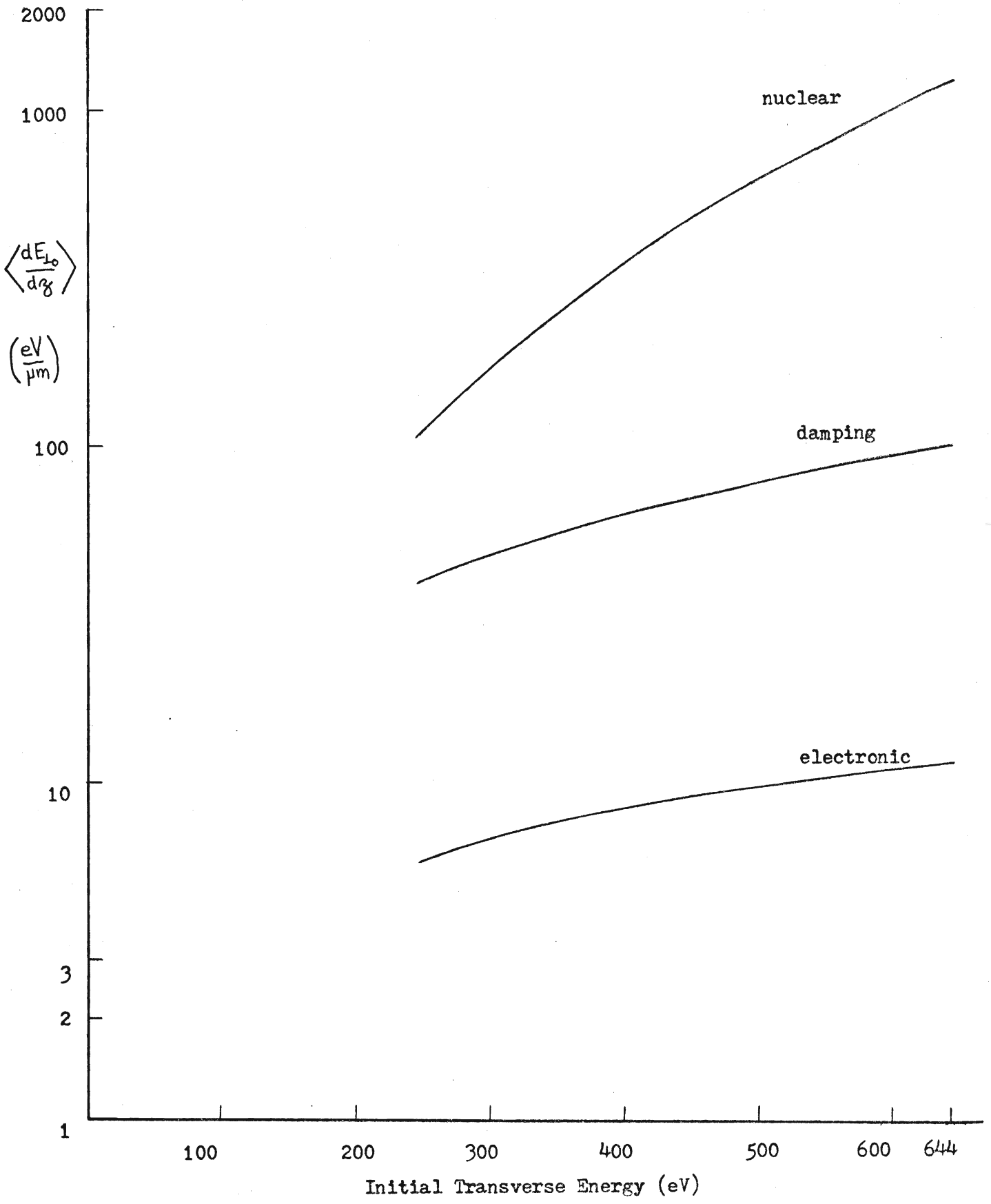
2000
1000
100
10
3
2
1
$\left\langle \frac{dE_{\perp_o}}{d\chi} \right\rangle$
$\left(\frac{eV}{\mu m}\right)$
nuclear
damping
electronic
100
200
300
400
500
600
644
Initial Transverse Energy (eV)

III.1 THE INITIAL TRANSVERSE ENERGY DISTRIBUTION

If the incident beam is precisely aligned with a channel axis and we neglect the effect of scattering by disordered surface atoms, then the initial transverse energy $E_{\perp 0}$, measured with respect to that at the centre of the channel, is given by

$$E_{\perp 0} = U(r) - U(r_0) \qquad \text{(III.1)}$$

where r is the distance (in the transverse plane) of the point of impact from the centre of the atomic string,

r_0 represents the distance from the string to the channel centre, and

πr_0^2 is approximately equal to the area per string projected perpendicular to the string direction.

If n is the number of atoms per unit volume in the crystal and d is the interatomic spacing along the string, then

$$n.d.\pi r_0^2 = 1 .$$

U(r) is the standard Lindhard continuum potential

$$U(r) = \frac{Z_1 Z_2 e^2}{4\pi\epsilon_0 d} . \ln\left(\frac{C^2 a^2}{r^2} + 1\right) \qquad \text{(III.2)}$$

The probability that a particle has an initial transverse energy between $E_{\perp 0}$ and $E_{\perp 0} + dE_{\perp 0}$ is equal to the probability that it enters the crystal between r and r + dr (in the transverse plane) from the centre of a string, see Figure III.2.

Hence the Initial Transverse Energy Distribution, $p(E_{\perp 0})$, is given by:

Figure III. 2

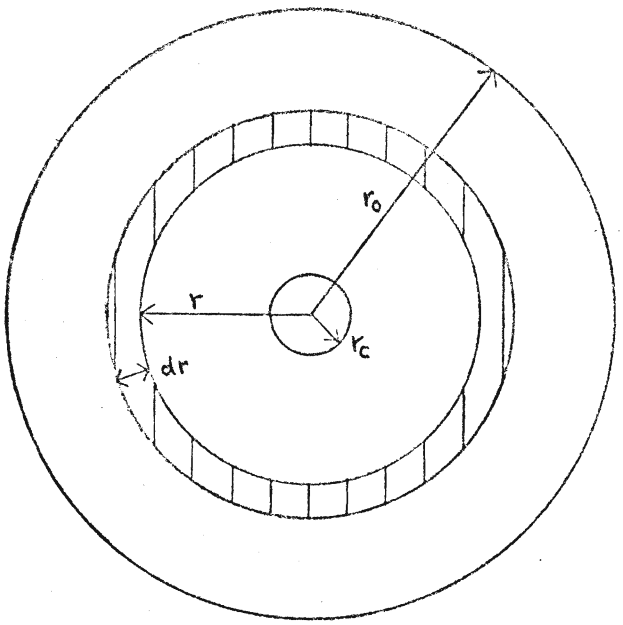

$$p(E_{\perp o})dE_{\perp o} = \frac{\pi\, d(r^2)}{\pi r_o^2} = \frac{2\pi r\, dr}{\pi r_o^2} \qquad \text{(III.3)}$$

From (III.1), (III.2) and (III.3), it can readily be shown that:

$$p(E_{\perp o})dE_{\perp o} = \frac{C^2 a^2}{r_o^2} \cdot A \cdot \frac{4\pi\epsilon_o d}{Z_1 Z_2 e^2} \cdot \frac{e^{2E_{\perp o}/E\psi_1^2}\, dE_{\perp o}}{(A.e^{2E_{\perp o}/E\psi_1^2} - 1)^2} \qquad \text{(III.4)}$$

where $A = \frac{C^2 a^2}{r_o^2} + 1$ and $E\psi_1^2 = \frac{2Z_1 Z_2 e^2}{4\pi\epsilon_o d}$.

III.2 THE RATE OF CHANGE OF TRANSVERSE ENERGY WITH DEPTH

During the motion of the particle in the channel, its transverse energy is given by:

$$E_\perp = E\psi^2 + U(r) - U(r_o)$$

Hence the average change in transverse energy with depth is given by:

$$\langle dE_\perp/dz \rangle = E\langle d\psi^2/dz \rangle + \langle \psi^2 dE/dz \rangle + \langle dU/dz \rangle \qquad \text{(III.5)}$$

The average is taken over the area in the transverse plane, equal to $\pi(r_0^2 - r_{min}^2)$, which is accessible to a particle of transverse energy $E_\perp$, where

$$E_\perp = U(r_{min}) - U(r_o).$$

See Figure III.3

Figure III. 3

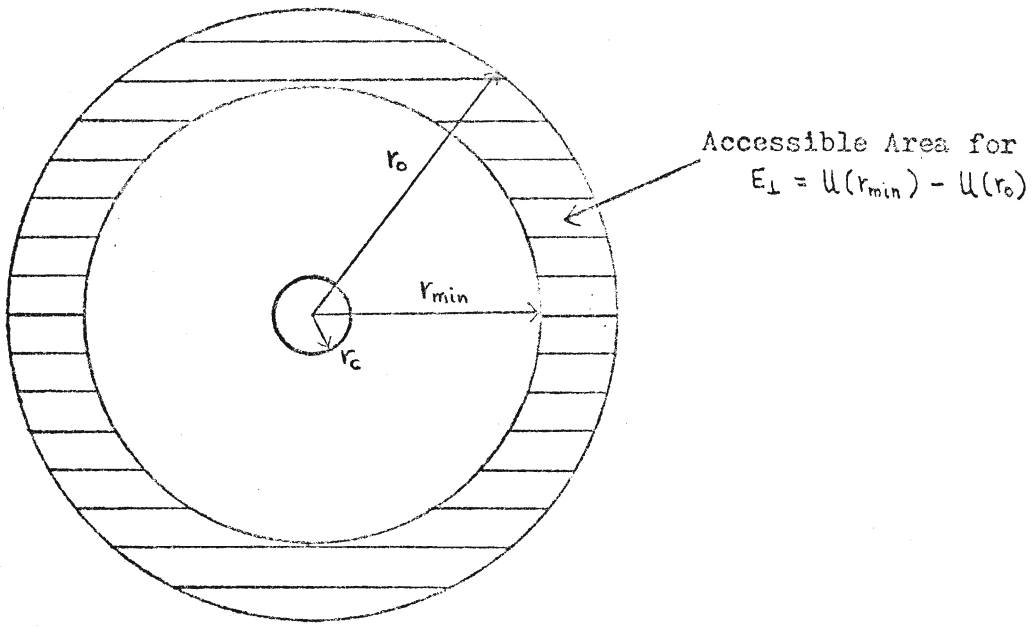

It is assumed that particles having transverse energy $E_\perp$ are uniformly distributed over the accessible area, i.e., there is a statistical equilibrium.

We shall consider the case of a perfect crystal, in which the multiple scattering due to disorder defects is therefore zero. Hence the multiple scattering term, $E\left\langle \frac{d\psi^2}{dz} \right\rangle$, can therefore be written:

$$E\left\langle \frac{d\psi^2}{dz} \right\rangle = \left\langle \left(dE_\perp/dz \right)_n \right\rangle + \left\langle \left(dE_\perp/dz \right)_e \right\rangle$$

where n and e refer to scattering by string atoms (nuclear) and atomic electrons (electronic scattering) respectively.

III.3 DAMPING TERM

Lindhard estimates the damping term, $\left\langle \psi^2 \frac{dE}{dz} \right\rangle$, to be given by:

$$\left\langle \psi^2 \, dE/dz \right\rangle \approx \beta \frac{E_\perp}{E} \left\langle dE/dz \right\rangle ,$$

where $\beta \approx 0.5 \longrightarrow 1.0$.

We have used, with Björkqvist *et al.*[16], the value $\beta = 0.5$. Note that $\left\langle \frac{dE}{dz} \right\rangle$ is negative, reflecting the reduction in total energy of the particle as it moves along the trajectory. Consequently, the damping term contributes a reduction to the rate of increase in $E_\perp$.

Since U(r) is independent of z, then $\left\langle \frac{dU}{dz} \right\rangle = 0$. Therefore (III.5) becomes:

$$\left\langle dE_\perp/dz \right\rangle = \left\langle \left(dE_\perp/dz \right)_n \right\rangle + \left\langle \left(dE_\perp/dz \right)_e \right\rangle + 0.5 \frac{E_\perp}{E} \left\langle dE/dz \right\rangle \quad \text{(III.6)}$$

III.4 NUCLEAR MULTIPLE SCATTERING

Lindhard considered the deviations from the transverse force $\vec{K}(r)$, corresponding to the continuum potential, which are caused by thermal vibrations of the string atoms and evaluated their scattering effect on channeled particles (of mass M_1, velocity v).

The average increase in $E_\perp$, due to the thermal vibrations of string atoms, (along a path δz) is estimated to be

$$\langle \delta E_\perp \rangle_n = \langle E_{\perp \delta z + z} \rangle - E_{\perp z} = \left\langle \frac{\Sigma (\delta \vec{p}_\perp)^2}{2M_1} \right\rangle = \frac{d}{4E} \left\langle \delta \vec{K}(r)^2 \right\rangle \delta z \qquad \text{(III.7)}$$

where $\delta\vec{K}(r)$ is the deviation from $\vec{K}(r)$ experienced by the channeled particle as it passes by the thermally-displaced string atom, and $\delta\vec{p}_\perp$ is the corresponding deviation in transverse momentum due to the displacement. The averaging in (III.7) is taken over the accessible transverse area for particles with that transverse energy, over the possible thermal displacements, and also along the path δz.

For small thermal vibrational amplitudes, $r \gg \rho$, and so (as stated by Lindhard):

$$\langle \delta \vec{K}(r)^2 \rangle = \tfrac{1}{2} \rho^2 \left\langle \frac{K^2(r)}{r^2} + \left(\frac{dK(r)}{dr} \right)^2 \right\rangle \qquad \text{(III.8)}$$

where $K(r) = - \partial U / \partial r$ (III.9)

and $U = U(r) - U(r_0)$ (III.10)

Using (III.8), (III.9) and (III.10) in (III.7), the following result is obtained by Foti *et al.*[18]:

$$\left\langle \frac{\delta E_1}{\delta \gamma} \right\rangle_n = \frac{\pi . n . Z_1 . Z_2 . e^2 . d . \rho^2 . E\psi_1^2}{E . 4\pi\epsilon_0 . C^2 . \beta^2 \cdot 2} \left\{ \frac{(Ae^{2E_1/E\psi_1^2} - 1)}{A(e^{2E_1/E\psi_1^2} - 1)} \left(Ae^{2E_1/E\psi_1^2} + 2/3\right) \cdot \left(1 - \frac{e^{-2E_1/E\psi_1^2}}{A}\right)^3 \right\} \qquad \text{(III.11)}$$

III.5 ELECTRONIC MULTIPLE SCATTERING

Bohr[22] gives the change in the average square fluctuation in angle, due to electronic collisions, to be:

$$\delta\Omega_e^2 = \frac{m_e}{2M_1 E} . S_e . R(r) . \delta\gamma \qquad \text{(III.12)}$$

where m_e is the mass of an electron,

R(r) is the electron density at a distance r from the string, corresponding to the solution of a Poisson's Equation using the continuum potential, and

S_e is the stopping cross-section per electron and for swift particles, S_e is given by the Bethe-Bloch formula:

$$S_e = \frac{4\pi . Z_1^2 . e^4}{m_e v^2} . \frac{1}{(4\pi\epsilon_0)^2} . L_e \qquad \text{(III.13)}$$

with

$$L_e \approx \ln(2m_e v^2/I) \qquad \text{(III.14)}$$

and I is the mean ionisation potential of the target atom, $I \approx 10 . Z_2$ eV. Foti et al.[18] averages R(r) over the accessible area in transverse space and, using (III.12), (III.13) and (III.14), finds:

$$\left\langle \left(dE_1/d\gamma\right)_e \right\rangle = E \left\langle \left(\delta\Omega^2/\delta\gamma\right)_e \right\rangle = \left[\frac{n . Z_1 . \pi . e^2 . d}{E . 4\pi\epsilon_0} . \frac{E\psi_1^2}{2} . \ln\left(\frac{2m_e v^2}{10 . Z_2}\right) \cdot \left\{ \frac{(Ae^{2E_1/E\psi_1^2} - 1)}{A(e^{2E_1/E\psi_1^2} - 1)} \cdot \left(1 - \frac{e^{-2E_1/E\psi_1^2}}{A}\right) \right\} \right] \qquad \text{(III.15)}$$

Since all the terms in (III.6) have now been obtained in analytic form, and using the Stopping Power, $\frac{dE}{dz}$, tabulated by Ziegler and Andersen[28], the calculation of Random Fraction as a function of depth can be made.

III.6 NUMERICAL CALCULATION OF RANDOM FRACTION AS A FUNCTION OF DEPTH

The average square amplitude of atomic vibrations, ρ^2, in the transverse plane is taken to be 2/3 mean square amplitude, in three dimensions (see Björkqvist et al.[16]) and is calculated using the formula given by Lonsdale[30]:

$$\overline{u^2} = \frac{4{\cdot}364 \times 10^{-18}}{A.\theta} \cdot \left\{ \frac{\Phi(x)}{x} + 0{\cdot}25 \right\} \quad m^2 ,$$

where $\rho^2 = 2/3\,\overline{u^2}$ and

$\Phi(x)$ is the Debye function,

$x = \theta/T$, θ is the Debye Temperature

(θ_{Au} = 170K), and T is the temperature in question. ρ^2 determines the temperature-dependence of

(i) the critical transverse energy, $E_{\perp_c}$, where

$$E_{\perp c} = \frac{Z_1 Z_2 e^2}{4\pi\epsilon_0 d} \cdot \ln\left(\frac{C^2 a^2}{r_c^2} + 1 \right)$$

and $r_c^2 = \rho^2 + a^2$, and

(ii) the rate of increase of transverse energy $\left\langle \frac{dE_\perp}{dz} \right\rangle$.

The numerical calculation was made in the following way: selected values of $E_{\perp_0}$ were obtained by taking successive small decrements of $E_\perp$ from $E_{\perp_c}$. Consider one value, $E_{\perp_0}'$,

<u>At the crystal surface</u>

Total Energy, $E = E_0$

Transverse Energy, $E_\perp = E_{\perp_0}'$

At a small depth interval z (intervals of 100 Å were used in the calculation)

$$\text{Total Energy, } E = E_0 - S(E_0).z = E_1$$

Transverse Energy,

$$E_\perp = E_{\perp 0}' + \left\langle \frac{dE_\perp}{dz} \right\rangle (E_0, E_{\perp 0}').z = E_{\perp 1}'$$

where S(E) denotes the Random Stopping Power, $\frac{dE}{dz}$.

If $E_{\perp 1}' < E_{\perp c}$, then another depth interval is considered with the energies at the back of the second interval given by:

$$\text{Total Energy } E = E_2 = E_1 - S(E_1).z$$

$$\text{Transverse Energy } E_\perp = E_{\perp 2}' = E_{\perp 1}' + \left\langle \frac{dE_\perp}{dz} \right\rangle (E_1, E_{\perp 1}').z$$

and so on for successive intervals, until $E_{\perp n}' \geqslant E_{\perp c}$. nz would then be tabulated and the Random Fraction at nz, $\chi(nz)$ would be calculated from:

$$\chi(n\gamma) = \int_{E_{\perp 0}'}^{\infty} p(E_{\perp 0}).dE_{\perp 0} = \frac{A-1}{Ae^{2E_{\perp 0}'/E\psi_1^2} - 1} \qquad \text{(III.16)}$$

which is obtained by integrating equation (III.4).

The measured component of the Random Fraction caused by scattering of the aligned beam in the disordered surface layer, χ_3, is added to that found from (III.16).

CHAPTER FOUR

GOLD SINGLE CRYSTAL PREPARATION

The crystals used in our experiments must have a sufficiently low concentration of defects distributed through their bulk so that dechanneling by defects is negligible in comparison to that caused by thermally vibrating nuclei and electrons. The crystals must also have minimum surface disorder to minimise the Random Fraction at the surface and to simplify the calculation of the transverse energy distribution of the incident particles.

IV.1 EVALUATION OF CRYSTAL QUALITY

The evaluation of crystal quality is made using three complementary experimental techniques:

(a) Laue diffraction of X-rays, which is used to assess the average quality of the crystal over a depth of several microns,

(b) diffraction of mono-energetic electrons, used to assess the quality of the surface region to depths up to several hundred Angstroms,

(c) Rutherford backscattering-dechanneling, which can be used to determine the amount of surface disorder and to compare the quality of crystals in terms of their dechanneling rates observed over depths up to several microns.

IV.1.1 X-RAY DIFFRACTION

An 18 keV beam of continuous X-rays was used in the standard Laue Back-Reflection arrangement. A description of the interpretation of the

diffraction spot pattern can be found in standard X-ray diffraction texts[31]. For a single crystal, each spot in the diffraction pattern can be identified with a reflection from a particular set of planes in the crystal and the pattern may be analysed to determine the orientation of the crystal with the X-ray beam. For our purposes, however, it is sufficient to note that the diffraction spot from a set of planes in a perfect crystal is circular and has a sharp outline and that any deviations from this are produced by crystal defects. The Laue spots obtained from diffraction quality, freshly-cleaved NaCl, purchased from Harshaw Chemical Company, were used as a reference. The shape and sharpness of the diffraction spots from gold crystals were carefully inspected visually and compared with those in the NaCl pattern, see Fig. IV.1(a) and (b).

X-ray diffraction patterns obtained from NaCl crystals, overlaid with two micron thick gold films, showed strong absorption of the X-rays. Therefore, X-ray diffraction gives an assessment of gold crystal structural quality averaged over several microns.

IV.1.2 ELECTRON DIFFRACTION

The McMaster University electron microscope (Phillips EM300) was used in the reflection transmission mode. Monoenergetic electrons (80 keV or 100 keV in this case) are incident at a glancing angle to the crystal surface, the orientation of which is adjusted to give a Bragg diffraction pattern on a photographic plate.

The electrons are strongly scattered and only those which are diffracted from planes within a few hundred Angstroms of the surface will emerge again from the crystal surface to form the diffraction pattern. Reflection

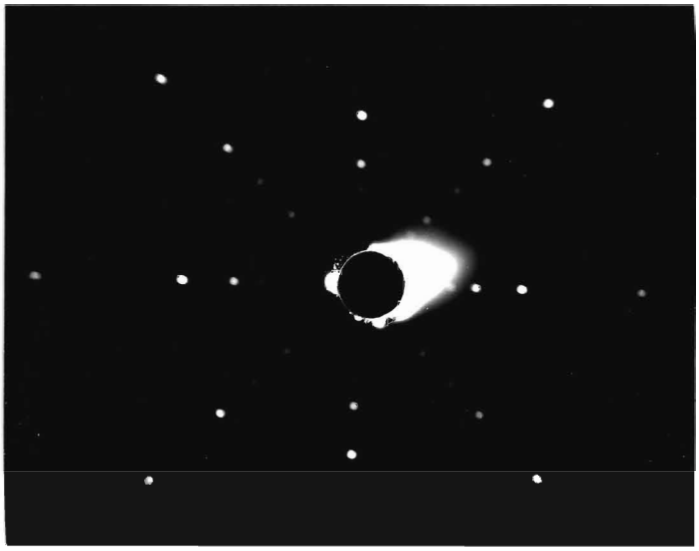

Figure IV. 1(a). X-ray diffraction pattern obtained from the reference NaCl crystal.

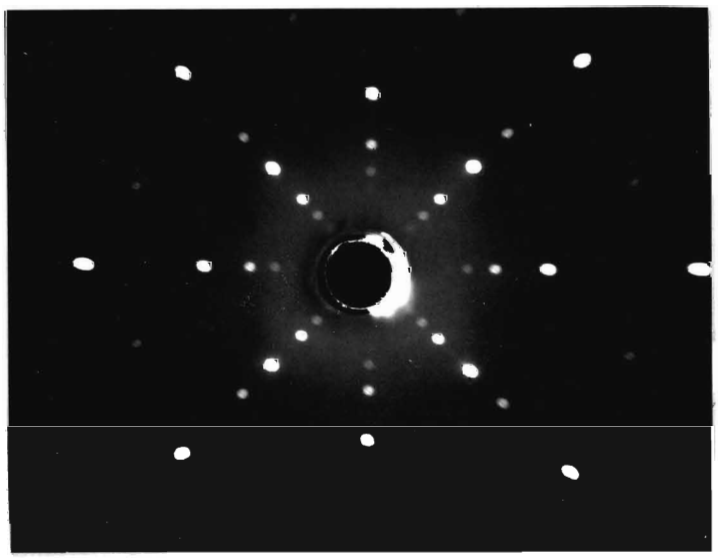

Figure IV. 1(b). Typical x-ray diffraction pattern from a gold crystal.

electron diffraction therefore permits observation of the structure of the near surface region[32]. Figure IV.2 shows diffraction photographs taken of the same gold crystal using X-rays and electrons. The surface structure is revealed as polycrystalline (by electrons) and the underlying bulk as a single crystal (by X-rays). In contrast, Fig. IV.3 shows electron and X-ray diffraction patterns from a gold sample which is a single crystal throughout. The presence of Kikuchi lines, a complex network of pairs of dark and bright lines, superimposed on an electron diffraction spot pattern is an indication of a high quality monocrystalline region near the crystal surface[33].

IV.1.3 RUTHERFORD BACKSCATTERING-DECHANNELING

Crystals, which exhibited good X-ray and electron diffraction patterns, were examined further using MeV He^+ Rutherford Backscattering. Aligned and Random Spectra were taken at room temperature for each crystal. Three spectral parameters have been used in the assessment of crystal quality.

The area of the surface peak in the Aligned Spectrum gives a quantitative measurement of the areal density of displaced gold atoms at the crystal surface[29].

The Aligned Fraction at the surface, χ_{min}, and the rate of increase of random fraction with depth, the dechanneling rate, both increase with crystal defect density and have been used to make the final selection of crystals. Details of these spectra are described in Chapter Two and a comparison of the room temperature aligned spectra for different crystals is shown in Chapter Five.

Figure IV. 2(a). Electron diffraction pattern revealing the polycrystalline structure of the surface of this gold crystal.

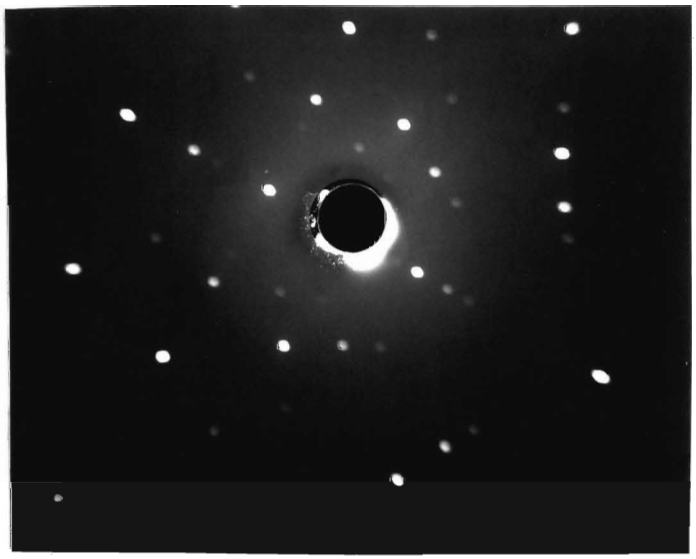

Figure IV. 2(b). X-ray diffraction pattern obtained from the same crystal used to obtain the electron diffraction pattern above. Here, the underlying bulk is shown to be single crystal.

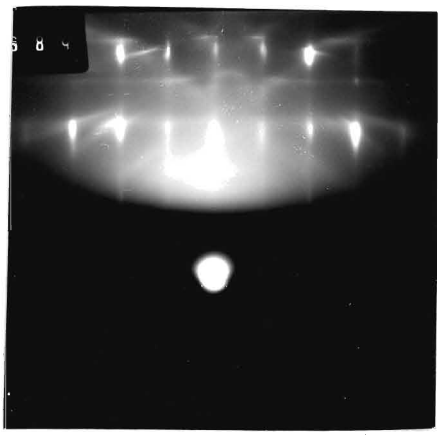

Figure IV. 3(a). Electron diffraction pattern revealing the single crystal structure of the surface of this gold specimen.

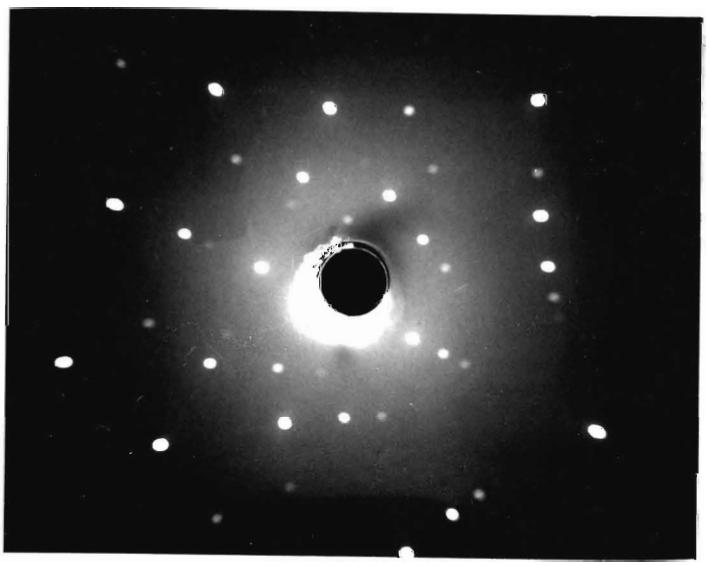

Figure IV. 3(b). X-ray diffraction pattern of the gold sample used in Figure IV. 3(a) showing the underlying bulk to be single crystal.

IV.2 PRODUCTION AND PREPARATION OF SINGLE CRYSTALS

IV.2.1 EPITAXIAL FILMS

Initially, the gold single crystals were produced as thin films, approximately one micron thick, epitaxially grown on NaCl substrates. This was achieved by evaporation of 99.99% pure gold wire on to the freshly-cleaved, in air [100] face of a NaCl substrate. The substrate was held at a temperature of ~450°C in a vacuum of better than 10^{-5} Torr. and the gold condensed on the substrate at a rate of ~20 Å/s. Approximately 50% of the gold crystals grown in this fashion showed a single orientation with the substrate, but they generally had diffuse spots in their X-ray patterns, see Figure IV.4. In addition, Rutherford backscattering measurements showed that these crystals had χ_{min} values between 10% and 15%, in comparison with the theoretical value for a defect-free gold crystal of ~2.5%. In order to reduce the concentration of defects in the epitaxial gold films, these films must be annealed. This required the development of difficult techniques to remove the film intact from the NaCl substrate and to support the film during annealing. Therefore it was decided to abandon this approach to the production of gold single crystals and turn attention to the problem of polishing and annealing of crystals sectioned from bulk gold single crystals.

IV.2.2 BULK CRYSTALS

Bulk gold single crystals were obtained from Chalk River Nuclear Laboratories[34]. They were 7-10 mm in diameter and had been cut, by spark erosion, into slices of thickness between 2 and 4 mm. All samples had been mechanically polished with fine powders of 0.25 μm diameter.

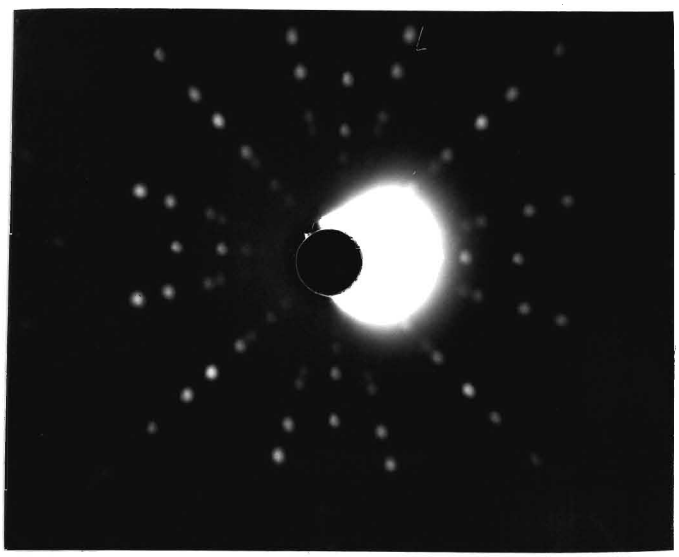

Figure IV. 4(a). X-ray diffraction pattern of epitaxial Au crystal having more than one preferred orientation.

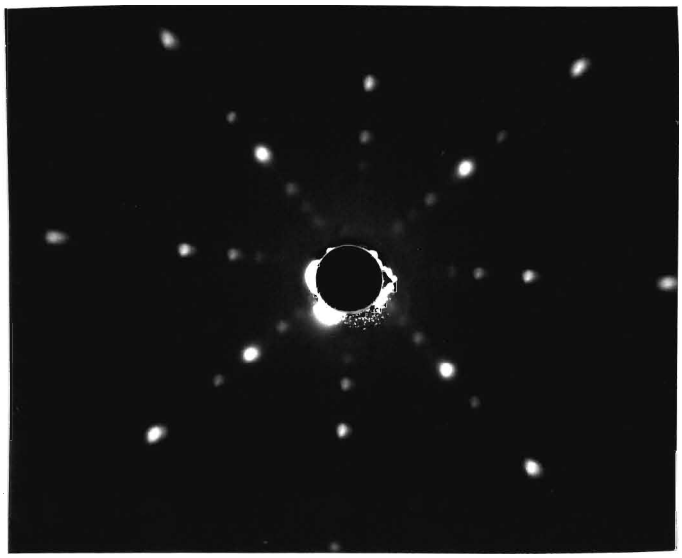

Figure IV. 4(b). X-ray diffraction pattern of an epitaxial Au crystal having one preferred orientation, but having diffuse spots.

X-ray diffraction patterns were then taken of these gold crystals, as received, which showed a dense diffuse background and faint streaks, see Figure IV.7(a). The crystals were thus assumed to have heavily damaged surface regions extending several microns below their outer faces.

The further treatment of the crystal, which was required in order to remove the dense surface disorder and any defects in the underlying bulk, was developed empirically. Metal crystals, such as tungsten and copper, suitable for channeling studies have been produced at C.R.N.L. by using the following sequence of stages in preparation: annealing, cutting, mechanical polishing, vibratory polishing, and finally electropolishing. However, this preparation was found to be totally inadequate for gold crystals[35]. Gold is exceptionally soft and would sustain deep mechanical damage during cutting and mechanical polishing. Thus, a further annealing stage may be required after polishing.

It was found that a combination of electropolishing and annealing in the final stages of preparation produces well-ordered gold single crystals in which defect dechanneling at room temperature appears to be negligible. A description of the electropolishing and annealing stages, used in this project, follows.

IV.2.3 ELECTROPOLISHING PROCEDURE

A diagram of the apparatus used is shown in Figure IV.5. The standard electrolyte for gold[36] was used (22 g chromic acid: 135 c.c. acetic acid:7 c.c. water). The correct operating state of the polisher was determined by observing the crystal surface topography produced as a function of the cell voltage. Figure IV.6 shows the rough surface due to

Figure IV. 5

The Electropolishing Rig

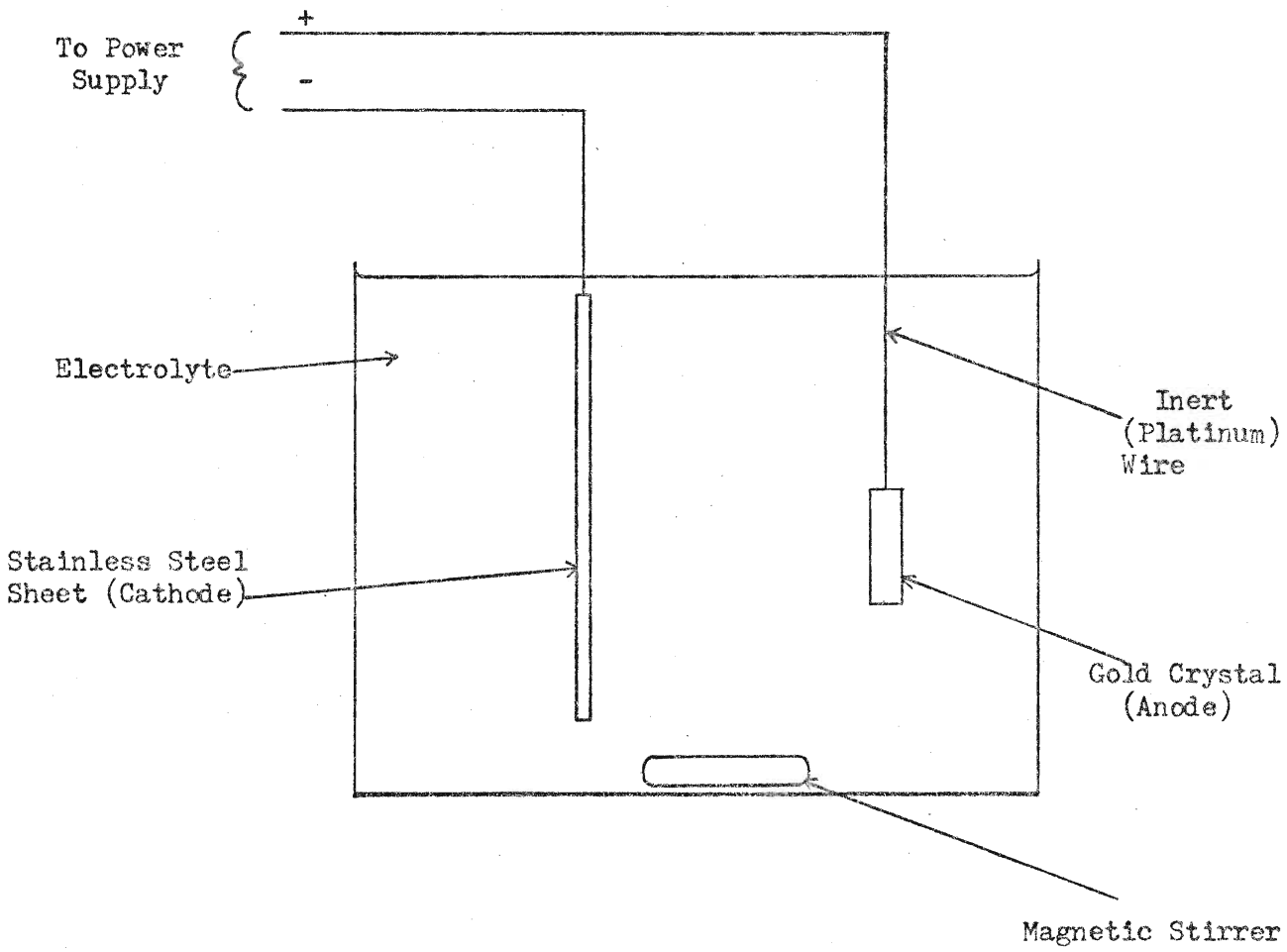

chemical etching when the cell voltage was too low and the smooth surface produced by electropolishing when the cell voltage was at 22 volts (the operating voltage). The polishing rate was found to be approximately 35 microns per hour and approximately 50 microns was normally removed.

Figure IV.7 shows the X-ray diffraction patterns taken before and after electropolishing. The polishing removes the dense surface disorder and leaves a single crystal with a significant defect density as evidenced by the diffuse, structured, Laue X-ray spots, see also Figure IV.9(a), (b) and (c). The structure in the spots is assumed to be due to extended defects, for example, edge dislocations and low-angle tilt boundaries.

IV.2.4 ANNEALING MECHANISMS

The mechanisms involved in annealing are not yet fully understood[37]. However, some relevant information is available concerning defects in crystals[38]:

(a) extended defects, such as edge dislocations and low-angle tilt boundaries, are mobile at high temperatures (however, dislocations moving in different planes can interact at the intersection of these planes and become immobile or sessile),

(b) the equilibrium concentration of simple defects, such as mono-vacancies, is related to the crystal temperature by a Boltzmann factor, i.e., C_{1V} is proportional to $e^{-E_{1V}/kT}$, where E_{1V} is the energy required to create a monovacancy,

(c) the creation of a vacancy requires the proximity of a "sink" for the de-sited atom, such as a crystal surface, grain boundary, tilt boundary or edge dislocation.

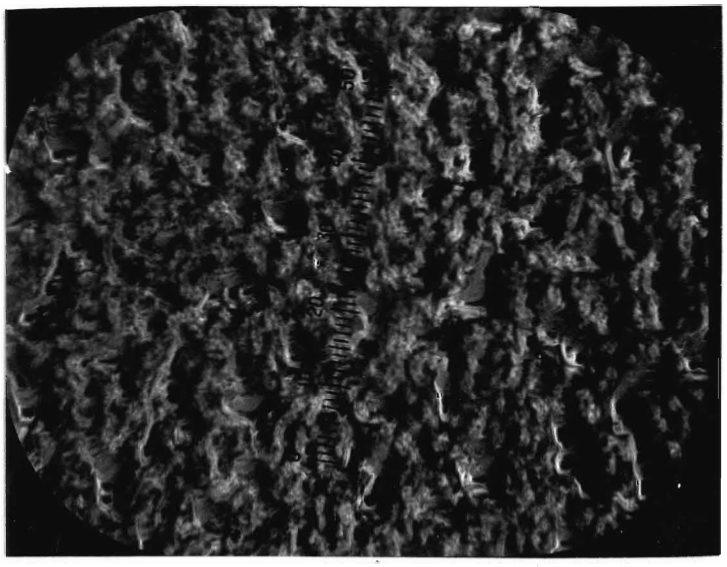

Figure Iv. 6(a). Rough surface caused by chemical etching. (One centimetre on the photograph represents approximately 35 microns on the gold surface.)

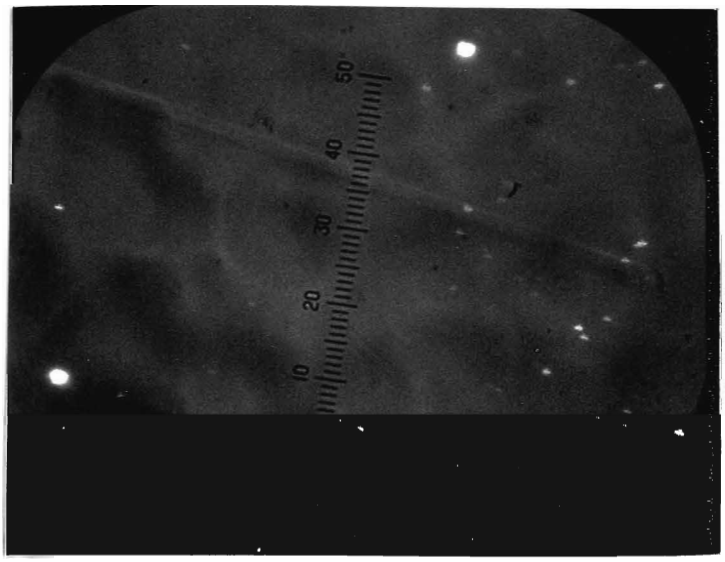

Figure IV. 6(b). Smooth surface produced by electropolishing.

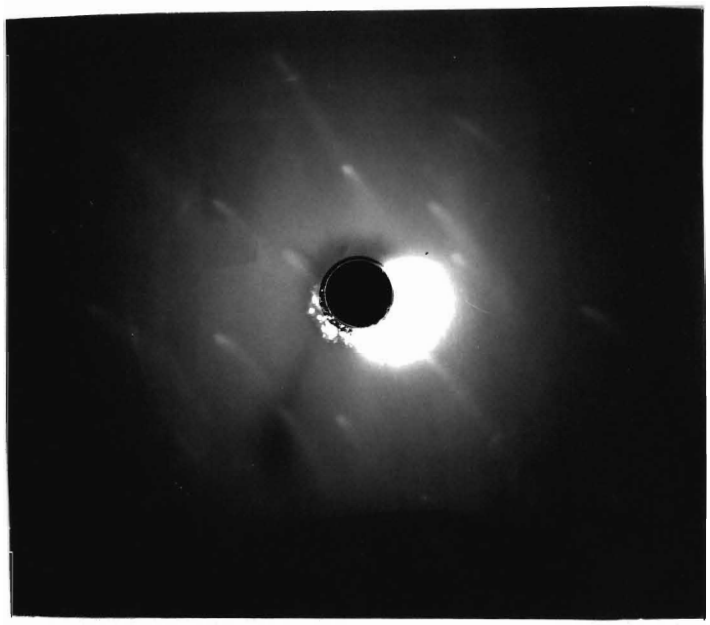

Figure IV. 7(a). X-ray pattern before electropolishing.

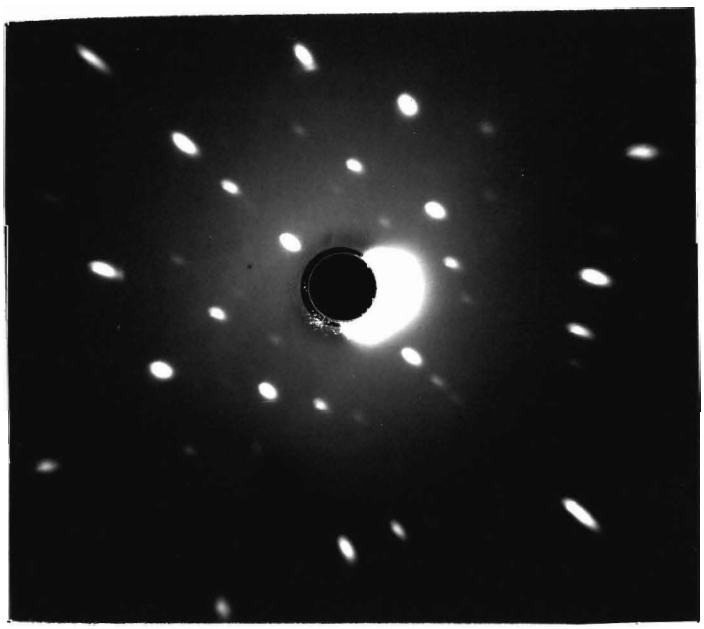

Figure IV. 7(b). X-ray diffraction pattern after electropolishing.

If the temperature of the gold crystal is held near its Melting Point (1063°C) for a long time, some of the extended defects will become mobile and move out to the crystal surface. It is suggested that the large number of atoms re-sited in sessile extended defects at this temperature may cause a re-arrangement of the configuration of these defects into smaller, more mobile defects, such as divacancies and trivacancies.

After annealing, the temperature of the annealing system is reduced very slowly, so that the system retains thermal equilibrium and the concentrations of the simple defects will be the equilibrium values appropriate to the instantaneous temperature.

IV.2.5 ANNEALING PROCEDURE

A photograph of the vacuum annealing chamber is shown in Figure IV.8. The thermocouples were calibrated against the Melting Points of gold, silver and lead. The Ultra High Vacuum pumping system kept the pressure below 10^{-7} Torr. throughout annealing. The temperature reduction was automated using electric motors.

Figure IV.9 shows a sequence of X-ray diffraction photographs which were taken during the development of the annealing procedures. (This crystal had received some electropolishing at C.R.N.L.). Rather little improvement in single crystal quality is evident following the 14 hour anneal at 665°C. Clearly shown is the significant improvement produced by the 1000°C anneal and the benefit of prolonged annealing (60 hours versus two hours) at this temperature.


CAUTION!

Figure IV. 9(a). Before annealing.

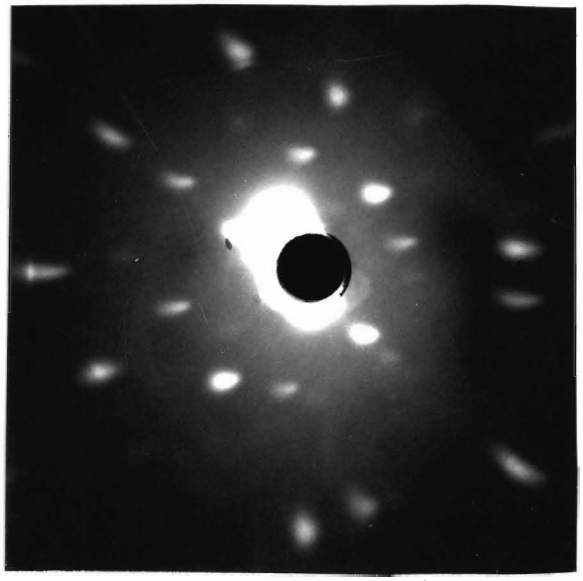

Figure IV. 9(b). After 14 hr. anneal at 666° C.

Figure IV. 9(c). After 2 hr. anneal at 1000° C.

Figure IV. 9(d). After 60 hr. anneal at 1000° C.

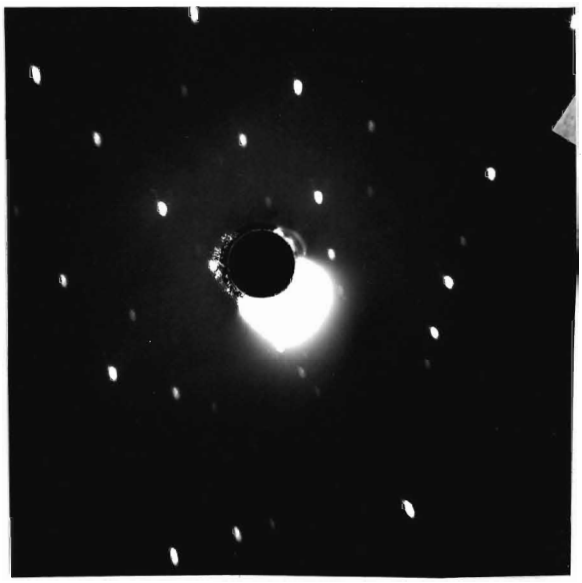

The standard annealing procedure adopted was:

(a) the crystal was carefully cleaned in hot trichloroethylene, isopropyl alcohol and acetone,

(b) it was then placed in the annealing chamber, and, with the vacuum reduced below 10^{-7} Torr, the temperature was raised at a rate of 100°C/hour,

(c) the crystal was annealed at 1000°C for between 60 and 100 hours,

(d) the temperature was reduced from 1000°C to 750°C at a rate of approximately 10°C/hour, then from 750°C to room temperature at a rate of approximately 22°C/hour.

The crystal was mounted on an aluminium backing plate (see Figure IV.10), when not actually in the annealing or electropolishing systems, to minimise damage during handling.

IV.2.6 RESULTS OF CRYSTAL PREPARATION

The crystal used to take the X-ray diffraction patterns in Figure IV.9 was subsequently found to have single crystal electron diffraction spots and had a χ_{min} value of 2.7% (theoretical value ~2.5%) when Rutherford Backscattering dechanneling measurements were made at room temperature.

Figure IV.11 shows X-ray and electron diffraction patterns of a crystal taken during the standard electropolishing and annealing procedures outlined in this Chapter. Crystals with these diffraction characteristics were selected for channeling/dechanneling measurements. Further selection of best quality crystals was sometimes possible on the basis of observable differences in the dechanneling rates at room temperature and finally at low temperatures of ~41°K.

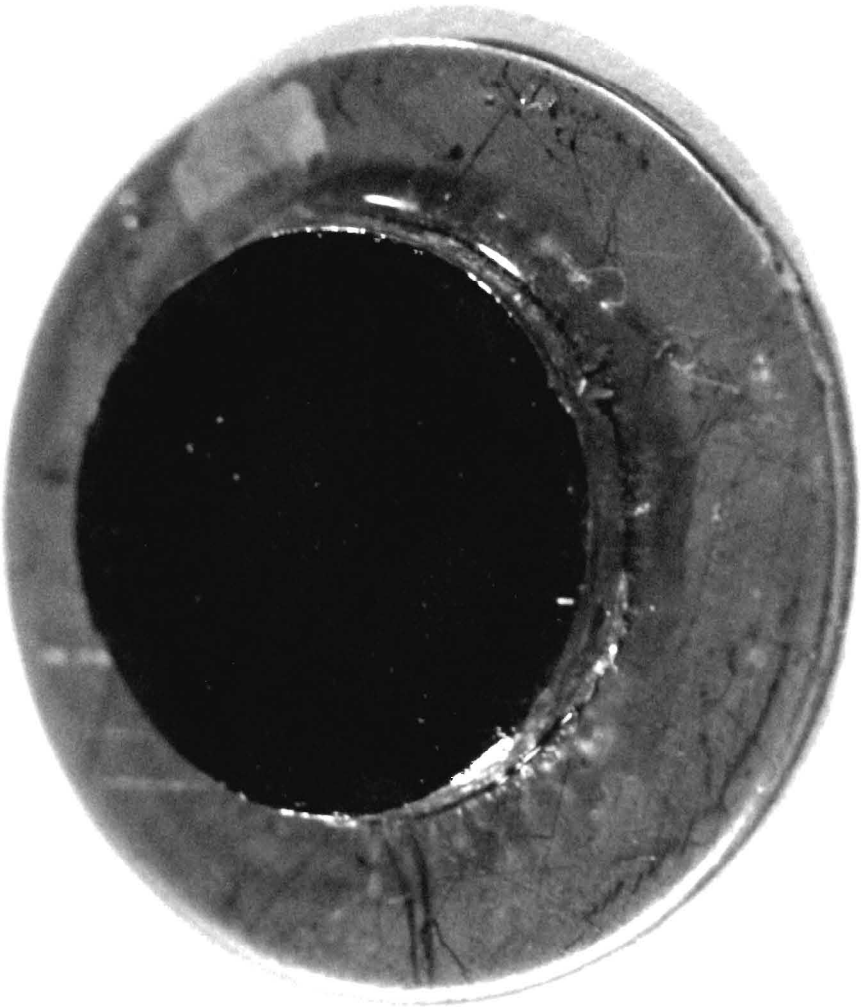

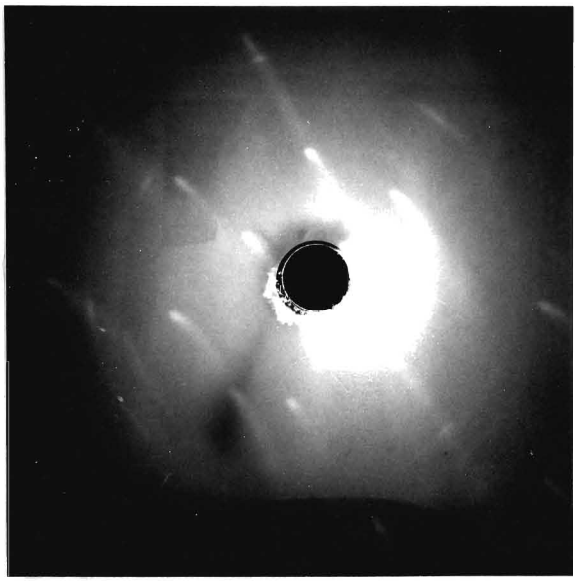

Figure IV. 11(a). X-ray diffraction pattern prior to treatment.

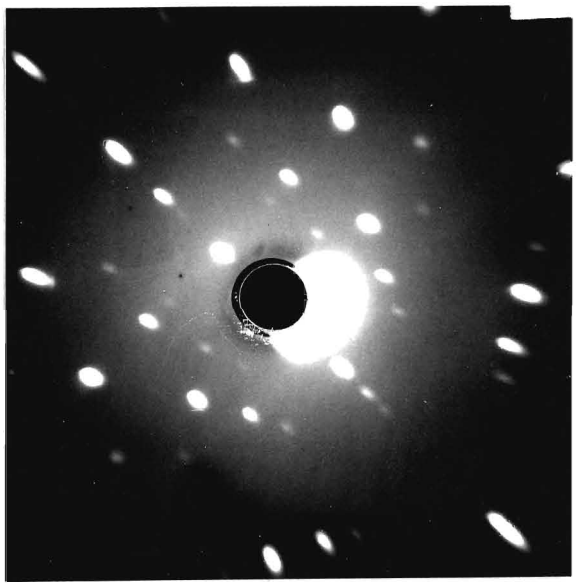

Figure IV. 11(b). X-ray diffraction pattern after electro-polishing.

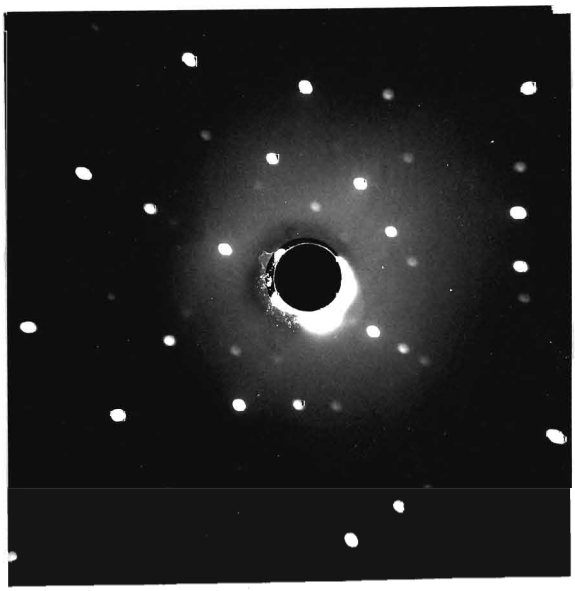

Figure IV. 11(c). X-ray diffraction pattern after annealing.

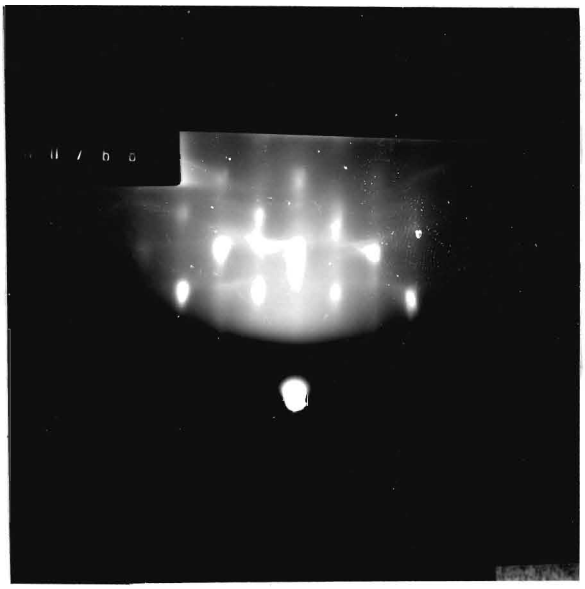

Figure IV. 11(d). Electron diffraction pattern after annealing.

CHAPTER FIVE

DECHANNELING IN GOLD

V.1 THE CHALK RIVER NUCLEAR LABORATORY (C.R.N.L.) CHANNELING FACILITY

Backscattering and channeling measurements were made using the 11° arm of the 3 MeV Van de Graaff accelerator at C.R.N.L. In this excellent facility, it was possible to change from 1 MeV H^+ to 2 MeV He^+ beams and vice versa within approximately 15 minutes. Two 1 mm diameter apertures placed 2 metres apart in the beam line defined the beam direction, gave a beam divergence of 3.0×10^{-2} degrees and a beam size of less than 1.5 mm diameter on the crystal.

The main components of the backscattering chamber are shown in Figure V.1. The two axis goniometer is used to provide Azimuthal and Tilt Rotation of the crystal in order that it can be aligned with the beam (Figure V.2). The silicon detector is positioned at an angle of 150° to the incident beam direction, in the vertical plane, and subtends an angle with respect to the crystal which is large compared to the critical angle for blocking. The region around the crystal and detector is enclosed by a copper cylinder which collects the beam-induced secondary electron emission from the crystal. This current is added to the current which passed through the crystal to give a measurement of the beam current incident on the crystal. The liquid nitrogen cold finger aids rapid evacuation of the scattering chamber, minimises the contamination of the crystal surface in the backscattering chamber, and cools the silicon detector to its maximum energy resolution

Figure V. 1. SCHEMATIC SCATTERING CHAMBER

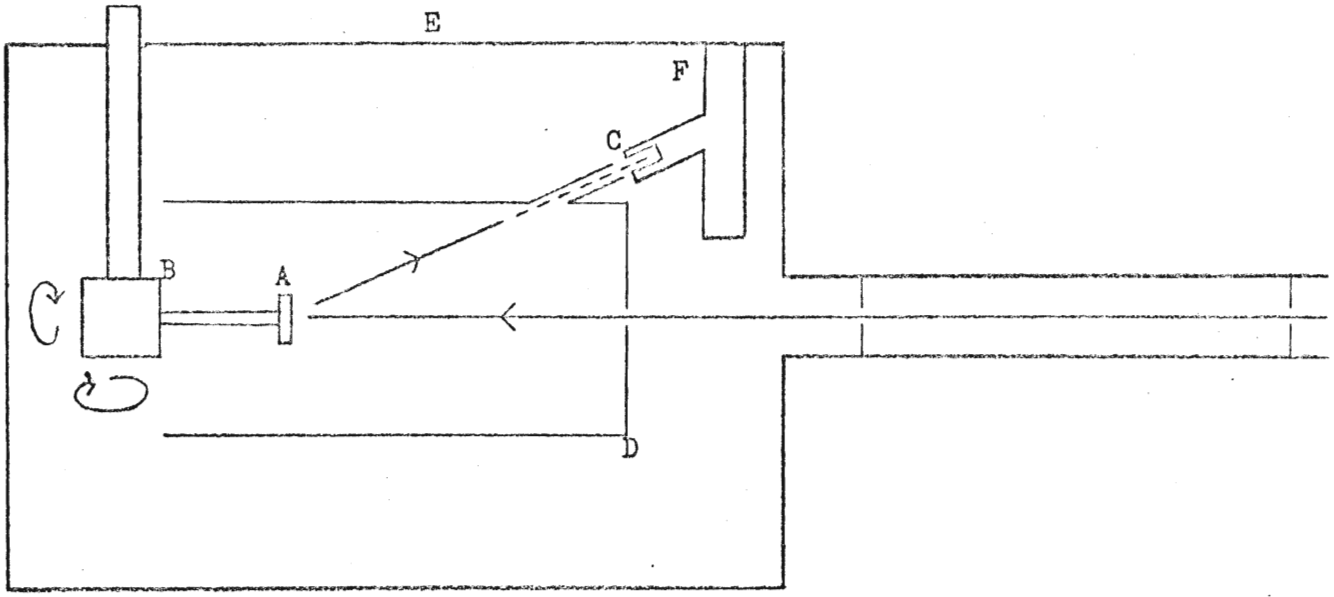

A - Crystal
B - Goniometer
C - Si Detector
D - Cu Shield
E - Vacuum Chamber
F - Cold Finger

Figure V. 2. GONIOMETER AXES

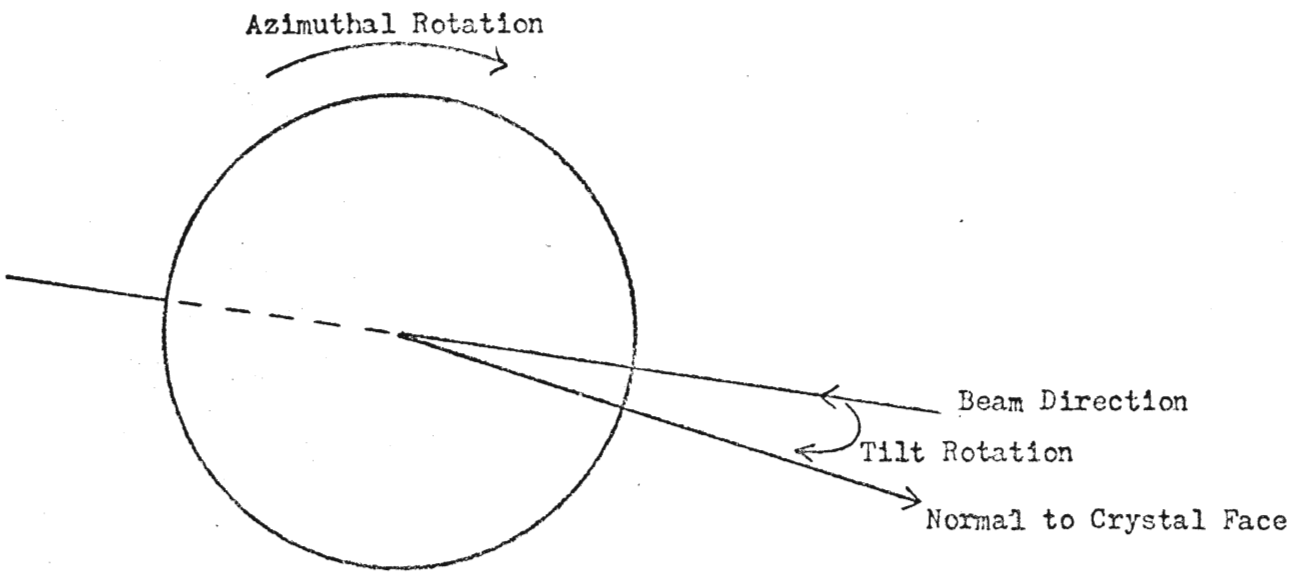

(10-15 keV) temperature. Controlled temperature variation, in the range 40°K to 293°K range, is provided by a two-stage CRYOMECH cooling system. The lower temperature stage is connected to the copper shield to minimise the condensation of residual gases on the crystal surface. The higher temperature stage is connected to the goniometer head. Thermocouples and heaters accompany both stages.

A block diagram of the backscattered particle detection and energy analysis system is shown in Figure V.3. The system functions as follows: a backscattered particle, of energy E_1, enters the silicon detector, producing an amplified voltage signal V_1, directly proportional to E_1, at the M.C.A. The M.C.A. then records a count in a channel, the channel number of which is directly proportional to V_1. The pulse generator is used to simulate detector pulses in order to calibrate the channel number scale of the M.C.A. directly in energy. The voltage scale on the pulse generator is first converted to an energy (MeV) scale, by calibration with reference to alpha particles of known energy from an americium-241 radioactive source. The ratiometer measures the instantaneous ratio of the number of backscattered particles to the beam current. The ratiometer is used in the initial alignment procedure, since a minimum reading on the ratiometer is obtained whenever a crystal axis or plane is aligned with the beam.

V.2 PROCEDURE FOR DECHANNELING MEASUREMENTS

Before the crystal was placed in the backscattering chamber, the alignment of the beam, with respect to the goniometer, was checked. This was done by recording the trace of a "burn" mark produced by the beam impacting on paper fastened to the goniometer head during azimuthal rotation.

Figure V. 3. Block Diagram of Particle Detecting and Energy Analysis System.

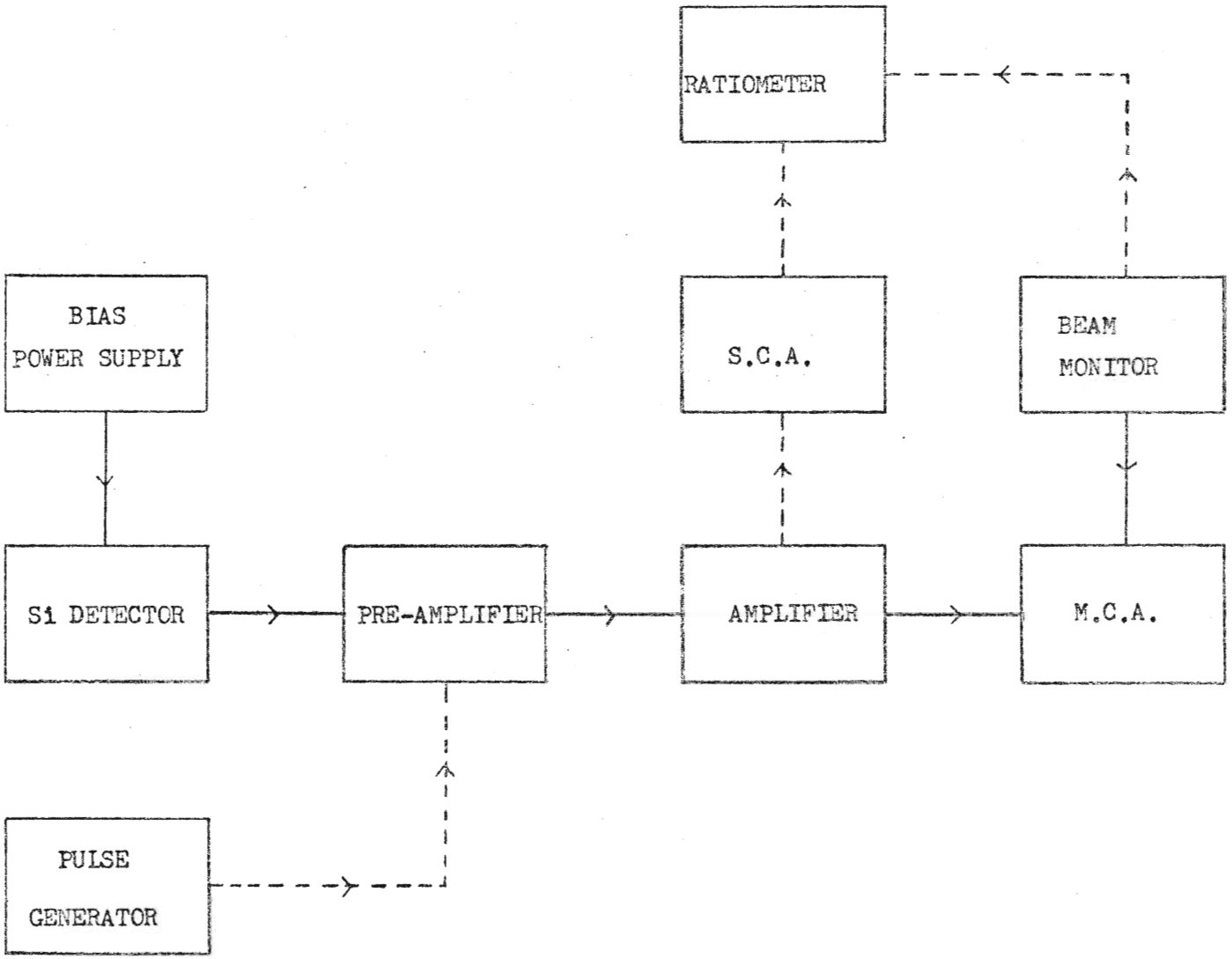

The aluminium backing plate, which held the gold crystal, was then fastened to the goniometer head. The gold crystal had not been touched itself since annealing, all handling was done via this backing plate.

The chamber was evacuated below 10^{-5} Torr, the cold finger chilled, and the M.C.A. was calibrated with respect to the pulse generator. A 1 MeV proton beam was used for crystal alignment since proton-induced damage occurs at a greater depth in the crystal than that examined by the 2 MeV He^{+} beam, see Figure V.4. Damage to the crystal is also minimised by stopping the beam when backscattering was not being recorded.

V.2.1. ALIGNMENT OF <110> CRYSTAL AXIS WITH THE BEAM

The method used to obtain an approximate alignment of the beam with the required channel axis is described in Appendix B. With the channel axis and beam approximately aligned, the goniometer tilt and azimuthal co-ordinates were ϕ' and θ'. The S.C.A. rate, which is the backscattered yield for a given beam fluence, was measured as a function of both ϕ and θ around ϕ' and θ'. The <110> axial dip traced out during these tilt and azimuthal scans is shown in Figures V.5 and V.6. It can be seen from these scans that the centre of the dip can be determined to approximately 0.1°, which is therefore the limit of the precision of alignment using this method. The final precise alignment was achieved by taking aligned spectra, for a given beam fluence, at different tilt angles slightly offset to the nominal aligned position in order to find the position which gave an aligned spectrum

Figure V. 4. Aligned Spectra for 1MeV Protons on Gold (a) before and (b) after radiation damage. Channel Number 317 is equivalent to a depth of 10000 Angstroms.

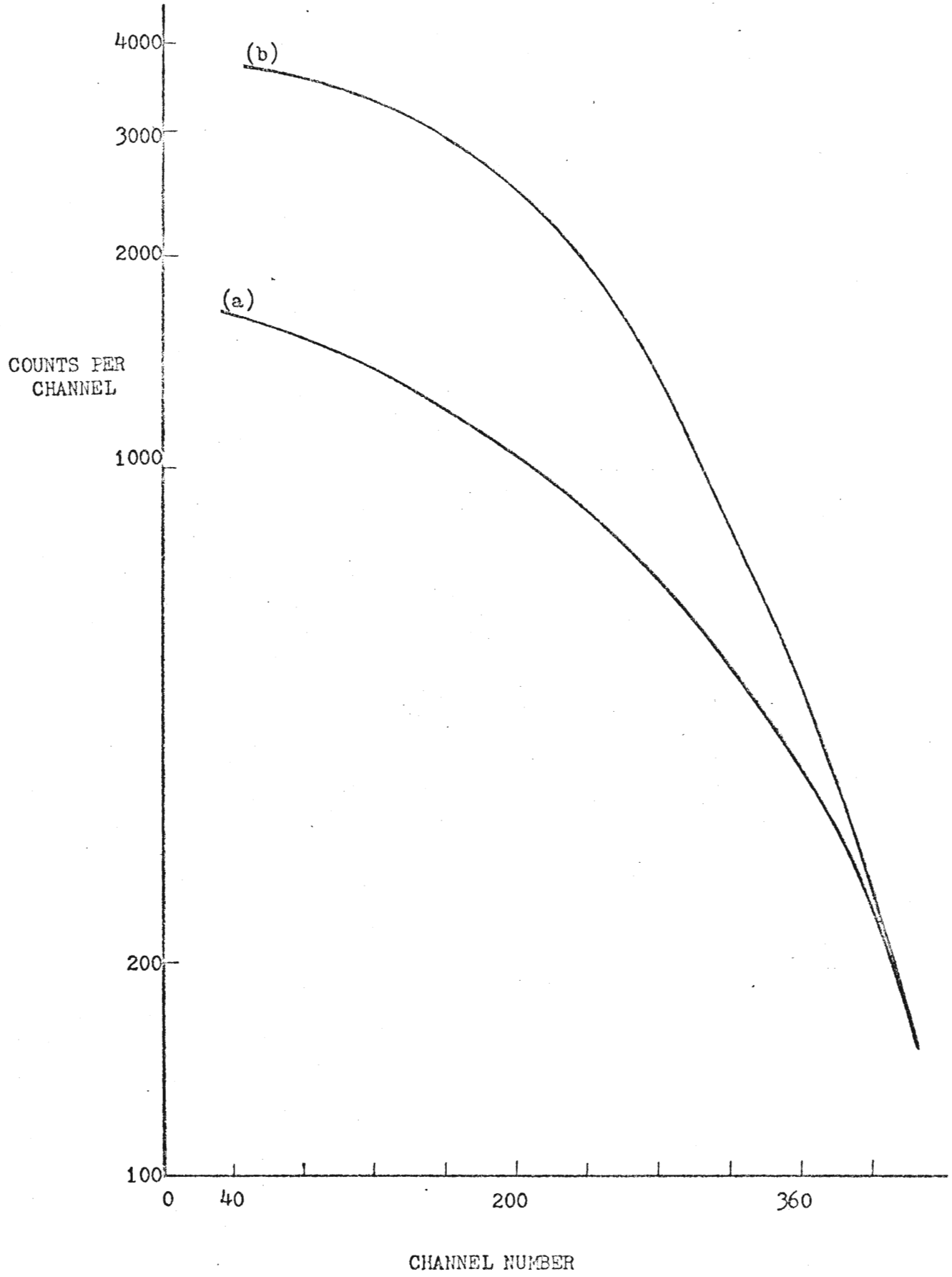

Figure V. 5. Tilt Scan

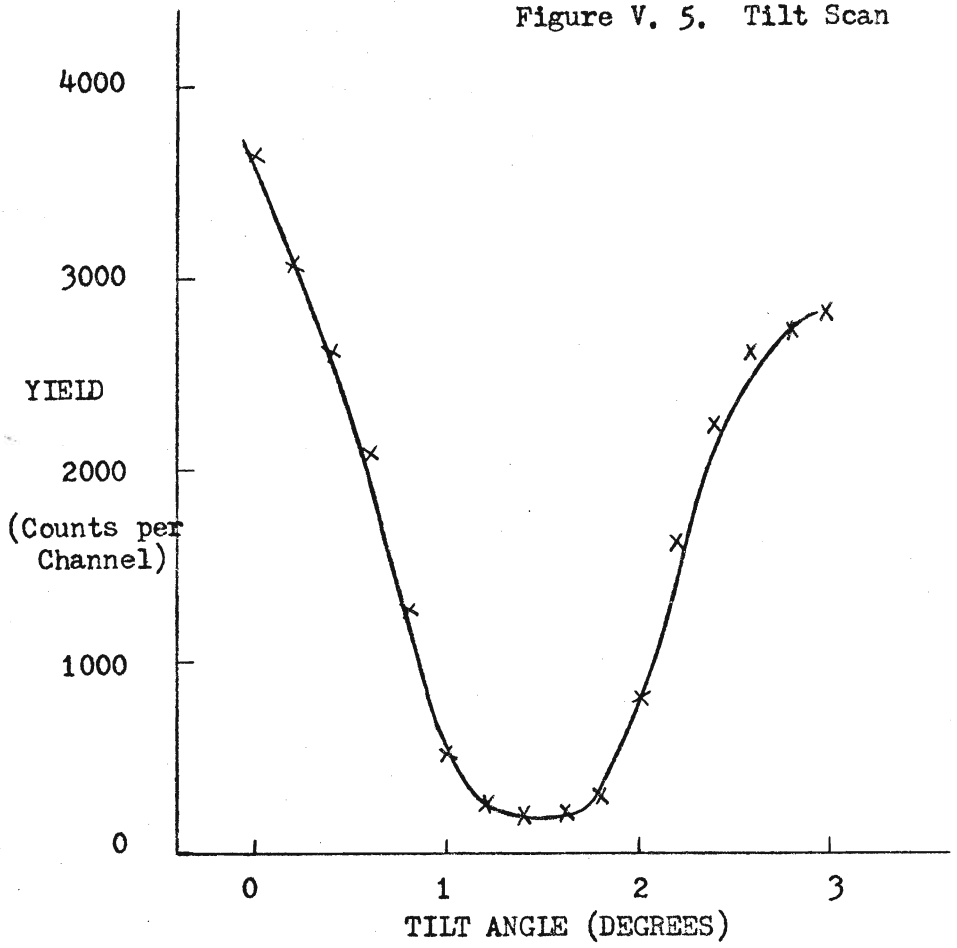

Figure V. 6. Azimuthal Scan

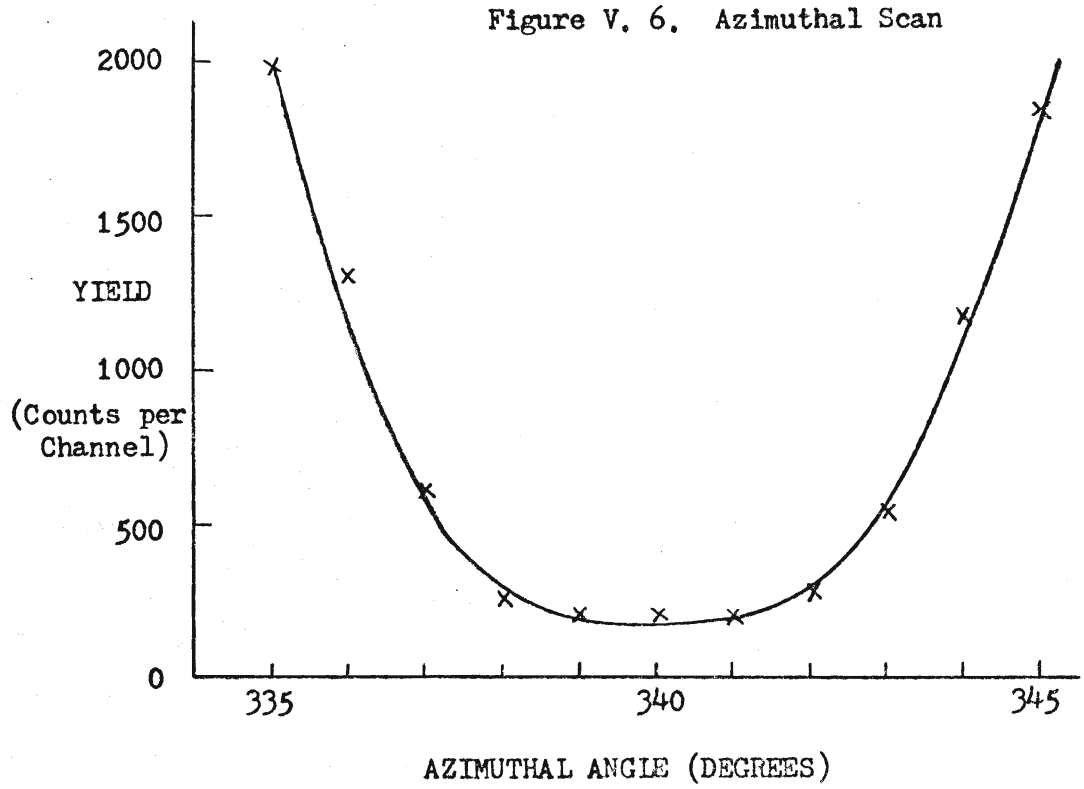

of minimum dechanneling rate. Thus the final alignment can be made to better than 0.1°, see Figure V.7. Once a crystal was precisely aligned, aligned spectra were recorded using 1 MeV H^+ and 2 MeV He^+ beams at room temperature. The dechanneling rates of these spectra were compared from crystal to crystal, see Figure V.8. Any crystal, which had a dechanneling rate significantly higher than the others, was considered to exhibit defect dechanneling and was rejected from low temperature studies.

V.2.2. SPECTRA RECORDING

A crystal, which did not exhibit defect dechanneling, was then cooled to approximately 40°K. With the channel axis still aligned to the beam direction, aligned spectra were recorded as a function of increasing temperature using the 2 MeV He^+ beam. Before each spectrum was recorded, any background leakage current into the Beam Monitor electrometer/integrator was minimised (to less than 1% of the beam current) by zeroing the electrometer. However, we still found that variations in the spectrum counting rate of up to 5% occurred, for a given beam fluence. This variation must therefore be considered to give the limit of the precision in calculating the aligned and random fraction values from the measured backscattered spectra.

The random spectrum was taken at room temperature following completion of the set of aligned spectra. The crystal was tilted so that the beam direction did not coincide with a major crystallographic direction and the crystal was azimuthally rotated, to minimise the channeling effect during the recording of the random spectrum.

Figure V. 7. Aligned Spectra for different Tilt Angles. 1MeV Protons on Gold.

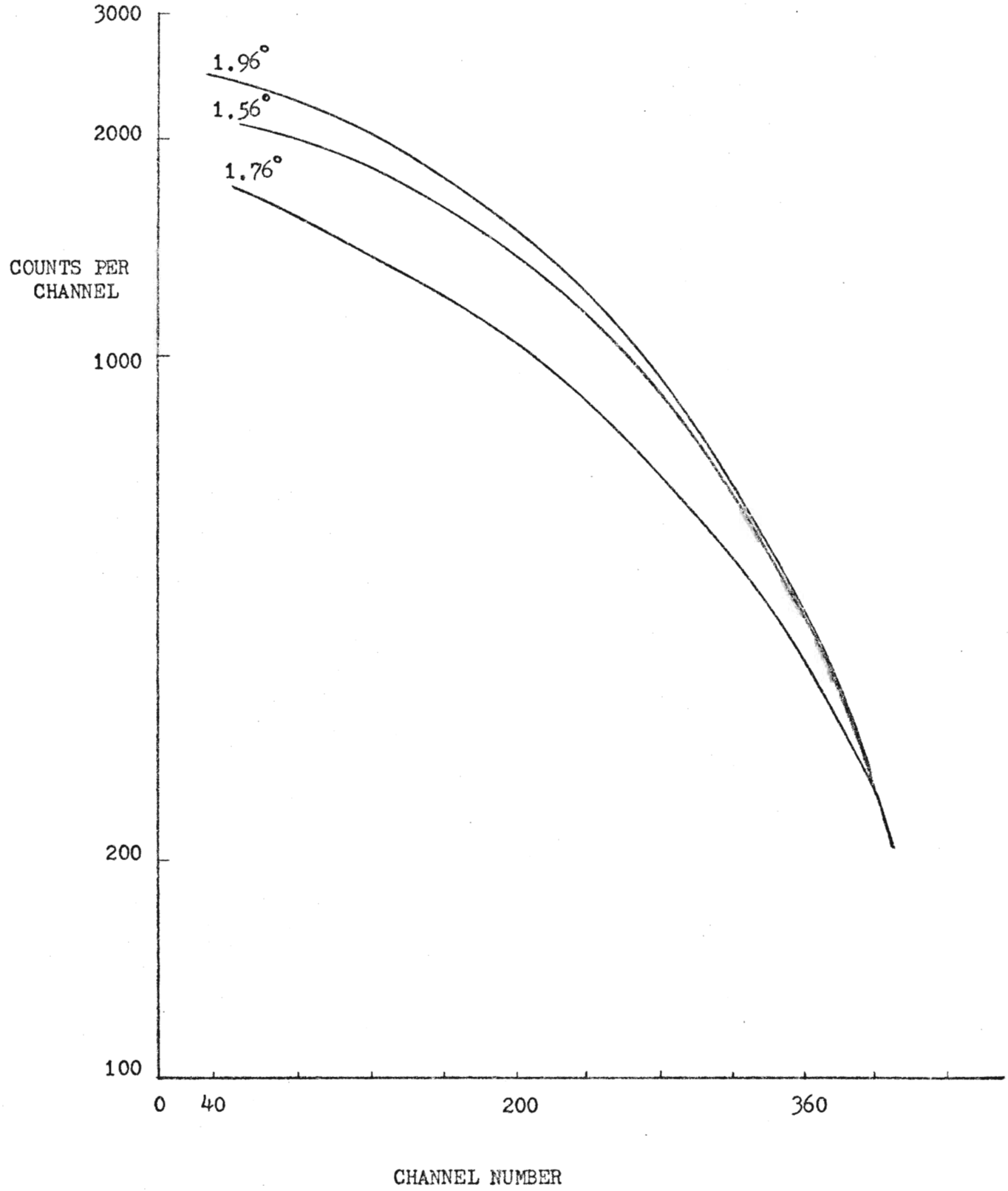

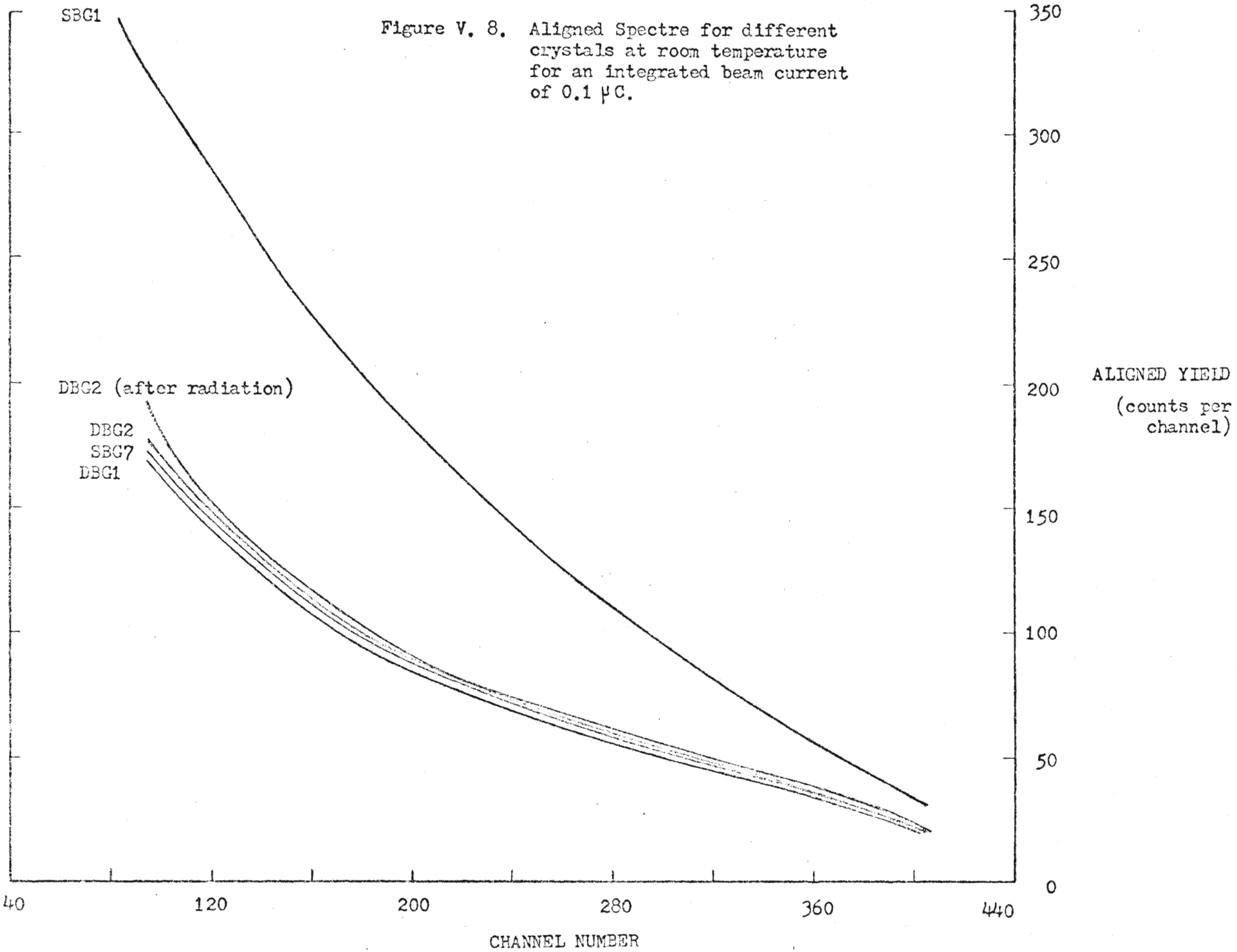

Figure V. 8. Aligned Spectre for different crystals at room temperature for an integrated beam current of 0.1 μC.

The total beam fluence on each crystal during the recording of the aligned spectra was approximately 2 x 10^{15} atoms/cm^2 and 2 x 10^{14} atoms/cm^2 for the random spectra.

V.3. RESULTS OF DECHANNELING MEASUREMENTS

Figure V.8 shows the room temperature aligned spectra for four crystals, three of which have the same dechanneling rate, within the precision of measurement, and the other (SBG1) exhibiting defect dechanneling. Figures V.9(a) and V.9.(b) show the aligned spectra as a function of temperature for DBG1 and DBG2, respectively, using 2 MeV He^+. The random spectra for SBG7, DB1 and DBG2 are shown in Figure V.10; in Figure V.11, the aligned spectra of DBG1 and DBG2 at low temperatures are compared. (The M.C.A. recorded data for all spectra of DBG1 and DBG2 are given in Appendix C.) Although the dechanneling rates at room temperature were the same for DBG1 and DBG2 (Figure V.8), at low temperatures there were significant differences (Figure V.11). Since DBG1 exhibited the lower dechanneling rates, it was taken to represent more closely a defect-free crystal and its spectra were used later in the determination of the measured random fraction versus depth spectra, which were compared with theoretical spectra calculated for defect-free (perfect) gold single crystals.

Figures V.12 and V.13 show the surface peak yield in the aligned spectra, as a function of temperature, for DBG1 and DBG2, respectively.

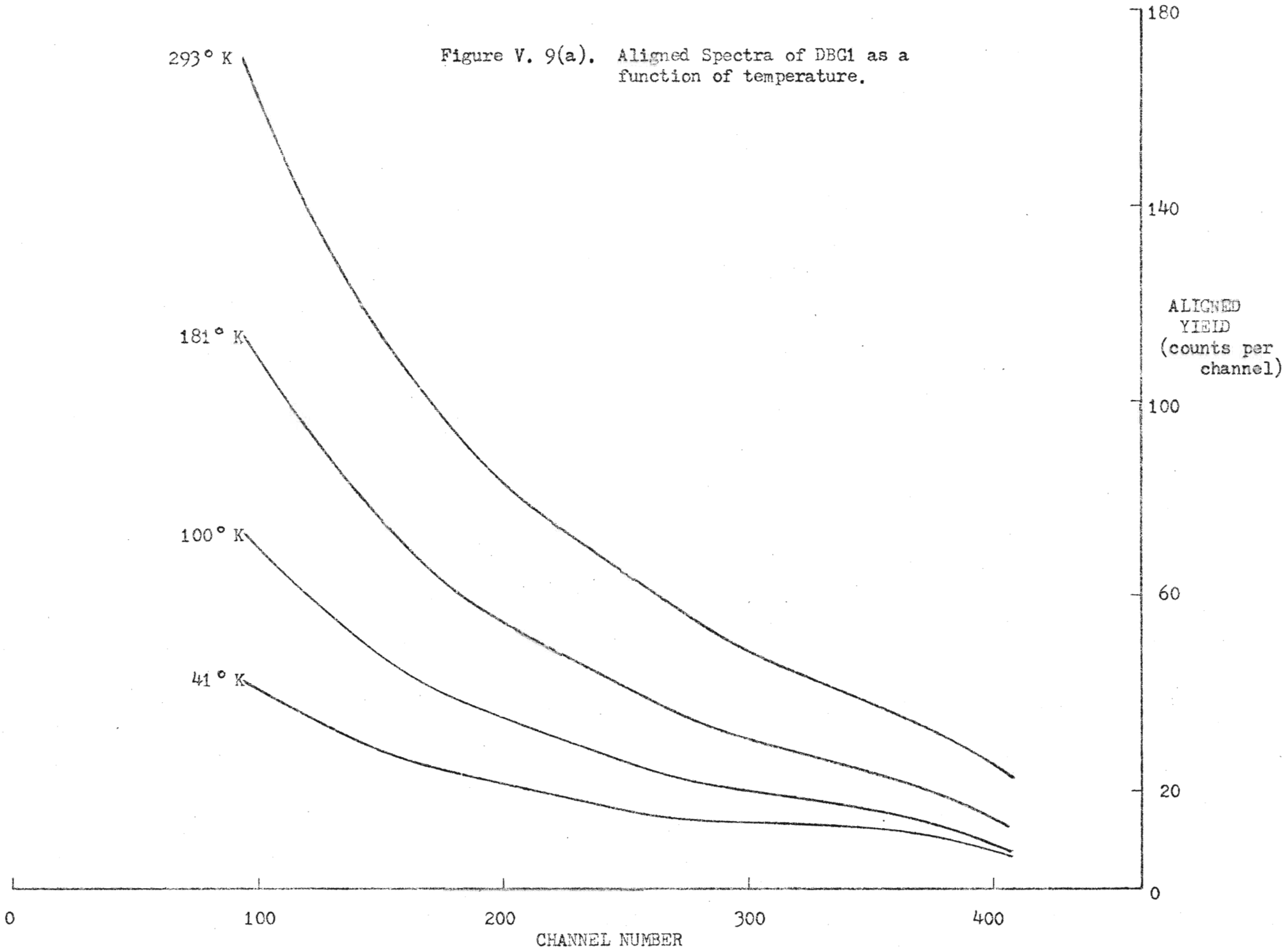

Figure V. 9(a). Aligned Spectra of DBG1 as a function of temperature.

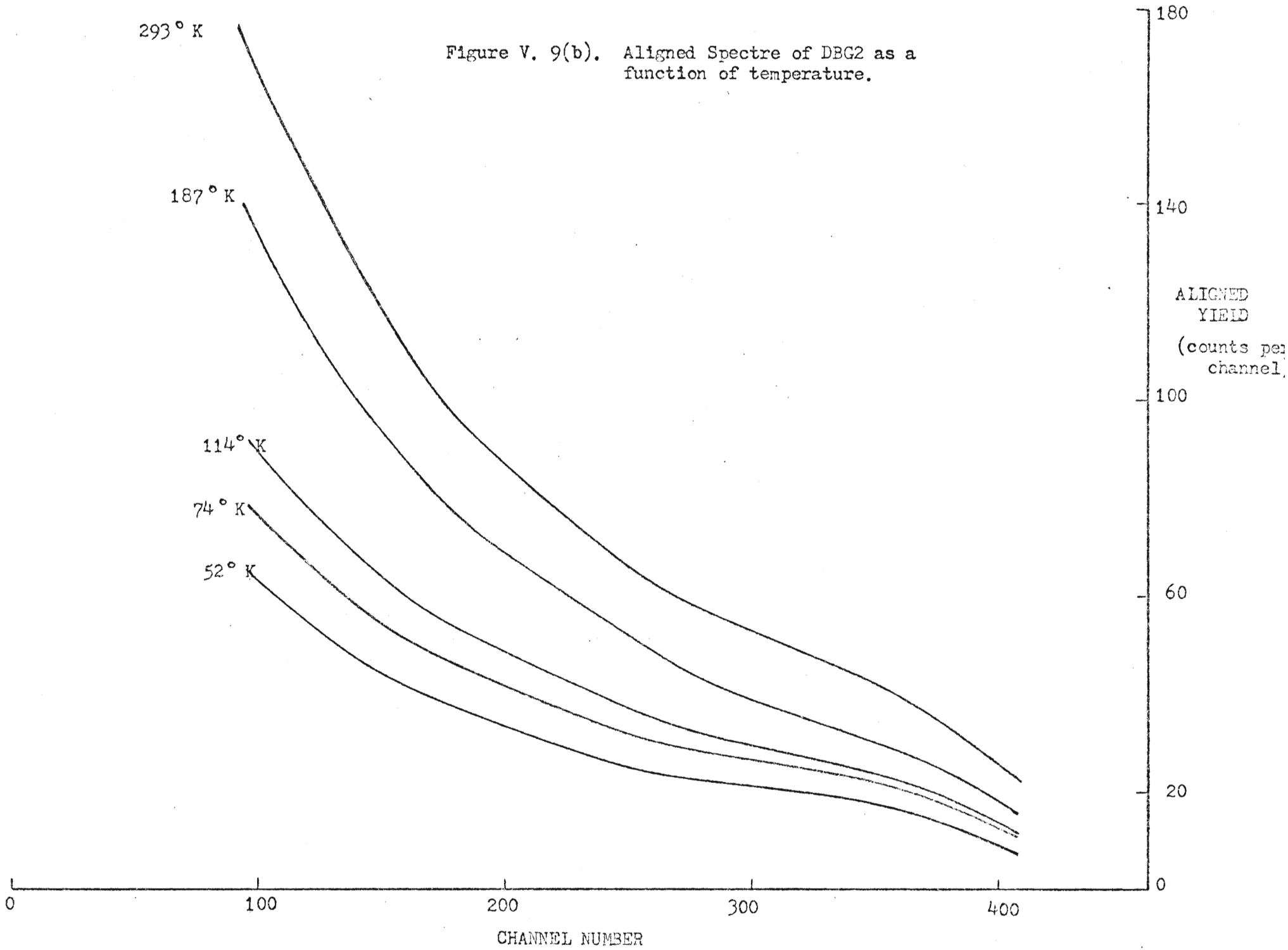

Figure V. 9(b). Aligned Spectre of DBG2 as a function of temperature.

Figure V. 10. Measured Random Spectra

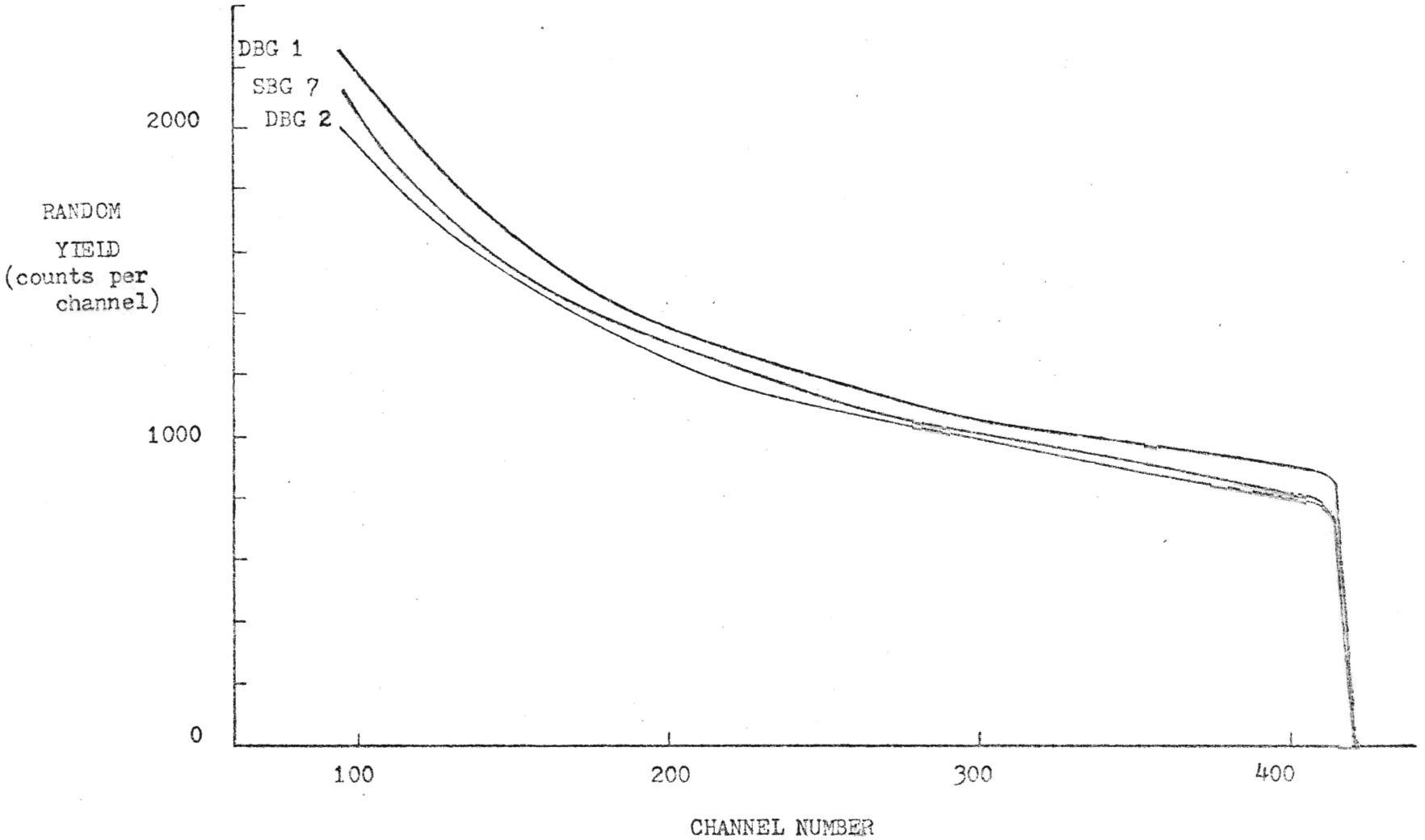

Figure V.11. Comparison of Aligned Spectra of DBG1 and DBG2 at low temperatures.

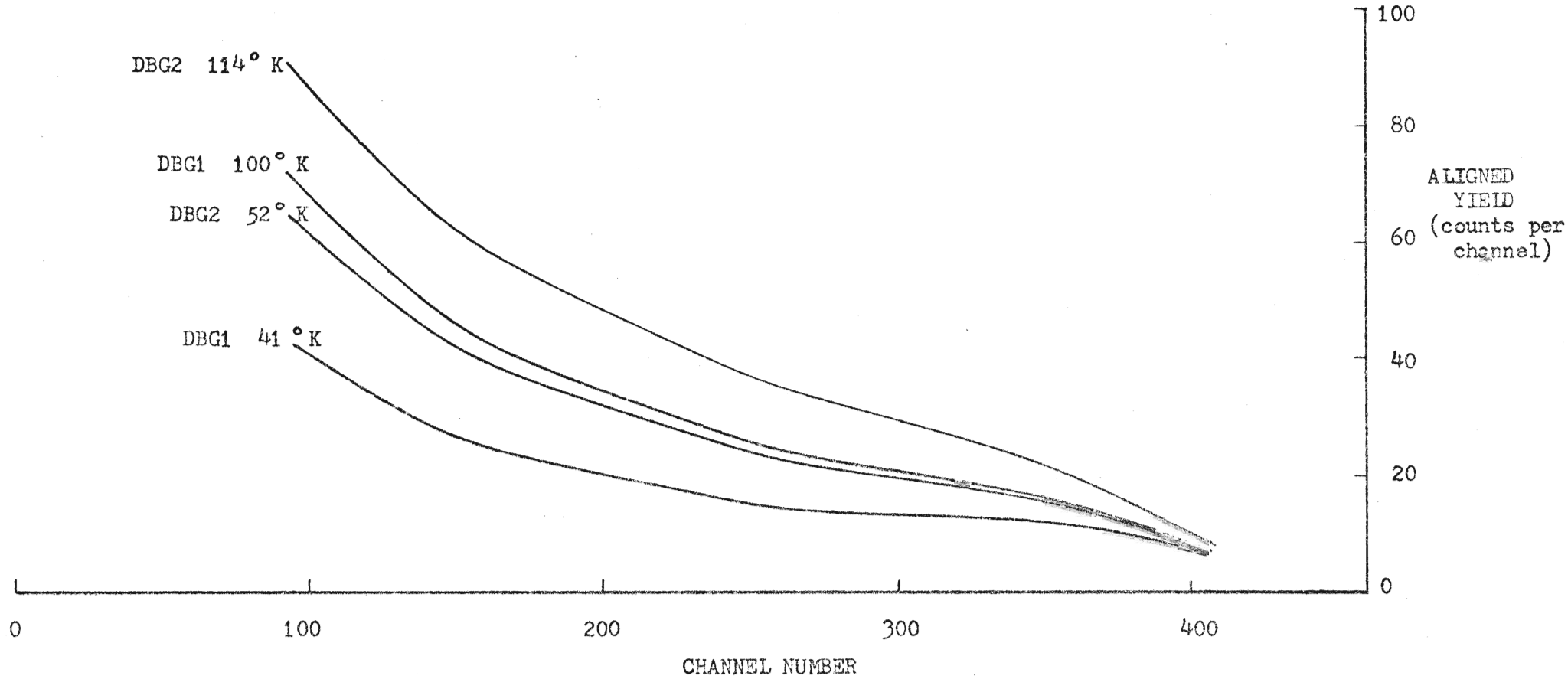

Figure V. 12. Surface Peak of Aligned Spectrum of DBG 1 as a function of Temperature. Only the 293° K and 41° K spectra are shown for clarity.

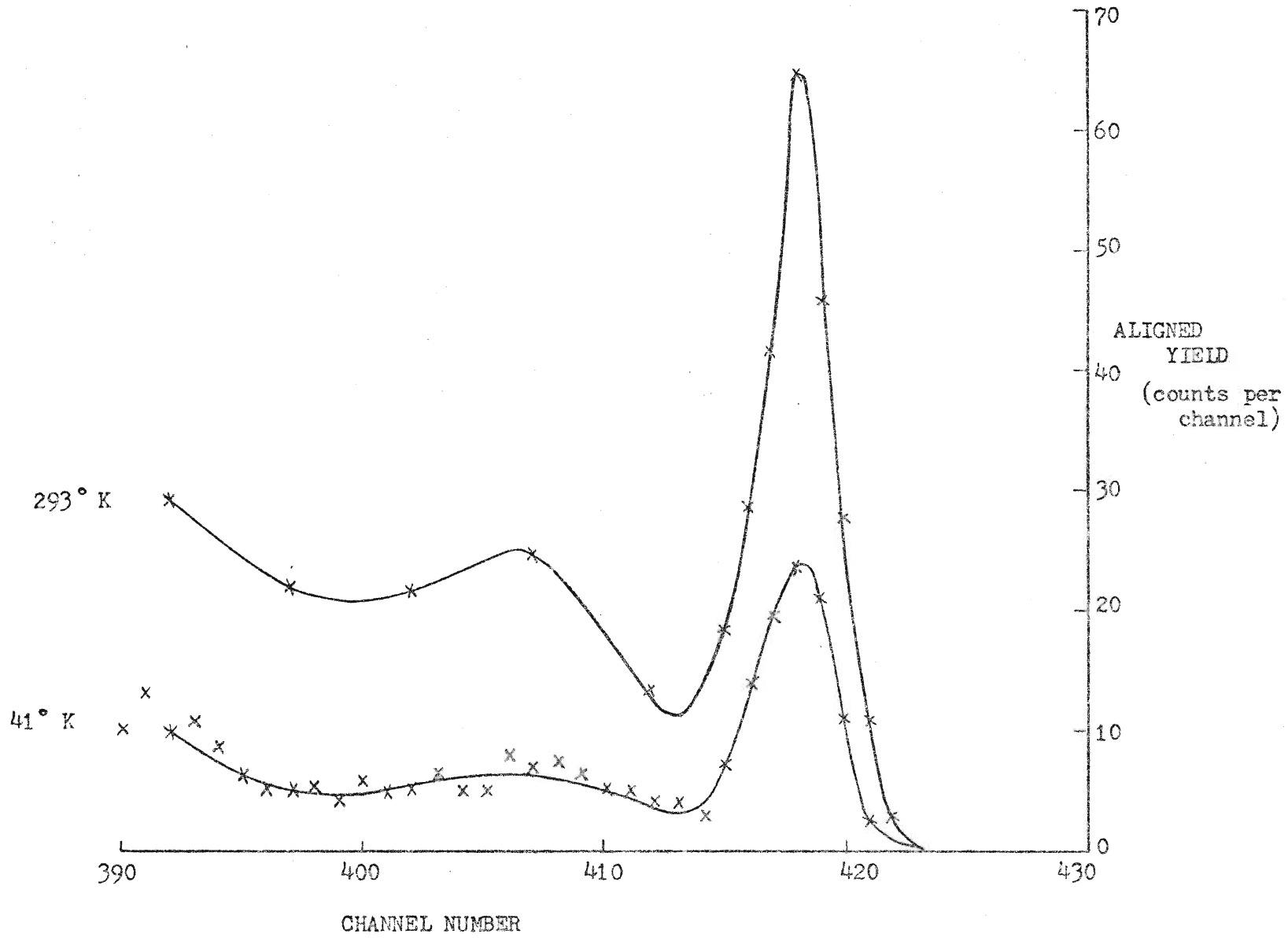

Figure V. 13. Surface Peak of Aligned Spectrum of DBG 2 as a function of Temperature. Only 293° K and 52° K spectra are shown for clarity.

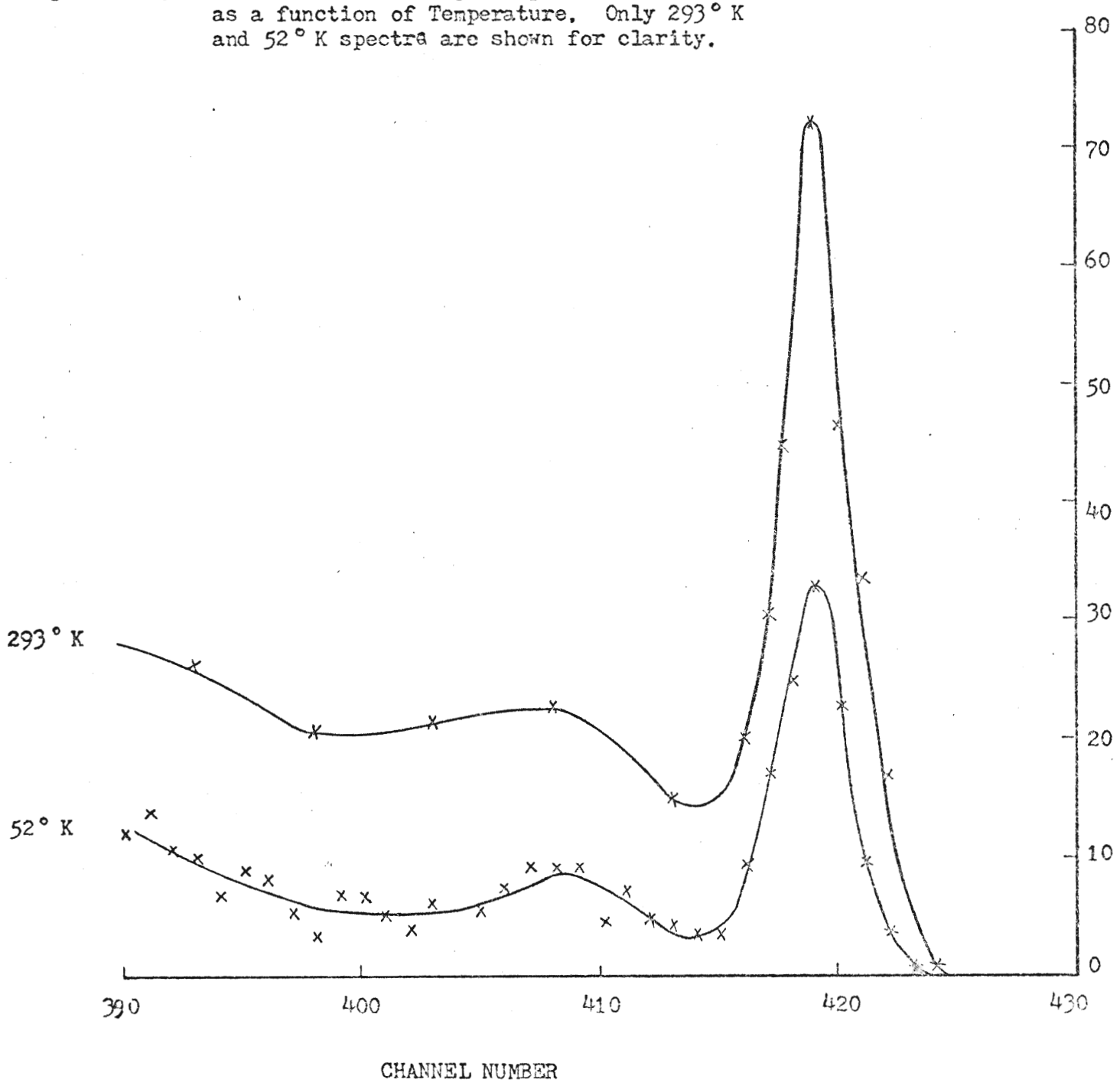

V.4 ANALYSIS OF DECHANNELING MEASUREMENTS

The beam energy was required to be constant throughout the measurements. Consequently, the energy (or channel number) of particles backscattered from the crystal surface, E_1, represented by the centre of the surface peak in the aligned spectra and the centre of the surface edge in random spectra, should be constant throughout the measurements. The channel number of particles backscattered from the crystal surface was found to be coincident, within ±2 channels (±8.5 keV), for all the 2 MeV He^+ spectra. The detector resolution was 10-15 keV, so the small beam energy variations were considered to be acceptable. The value of E_1 calculated from $E_1 = k^2E_0$, where E_0 is the nominal beam energy, 2 MeV, and that obtained from the aligned spectrum and the calibration of the M.C.A. differed by 17.0 ± 4.0 keV.

Figures V.14 and V.15 show random fraction versus depth spectra as a function of temperature. The energy-to-depth scale conversion and the calculation of random fraction from the aligned and random energy spectra (shown in Figures V.9 and V.10) were made using the methods outlined in Chapter Two. The stopping power data of Ziegler and Andersen[28] were used.

Table V.1 shows the surface peak yield, Y_{SA}, (normalised to an integrated beam monitor current of 0.1 μC) of the aligned spectra as a function of temperature and the corresponding effective number of surface scattering centres per unit area, n'dx', calculated from

$$n'dx' = \frac{Y_{SA}}{Y_{SR}} \cdot \frac{n\Delta E}{2S_0} \qquad \text{(see Chapter Two)},$$

Figure V. 14. Random Fraction versus Depth for DBG 1

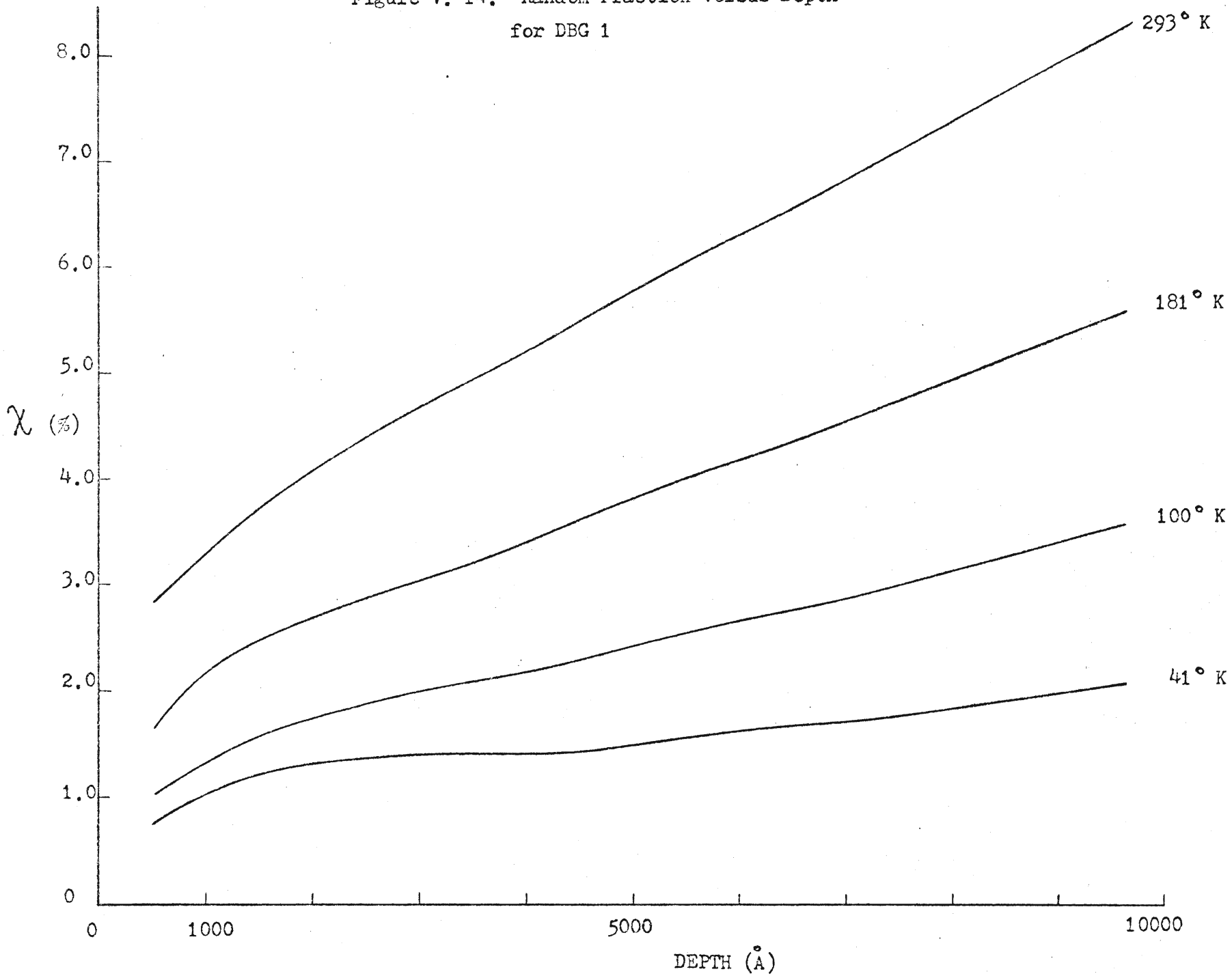

Figure V. 15. Random Fraction versus Depth for DBG 2

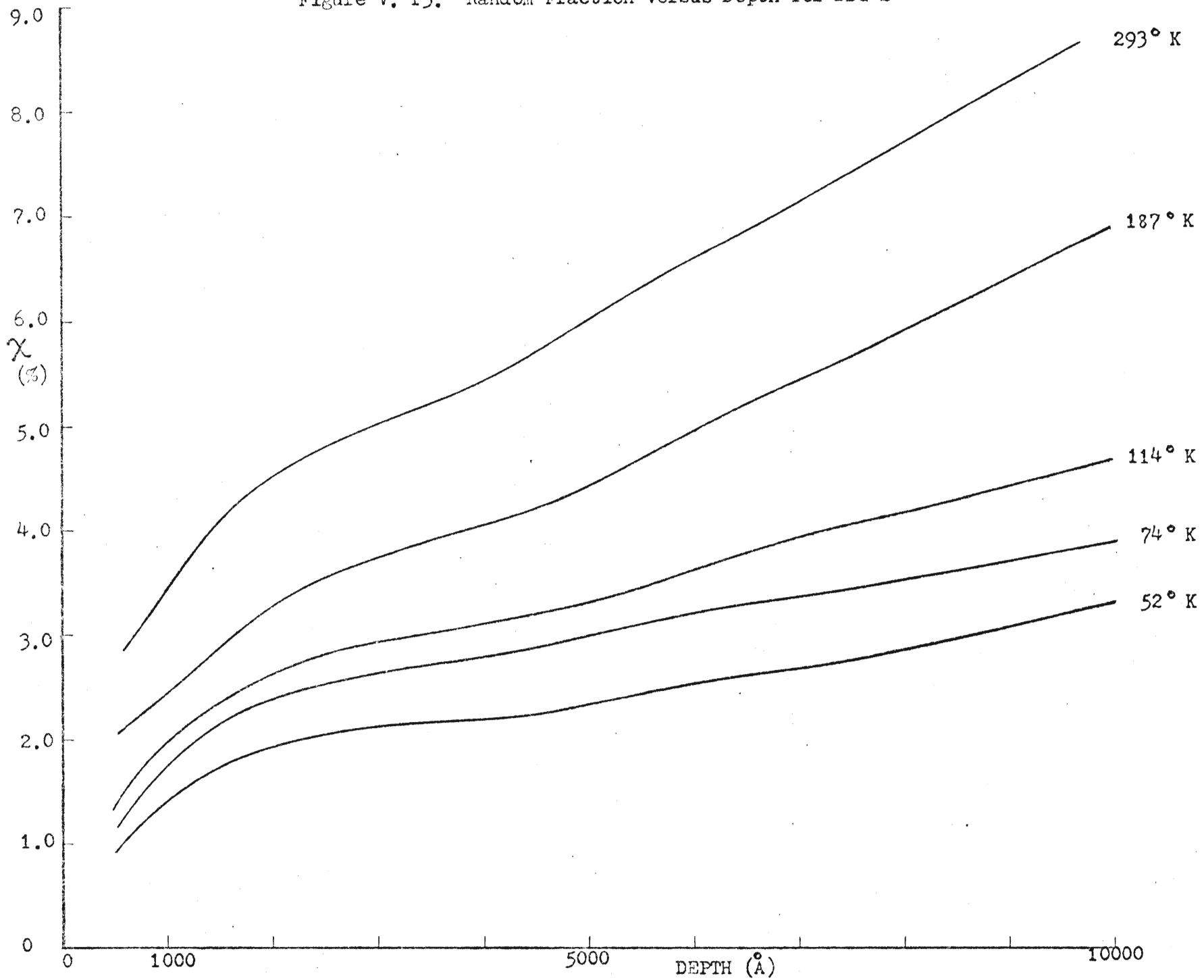

TABLE V.1

DBG1

Temperature	41°K	100°K	181°K	293°K
Y_{SA} (for 0.1 μC)	86 (±4%)	121 (±5%)	152 (±5%)	201 (±5%)
n'dx' (atoms/m^2)	$1.8(\pm0.2)\times10^{19}$	$2.5(\pm0.3)\times10^{19}$	$3.2(\pm0.4)\times10^{19}$	$4.2(\pm0.5)\times10^{19}$

DBG2

Temperature	293°K	52°K	114°K	187°K	293°K
Y_{SA} (for 0.1 μC)	233 (±7%)	107 (±4%)	135 (±5%)	163 (±5%)	200 (±4%)
n'dx' (atoms/m^2)	$5.6(\pm0.7)\times10^{19}$	$2.6(\pm0.3)\times10^{19}$	$3.3(\pm0.4)\times10^{19}$	$3.9(\pm0.4)\times10^{19}$	$4.8(\pm0.5)\times10^{19}$

where Y_{SR} = 887 ± 1% for DBG1 and 771 ± 1% for DBG2,

$n = 5.905 \times 10^{28}$ atoms/m^3,

ΔE = 4.27 keV/channel and

$S_0 = 115\ (\pm 5\%) \times 10^{-15}$ eV·cm^2/atom from Ziegler and Andersen[28].

The precisions given for Y_{SA} and Y_{SR} are determined by the statistical error on their total count values. Y_{SA} is found by extrapolating the aligned yield, through the surface peak to zero at the front edge of the surface peak and integrating the yield above the extrapolated curve, see Figure V.16.

Now $n'dx' = n_d dx_d + n_s dx_s$, where $n_s dx_s$ and $n_d dx_d$ are the contributions from the string atoms and the surface disordered atoms respectively. $n_d dx_d$ is independent of temperature, while $n_s dx_s$ is temperature-dependent. As the crystal temperature approaches 0°K, $n_s dx_s$ decreases to the string-end density, n d. Hence an upper limit for $n_d dx_d$ is obtained for each crystal by subtracting n d. ($\approx 1.7 \times 10^{19}$ atoms/m^2) from the lowest temperature value of n'dx'. This gives $n_d dx_d = 1.0\ (\pm 1.8) \times 10^{18}$ atoms/m^2 for DBG1 and $n_d dx_d = 8.8\ (\pm 2.6) \times 10^{18}$ atoms/m^2 for DBG2. The corresponding temperature dependent values which were calculated for $n_s dx_s$ are given in Table V.2.

To determine the measured value of χ_{min}, the aligned yield was averaged over the range of the surface oscillations (a depth range of approximately 280 Å to 1000 Å) and divided by the random yield just below the surface. This corresponds to the method used by Barrett[39].

Figure V. 16. The yield in the shaded triangle is subrtracted from the total yield in the surface peak to obtain Y_{SA}.

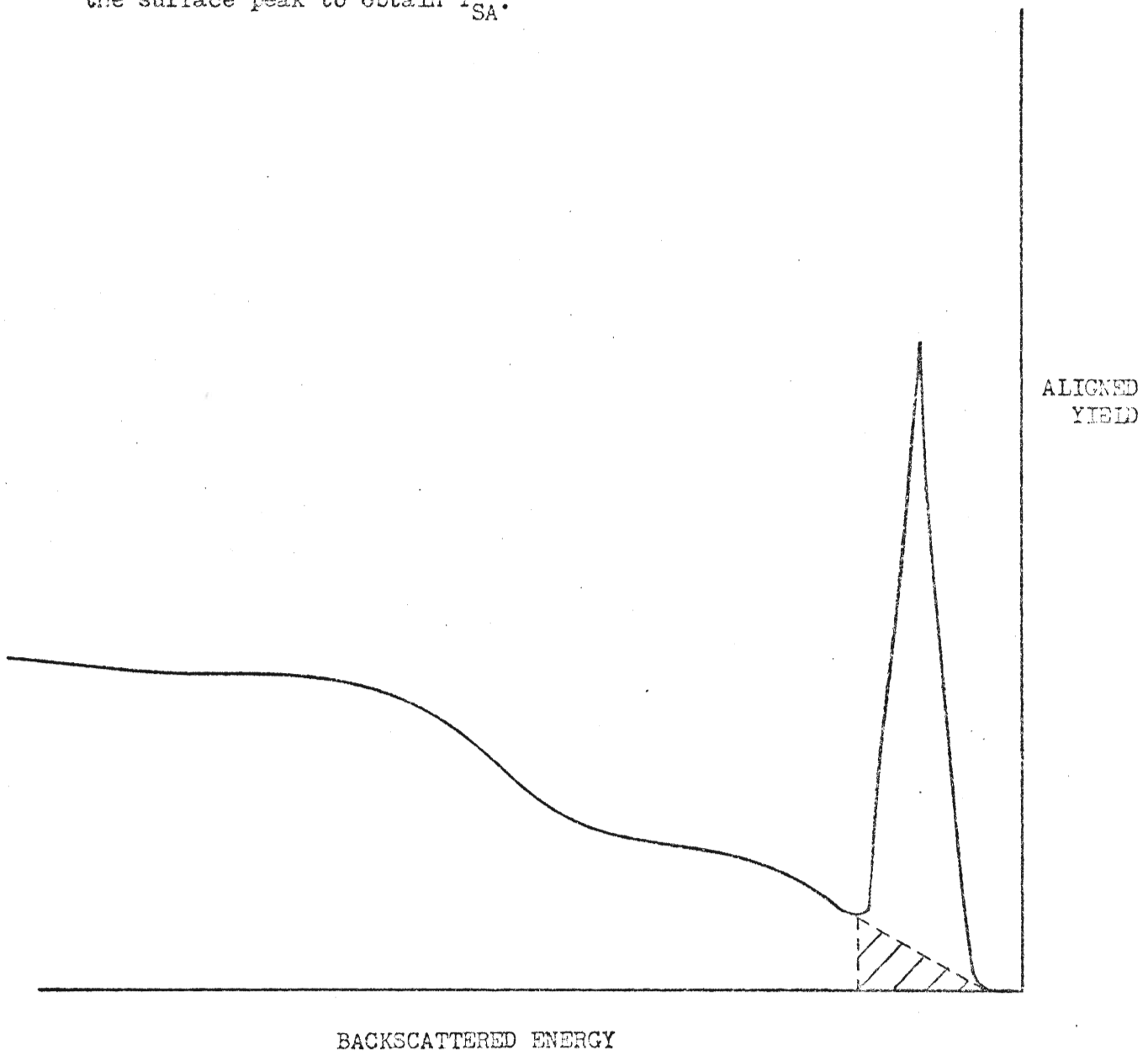

TABLE V.2

DBG1

Temperature	41°K	100°K	181°K	293°K
$n_s dx_s$ (atoms/m^2)	1.7×10^{19}	$2.4(\pm 0.3) \times 10^{19}$	$3.1(\pm 0.4) \times 10^{19}$	$4.1(\pm 0.5) \times 10^{19}$

DBG2

Temperature	293°K	52°K	114°K	187°K	293°K
$n_s dx_s$ (atoms/m^2)	$3.9(\pm 0.6) \times 10^{19}$	1.7×10^{19}	$2.4(\pm 0.4) \times 10^{19}$	$3.1(\pm 0.5) \times 10^{19}$	$4.7(\pm 0.8) \times 10^{19}$

The subsurface random yield for DBG1 was 887 ± 1% and for DBG was 771 ± 1%. The mean minimum aligned yields, normalised to an integrated beam monitor current of 0.1 μC, and the corresponding χ_{min} values are tabulated as a function of temperature in Table V.3. The statistical precisions are also shown.

V.5 COMPARISON OF EXPERIMENTAL RESULTS WITH THEORETICAL CALCULATIONS

The measured and calculated χ_{min} values are compared in Table V.4. The calculated values were obtained using both Lindhard's and Barrett's expressions, which are described in Chapter Two. The χ_3 values were calculated using the $n_d dx_d$ values shown in Section V.4. χ_3 was found to be 0.02% for DBG1 and 0.1% for DBG2.

The measured χ_{min} and the calculated values for χ_{min} (using Barrett's formula) are in excellent agreement for DBG1.

The Random Fraction versus Depth values as a function of temperature were calculated using the SITE approximation (see Chapter Three) and are compared with the spectra obtained for measurements on DBG1 in Figure V.17. The calculated dechanneling rate is approximately 40% of the experimental. The measured dechanneling rate shows a strong temperature dependence, increasing sixfold from 41°K to 293°K, which implies that there is only a small amount of dechanneling by defects.

TABLE V.3

DBG1

Temperature	41°K	100°K	181°K	293°K
$\langle Y_A \rangle$	6.8±3%	9.5±4%	14.5±3%	22.5±3%
χ_{min}	0.77(±0.03)%	1.07(±0.05)%	1.63(±0.07)%	2.53(±0.10)%

DBG2

Temperature	293°K	52°K	114°K	187°K	293°K
$\langle Y_A \rangle$	22.4±4%	7.3±3%	11.0±4%	15.7±3%	23.2±3%
χ_{min}	2.91(±0.15)%	0.94(±0.04)%	1.42(±0.06%)	2.04(±0.08)%	3.01(±0.10)%

TABLE V.4

DBG1

Temperature	41°K	100°K	181°K	293°K
χ_{min} (measured)	0.77(±0.03)%	1.07(±0.05)%	1.63(±0.07)%	2.53(±0.10)%
χ_{min} (Barrett)	0.53(±0.09)%	1.01(±0.12)%	1.63(±0.16)%	2.58(±0.22)%
χ_{min} (Lindhard)	0.7%	0.9%	1.1%	1.4%

DBG2

Temperature	293°K	52°K	114°K	187°K	293°K
χ_{min} (measured)	2.91(±0.15)%	0.94(±0.04)%	1.42(±0.06)%	2.04(±0.08)%	3.01(±0.10)%
χ_{min} (Barrett)	2.58(±0.22)%	0.64(±0.08)%	1.10(±0.12)%	1.69(±0.16)%	2.58(±0.22)%
χ_{min} (Lindhard)	1.5%	0.9%	1.0%	1.2%	1.5%

Figure V. 17. Random Fraction versus Depth
Comparison of Theory (- - -)
with Experimental (——).

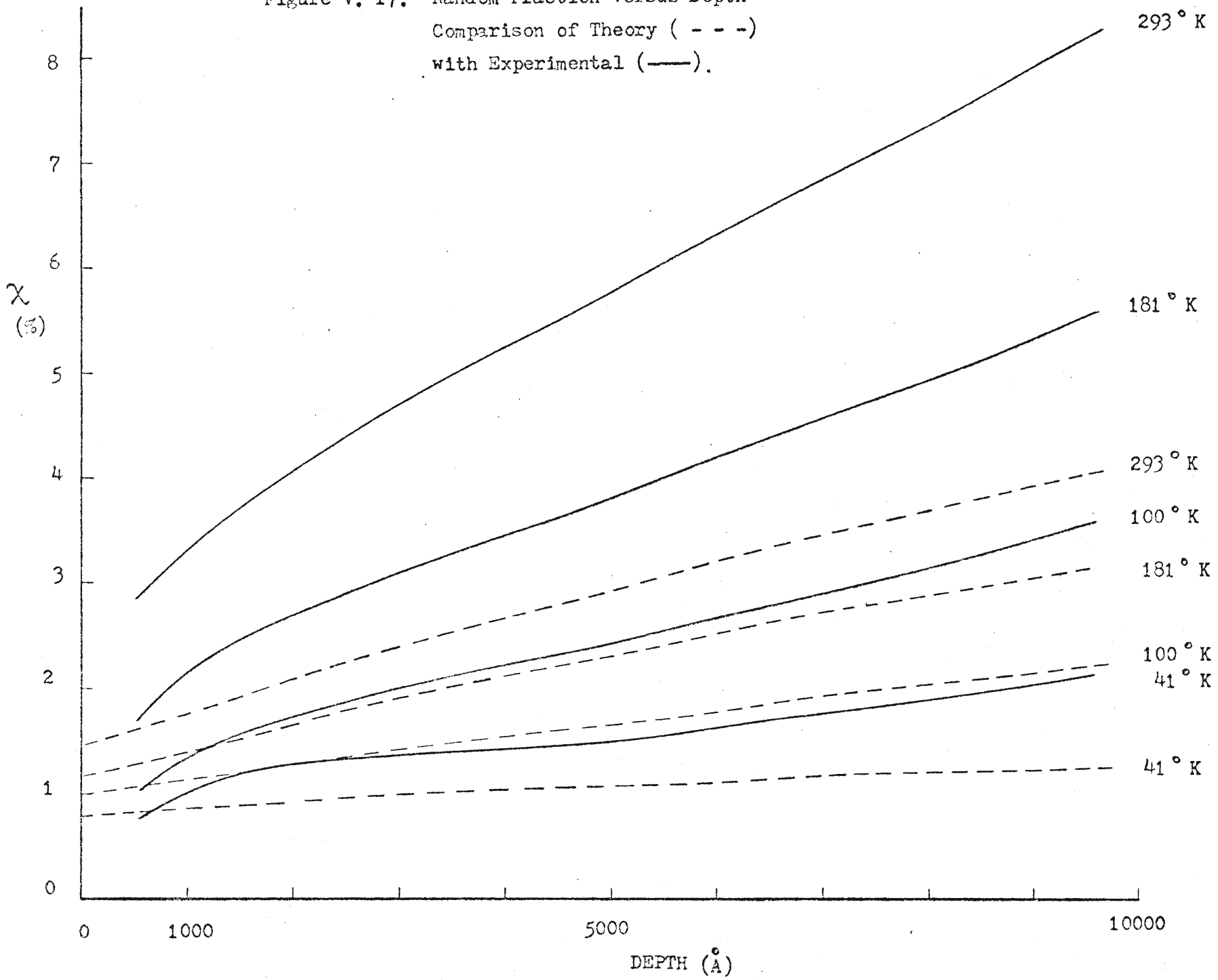

CHAPTER SIX

DISCUSSION AND CONCLUSION

VI.1 CRYSTAL QUALITY

The first aim in this project was to prepare well-ordered gold single crystals. The x-ray and electron diffraction photographs (see Chapter Four) indicated that the electropolishing and annealing treatment, which we adopted, effectively reduced the defect concentration in the bulk of the crystal and minimised the surface disorder. Table VI.1 shows the measured and calculated dechanneling rate as a function of temperature for DBG1 (see Figure V.17). The dechanneling rates were averaged over the depth interval ~2000 Å to 9500 Å. The calculated values are obtained using the SITE approximation (Chapter Three) with the critical distance of approach, r_c, given by $r_c^2 = 3\rho^2 + 0.2\ a^2$ (Barrett) or $r_c^2 = \rho^2 + a^2$ (Lindhard). The measured dechanneling rate at room temperature is 5.6 times that at 41°K. This large temperature dependence is in reasonable agreement with that calculated, namely, 5.0 (Lindhard) and 3.6 (Barrett). This strongly indicates that for room temperature, at least, the dechanneling is principally due to multiple scattering from thermally vibrating string atoms and that the contribution from defect scattering is very small, if not completely negligible. This view is supported by the fact that crystals which show small differences in dechanneling rates at low temperatures (Figure V.11), presumably due to residual defects, show agreement at room temperature (Figure V.8).

TABLE VI.1

Temperature	Dechanneling Rates		
	Measured (DBG1)	Calculated (Lindhard)	Calculated (Barrett)
41°K	0.107 (%/1000 Å)	0.0515	0.0579
100°K	0.222	0.115	0.110
181°K	0.406	0.179	0.159
293°K	0.599	0.259	0.210

If the number of scattering centres per unit area in the disordered layer, $n_d dx_d$, is assumed to be uniformly distributed on the crystal surface, then the value obtained in Section V.4 for DBG1 ($1.0 \pm 1.8 \times 10^{18}$ atoms/m^2) shows that there is significantly less than one monolayer of disorder (1.7×10^{19} atoms/m^2) on the crystal.

The measured and calculated (Barrett) values of χ_{min} for DBG1 are, overall, in excellent agreement (see Table V.4). We note here that the (Lindhard) calculated χ_{min} values were intended by Lindhard to be only estimates.

The observed strong temperature dependence of the dechanneling rate, the measured surface disorder of less than one monolayer and the agreement of the measured χ_{min} values with those calculated for perfectly ordered surfaces all lead to the conclusion that the gold crystals are indeed of high quality and exhibit dechanneling characteristic of defect-free crystals.

VI.2 EXPERIMENTAL RANDOM FRACTION SPECTRA

In principle the extraction of the Random Fraction versus Depth spectrum from the Aligned and Random (Energy) spectra is quite simple (see Chapter Two). However, several possible complicating factors must be remembered. There is a unique relationship between backscattered energy and depth, via stopping power, in the case of the random spectrum if single Rutherford scattering is assumed. But a channeled particle does not necessarily move through the same average electron density as a particle in the random beam and hence does not necessarily experience the same rate of energy loss. Consequently the depth scales for the random and aligned spectra may be somewhat different[10]. The stopping power for a channeled particle is difficult to characterise and measure. Nevertheless, we have found that the detected energy of particles backscattered from the rear surface of gold single crystal films (~6000 Å thick) for aligned incidence was only ~7% higher than that for random incidence. This implies that the channeled and random stopping powers are comparable for shallow depths. Our thin crystals were of rather poor quality as evidenced by high χ_{min} (10-15%) and dechanneling rate values at room temperature. However, the same observation has been reported by Merkle et al.[25] using good quality films. Therefore, we feel that the use of the same depth scale for the aligned and random spectra is justified.

In our analysis of the shape of the random spectrum (see Chapter Two), we used Ziegler and Andersen's empirical stopping power data and neglected events arising from more than one large angle scattering. Since the measured and random spectra were in good agreement, the assumption of single Rutherford backscattering being the predominant scattering mechanism and the use of Ziegler and Andersen's stopping power data would appear to be validated.

Thus, we feel that our calculation of the depth scale and the determination of the random fraction from the ratio of the aligned and random spectra is good to within the precision limitation imposed by the beam monitor and the observed thin film tails, namely 5-10%.

VI.3 CALCULATED RANDOM FRACTION SPECTRA

The Aarhus group found that calculations made taking into account diffusion in transverse energy and those using the SITE approximation were in agreement at shallow depths (Figure I.2(a)). Nevertheless, they felt that the use of the SITE approximation did not seem reasonable on physical grounds, since diffusion in transverse energy was evident in their calculations[15].

Both diffusion and SITE approximation calculations are made using the assumption that the initial transverse energy distribution and the critical transverse energy are well-defined and known. The theories differ in the calculation of changes in transverse energy distribution with depth.

In our SITE calculations, we assumed that the initial transverse energy distribution was completely described by a potential energy distribution, $p(E_{\perp_0})$. This is valid if we are comparing with an experimental case where the beam is precisely aligned with the channel axis, the beam divergence is negligible and scattering by the disordered surface atoms is minimal. Precise alignment ($<0.1°$) was attained, as described in Chapter Five, and the beam divergence, defined geometrically by the beam line apertures, was approximately 3×10^{-2} degrees. Neglecting any spread of the beam due to scattering in the beam line, the corresponding transverse kinetic energy distribution range due to beam misalignment and divergence is ± 10 eV, which is

negligible. An expression for the initial transverse kinetic energy distribution, $G(E_{\perp_o})$, produced by single Rutherford scattering from the disordered surface atoms is given by Björkqvist *et al.*[16],

$$G(E_{\perp_o}) = n_d dx_d \cdot \pi \cdot \left(\frac{e^2}{4\pi\epsilon_o}\right)^2 \cdot \frac{Z_1^2 \cdot Z_2^2}{E_{\perp_o}^2 E}$$

$G(E_{\perp_o})$ is tabulated with $p(E_{\perp_o})$ in Table VI.2 for the initial transverse energy range of particles dechanneled within 10,000 Å. $G(E_{\perp_o})$ is calculated using the value of $n_d dx_d$ appropriate for DBG1 (1.0×10^{18} atoms/m^2). Table VI.2 shows that the contribution to the distribution in initial transverse energy caused by scattering in the surface disorder layer, $G(E_{\perp_o})$, is approximately two orders of magnitude less than $p(E_{\perp_o})$ and hence can be neglected. Therefore, we feel that the use of $p(E_{\perp_o})$ for the initial transverse energy distribution is justified in our case.

TABLE VI.2

$E_{\perp_o}$ (eV)	$p(E_{\perp_o})$ (eV^{-1})	$G(E_{\perp_o})$ (eV^{-1})
250	1.98×10^{-4}	1.32×10^{-6}
500	5.09×10^{-5}	3.29×10^{-7}
640	3.07×10^{-5}	2.01×10^{-7}
750	2.21×10^{-5}	1.47×10^{-7}
1000	1.20×10^{-5}	0.82×10^{-7}

We have used the values suggested by Lindhard[14] for the critical transverse energy (*i.e.*, $E_{\perp_c} = U(r_c)$, where $r_c^2 = \rho^2 + a^2$) and for the potential screening parameter, C ($C = \sqrt{3}$). Lindhard notes that these values are to be regarded as estimates. We have therefore investigated the effect on the calculated Random Fraction spectra of variations in

the values of C and $E_{\perp c}$ (see Figures VI.1 and VI.2, respectively). In the case of $E_{\perp c}$, we altered the magnitude of $E_{\perp c}$ but left its temperature dependence unchanged (i.e., $E_{\perp c} = \alpha \cdot U(r_c)$, where $0.1 \leq \alpha \leq 2.0$). In another attempt we used $r_c^2 = 3\rho^2 + 0.2\ a^2$, which gives agreement at the surface and is consistent with the results of Barrett's Monte Carlo χ_{min} calculations. However, the calculated dechanneling rate appears to be relatively insensitive to the value of these parameters, C and $E_{\perp c}$ (Figures VI.1 and VI.2). Therefore, we conclude that there is a real difference between the measured dechanneling rate and that calculated using the SITE approximation.

For Random Fraction values up to 10%, the values calculated using the SITE approximation by the Aarhus group[15] for 1.6 MeV protons on ⟨110⟩ silicon and 2.0 MeV protons on ⟨100⟩ tungsten and those reported by Foti et al.[18] for 1.5 MeV protons on ⟨111⟩ silicon showed similar disagreement from the measured values to those we observed for 2 MeV He^+ in ⟨110⟩ gold.

In the SITE approximation, statistical equilibrium is assumed[14], i.e., particles of the same transverse energy uniformly populate their accessible area in transverse space. Barrett[40], using Monte Carlo calculations to study the causes of the sub-surface peaks in the aligned spectra, has shown that channeled particles experience a focussing effect on entering the crystal surface. He suggests that this focussing effect constitutes a breakdown in statistical equilibrium and affects the yield even beyond the near-surface region. Therefore, a basic assumption (statistical equilibrium) may not be completely valid in the surface region (<1 micron) and this may be a contributing cause to the observed difference between measured and calculated dechanneling rate.

Figure VI.1 Random Fraction versus Depth at Room Temperature. Experimental (——) and Calculated (---). The screening constant "C" is a parameter.

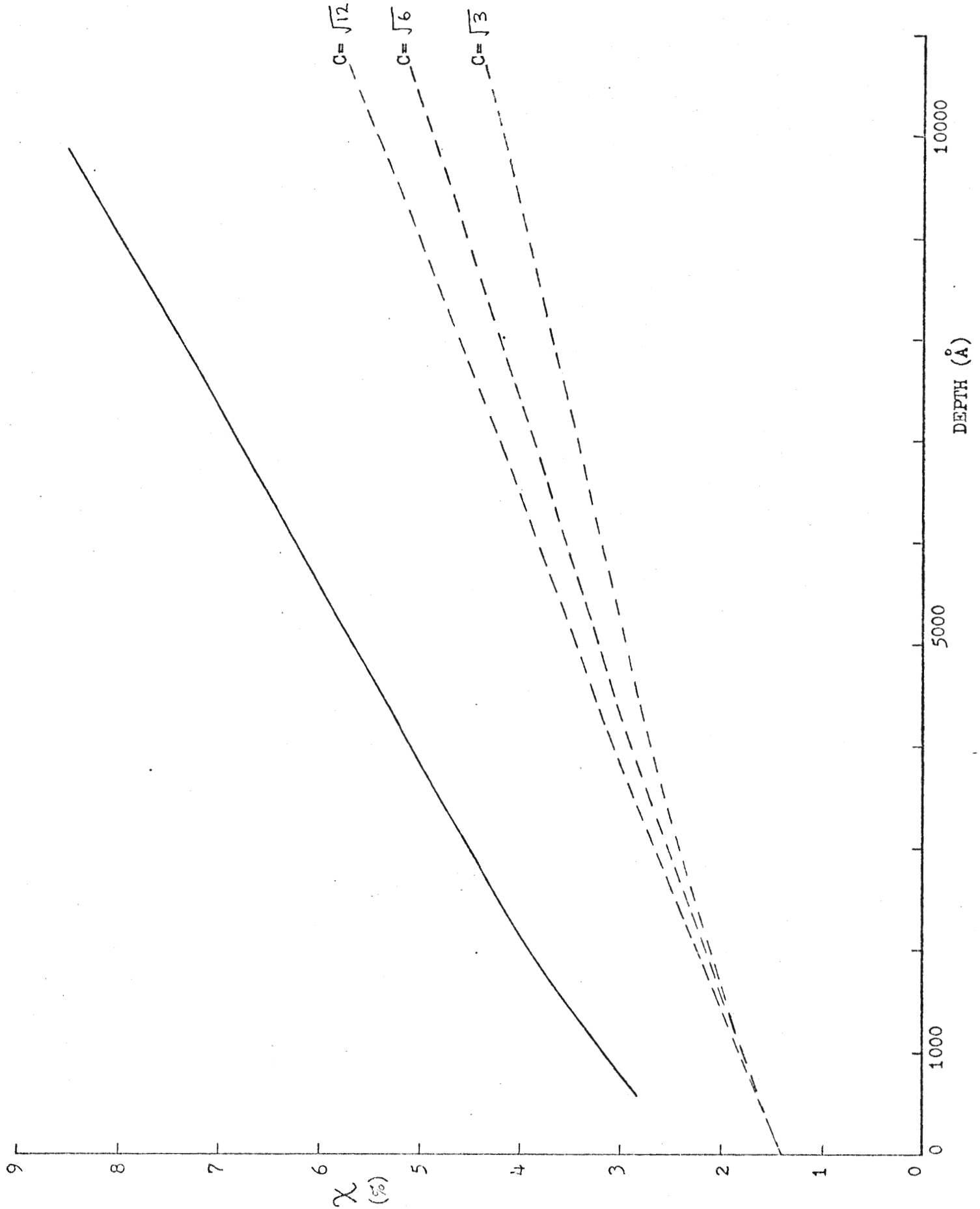

Figure VI. 2

Calculated Random Fraction Spectra Using $E_{\perp c}$ as a Parameter.
(a) $E_{\perp c}=0.5\ U(r_c)$, (b) $E_{\perp c}=U(r_c')$, $r_c'^2=3\rho^2+0.2a^2$,
(c) $E_{\perp c}=U(r_c)$, (d) $E_{\perp c}=2U(r_c)$.

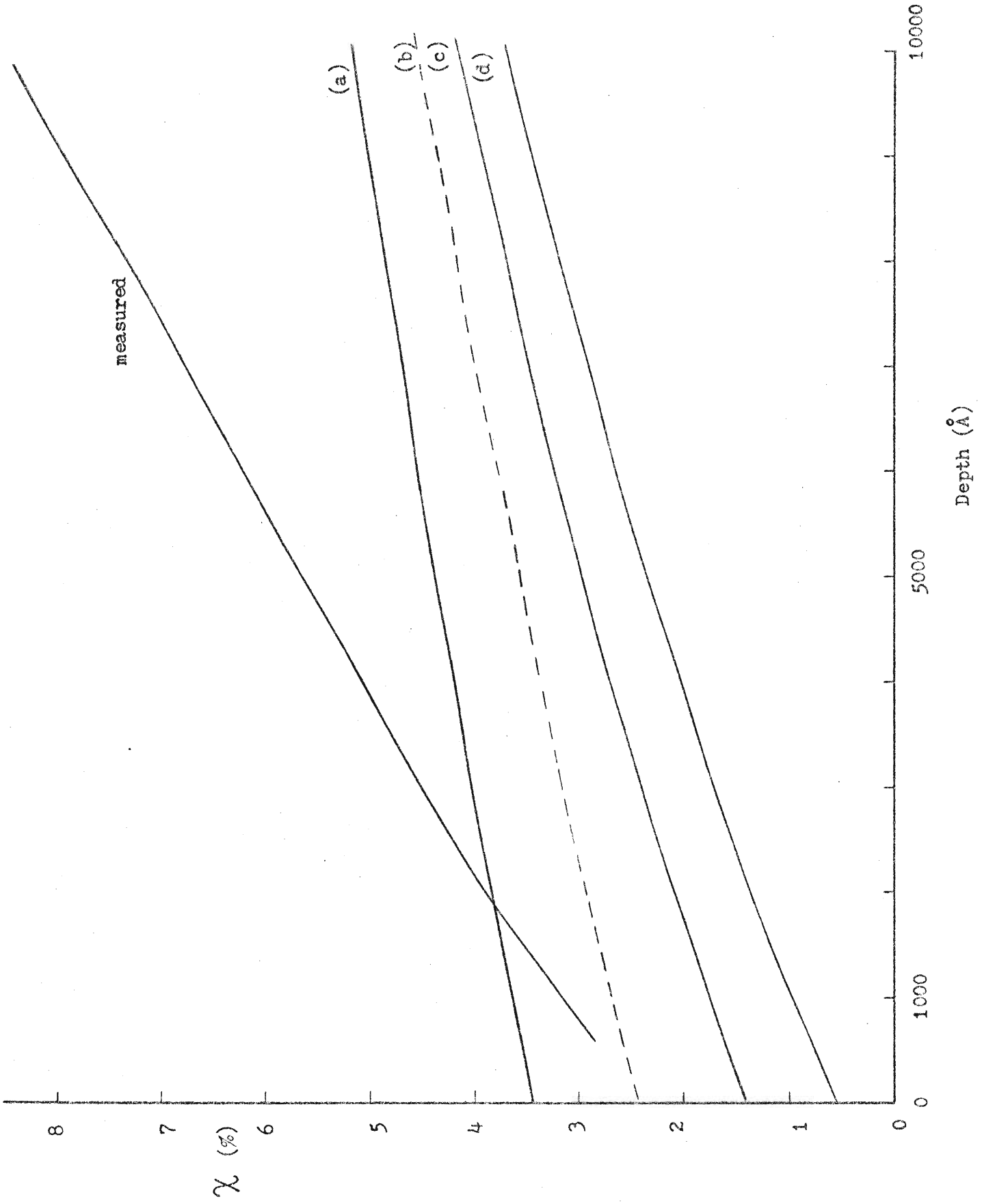

VI.4 CONCLUSION

The electropolishing and annealing treatments used in this project were effective in preparing high quality defect-free gold single crystals.

The measured Random Fraction spectra have been shown to represent dechanneling of 2 MeV He^+ in well-ordered <110> gold.

The calculated dechanneling rates based on the SITE approximation are 40-50% of those measured, although they show approximately the same temperature dependence. The differences are not considered to be due to the use of incorrect values for the theoretical parameters but may be due to lack of statistical equilibrium in the transverse motion in the surface region.

APPENDIX A

THE CONTINUUM POTENTIAL, U(r)

$V(\rho_n)$ is the interatomic potential between particle P and any string atom, n (see Figure A.1).

$\sum_n V_n(\rho_n)$ is the <u>total</u> potential experienced by P and is <u>periodic</u> along z. By definition U(r) is the average of $\sum_n V(\rho_n)$ along z. Since $\sum_n V(\rho_n)$ is periodic, then U(r) is the average of $\sum_n V(\rho_n)$ between $z = \pm d/2$).

Now the contribution of the string atom n to U(r) as P is moved between $z = \pm d/2$ is given by:

$$U_n = 1/d \int_{-d/2}^{+d/2} V(\rho_n).dz,$$

where $\rho_n^2 = (nd - z)^2 + r^2$.

By changing the variable from z to z', where z' = nd - z, we may write:

$$U_n = 1/d \int_{d(n+1/2)}^{d(n-1/2)} V(\rho').dz'$$

where $\rho'^2 = z'^2 + r^2$.

Therefore, $U(r) = \sum_n U_n$

$$= 1/d \int_{-\infty}^{+\infty} V(\rho).dz.$$

Figure A. 1.

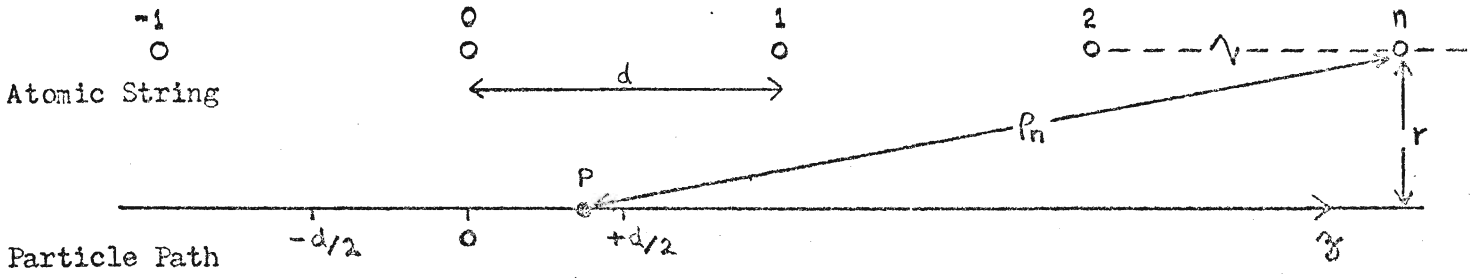

APPENDIX B

THE APPROXIMATE ALIGNMENT OF A CHANNEL AXIS WITH THE BEAM DIRECTION

By indexing the spots in the spots in the Laue x-ray diffraction pattern, we had ascertained the approximate angle, ϕ°_{a}, that the $\langle 110 \rangle$ direction in a crystal made with the normal to the crystal surface. With the crystal fastened to the goniometer head and the goniometer setting at $(0^{\circ},0^{\circ})$, then the azimuthal axis is coincident with the beam direction, see Figure B.1. The crystal is then tilted through an angle ϕ°, where $\phi^{\circ} > \phi^{\circ}_{a}$, and rotated around the azimuthal axis (Figure B.2). During the azimuthal rotation the beam passes through a set of directions in the crystal, lying on the perimeter of the base of the cone traced out during rotation (Figure B.3). A direction in the crystal can therefore be identified with the azimuthal and tilt coordinates, $(\phi^{\circ},\theta^{\circ})$, of its projection on to the base of the cone. The Ratiometer reading is monitored during the azimuthal rotation and the dips in the reading recorded as a function of the azimuthal angle, θ° (see Figure B.4). A dip occurs whenever the beam direction is incident along a plane containing the $\langle 110 \rangle$ direction. Since the intersection of planes containing the $\langle 110 \rangle$ direction is the $\langle 110 \rangle$ axis itself, then the intersection of the projected planes will give the coordinates $(\phi'^{\circ},\theta'^{\circ})$ of the projected $\langle 110 \rangle$ direction (see Figure B.5). By rotating the goniometer to $(\phi'^{\circ},\theta'^{\circ})$, the beam direction is now coincident with the $\langle 110 \rangle$ direction. This alignment is approximate, since the azimuthal dip is often quite wide (see Figure V.6).

Figure B. 1.

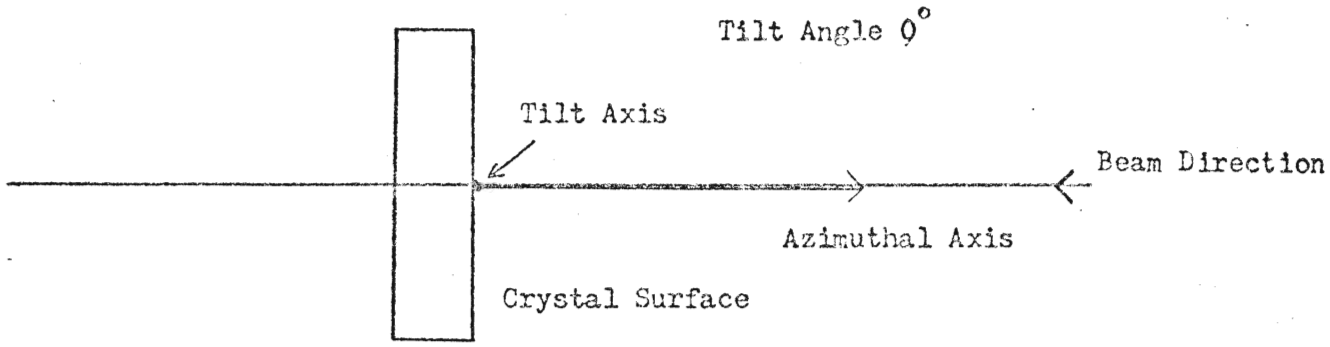

Figure B. 2.

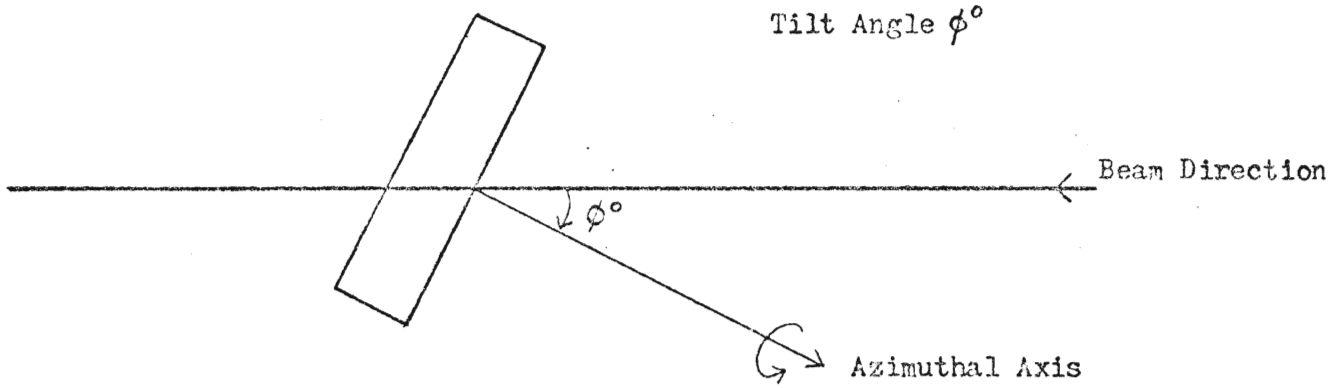

Figure B. 3.

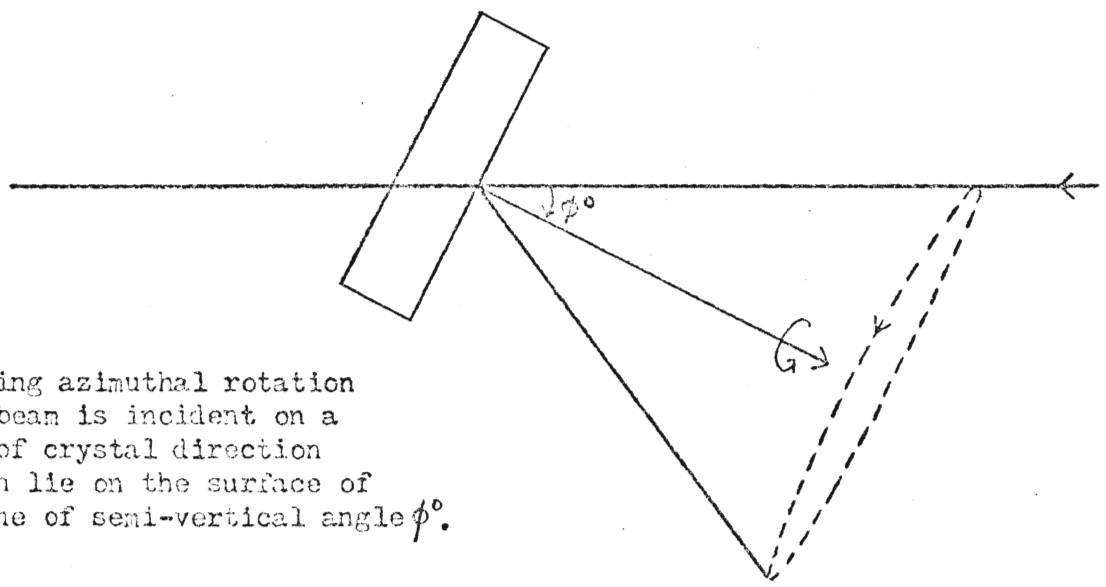

During azimuthal rotation the beam is incident on a set of crystal direction which lie on the surface of a cone of semi-vertical angle $\phi°$.

Figure B. 4.

The projection of the crystal directions traced out by the beam, during azimuthal rotation, lie on a circle in a plane normal to the azimuthal axis.

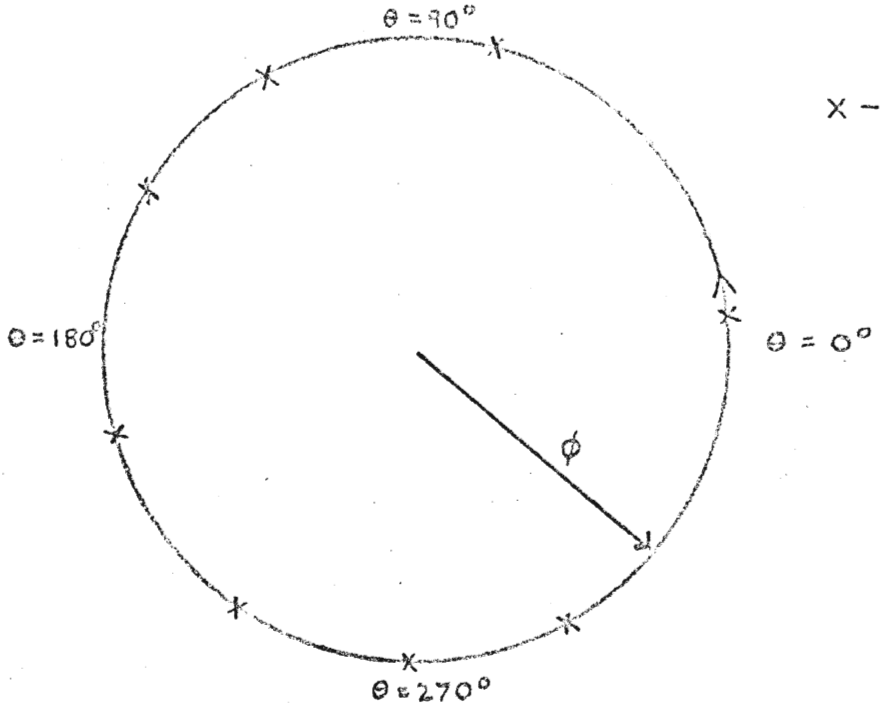

Figure B. 5.

The ratiometer dips are used to locate the projections of the crystallographic planes containing the ⟨110⟩ direction. Their intersection gives the coordinates (ϕ', θ') of the projection of the ⟨110⟩ axis.

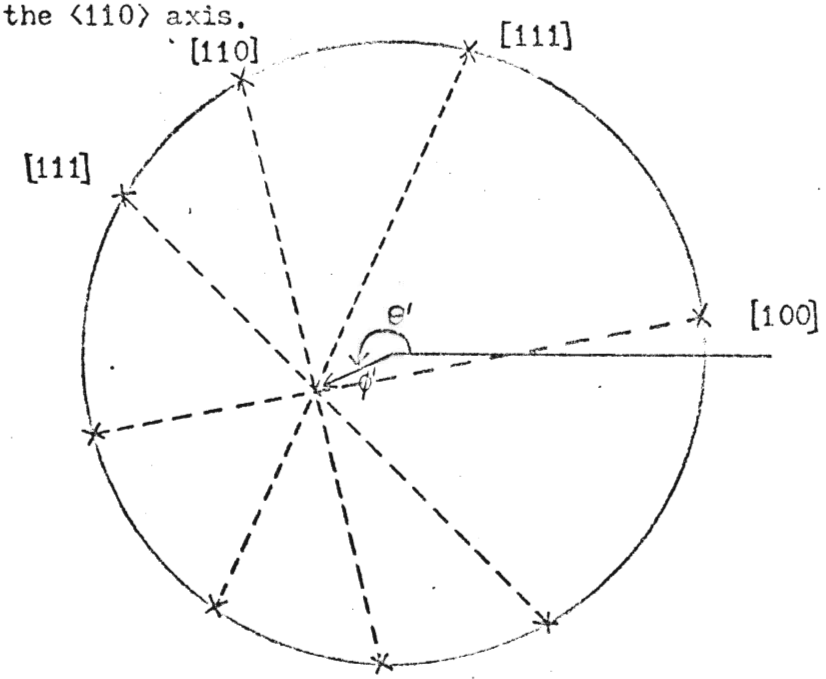

APPENDIX C

M. C. A. DATA

The following pages give the raw M. C. A. data in the aligned and random (energy) spectra for crystals DBG1 and DBG2. The heading gives the crystal name, type of spectrum, crystal temperature and integrated beam current, respectively.

The data is collected in the form: counts per channel versus channel number. The first column (from the left hand side) gives the channel numbers of the yields in the second column. The channel numbers increase from left to right across the remaining rows of yields.

The channel number scale can be converted to a backscattered energy scale, using the M. C. A. calibration:

E_1(keV) = 4.27 x channel number + 40.60

DEG1 Aligned Spectrum 41°K, 0.6 μC

38	570	550	483	564	507	489	466	510
46	464	467	462	487	436	472	393	424
54	443	394	431	387	387	364	385	382
62	394	380	344	366	383	342	365	342
70	368	313	306	319	330	320	288	301
78	311	296	319	288	295	276	268	285
86	289	301	263	276	272	253	270	256
94	263	257	262	244	254	246	228	262
102	257	222	226	272	239	238	247	240
110	214	255	244	224	206	214	189	226
118	200	220	203	204	218	214	203	217
126	215	202	226	189	195	209	191	200
134	175	183	203	174	201	174	182	173
142	167	182	173	153	165	179	149	163
150	155	183	166	186	167	177	149	152
158	166	150	170	159	164	173	151	156
166	155	160	165	150	168	164	175	134
174	137	143	122	154	144	143	124	150
182	145	143	133	137	127	147	139	122
190	100	116	115	136	115	124	108	124
198	146	116	130	121	108	127	115	124
206	139	109	121	129	120	105	129	111
214	131	125	117	147	103	113	105	123
222	102	90	104	120	113	106	121	112
230	116	112	106	130	117	91	117	105
238	105	113	95	110	104	90	92	97
246	120	93	79	69	76	76	91	59
254	79	69	72	102	101	97	119	94
262	104	101	77	88	72	73	77	87
270	99	86	90	94	93	76	101	99
278	81	82	82	76	78	86	100	94
286	77	77	82	90	69	59	89	77
294	96	84	97	98	71	94	95	81
302	71	78	72	74	87	82	71	74
310	83	71	71	69	58	77	75	85
318	51	71	64	92	70	69	74	81
326	68	68	57	72	50	70	67	93
334	68	85	70	89	69	65	62	59
342	54	69	64	77	67	60	60	52
350	61	67	63	62	59	61	53	69
358	67	63	57	59	70	73	51	61
366	52	62	49	58	52	83	61	57
374	47	55	51	55	80	69	75	52
382	58	60	49	54	52	72	46	64
390	62	80	59	65	52	38	32	30
398	33	26	36	30	32	39	30	30
406	48	42	46	39	34	30	23	24
414	20	42	85	117	141	125	68	15
422	5	1	0	0	0	0	0	0
430	0	0	0	0	0	0	0	0
438	0	0	0	0	0	0	0	0
446	0	0	0	0	0	0	0	0
454	0	0	0	0	0			

DBG1 Aligned Spectrum 100°K, 0.3 μC

38	503	430	486	446	472	407	392	391
46	393	395	370	387	399	351	355	362
54	375	322	340	343	341	330	315	316
62	322	274	308	306	275	280	303	273
70	288	297	271	277	263	264	286	310
78	272	246	255	240	227	223	236	243
86	223	250	253	216	197	242	246	219
94	214	210	239	208	206	201	207	219
102	222	218	187	216	183	181	159	208
110	209	198	200	176	173	193	170	168
118	168	148	180	168	174	176	159	167
126	174	162	168	160	156	149	151	164
134	156	164	184	134	148	144	158	139
142	181	140	145	153	155	137	145	126
150	136	131	145	115	125	117	132	122
158	127	141	149	139	136	133	122	109
166	123	120	136	113	127	137	112	125
174	120	113	118	116	107	118	106	94
182	125	109	112	128	106	100	101	112
190	92	90	104	109	115	107	116	109
198	102	106	100	110	91	84	106	102
206	92	115	98	104	108	83	95	106
214	106	89	90	78	87	94	87	81
222	102	102	84	91	85	89	93	96
230	87	88	94	94	74	73	79	104
238	101	90	91	83	85	85	77	74
246	73	79	83	62	53	64	81	51
254	70	68	74	75	71	80	75	73
262	81	80	81	70	76	68	65	82
270	70	70	84	71	59	71	66	70
278	59	76	80	51	65	55	67	69
286	76	68	70	53	62	59	65	64
294	63	61	57	52	68	53	67	68
302	76	52	66	55	60	70	61	59
310	48	74	61	63	65	52	64	63
318	71	53	51	52	54	47	55	59
326	72	46	51	54	51	56	60	44
334	45	57	59	47	53	49	59	49
342	46	47	48	51	50	50	48	55
350	59	42	54	57	52	47	58	37
358	48	49	51	42	41	47	51	43
366	50	46	53	50	48	40	48	38
374	44	41	42	52	47	44	47	31
382	34	36	38	41	36	30	49	32
390	46	54	61	40	34	31	20	28
398	28	26	22	17	23	22	19	25
406	19	24	33	29	16	19	20	9
414	19	29	36	64	104	114	50	19
422	1	0	0	0	0	0	0	0
430	0	0	0	0	0	1	0	0
438	0	0	0	0	0	0	0	0
446	0	0	0					

DBG1 Aligned Spectrum, 181°K, 0.3 μC

34	773	774	742	740	731	760	680	682
42	686	621	640	690	652	645	635	611
50	581	546	554	572	528	534	547	550
58	521	507	497	509	503	443	472	500
66	488	462	513	492	442	444	458	471
74	425	398	439	414	369	409	383	408
82	372	366	388	381	365	378	363	356
90	337	340	342	367	340	357	360	318
98	339	325	327	321	323	315	335	320
106	299	337	313	314	309	302	296	315
114	299	282	288	273	279	285	282	282
122	307	266	262	258	293	305	262	263
130	232	256	261	264	248	283	237	231
138	245	236	243	276	250	235	269	227
146	214	228	241	231	225	211	229	217
154	209	218	200	209	208	198	205	196
162	200	185	185	190	205	206	163	204
170	204	206	188	198	195	177	174	164
178	180	167	168	204	170	182	190	155
186	202	181	176	160	167	179	165	170
194	167	164	184	172	180	170	174	155
202	166	150	161	166	152	187	152	182
210	123	145	167	155	145	127	144	151
218	179	132	152	154	138	136	151	130
226	141	136	132	141	152	146	129	161
234	129	140	150	158	151	130	121	130
242	142	131	136	142	124	99	113	131
250	102	103	107	131	120	135	110	96
258	116	117	136	105	119	119	128	114
266	98	117	124	117	115	100	116	105
274	116	90	106	115	95	72	97	113
282	108	124	96	82	112	115	107	118
290	100	102	101	90	102	94	85	106
298	75	96	101	87	87	100	89	89
306	86	87	89	93	91	93	90	83
314	83	96	90	92	79	80	88	85
322	74	79	89	94	73	88	70	83
330	71	75	77	77	74	82	66	70
338	78	89	73	89	70	61	78	86
346	54	88	74	76	81	87	63	66
354	80	61	69	63	75	70	78	62
362	60	64	71	88	82	80	66	58
370	52	58	72	71	77	60	62	70
378	63	68	59	52	62	52	58	59
386	64	70	54	56	60	53	76	70
394	40	53	37	46	35	52	39	38
402	31	44	39	42	40	46	50	36
410	33	27	18	23	33	26	54	97
418	123	122	76	23	4	2	0	0
426	0	0	0	0	0	0	0	0
434	0	0	0	0	0	0	0	0
442	1	0	0					

DBG1 Aligned Spectrum, 293°K, 0.3 μC

34	1130	1151	1142	1124	1043	1098	1037	1007
42	1088	1079	959	944	971	967	917	881
50	905	843	864	826	802	827	784	843
58	755	787	741	731	769	709	719	759
66	727	714	722	733	689	665	688	662
74	647	662	612	654	624	599	607	657
82	646	636	573	632	583	543	570	553
90	576	544	564	529	512	510	509	514
98	496	477	504	477	505	510	474	490
106	488	504	412	444	467	467	423	397
114	469	429	452	418	439	392	436	400
122	424	385	416	429	428	397	380	374
130	401	339	379	395	382	390	366	393
138	371	355	365	375	356	346	361	351
146	350	367	340	316	344	339	337	314
154	317	327	335	374	319	275	323	312
162	292	315	289	312	319	311	275	324
170	282	280	293	308	292	338	296	270
178	262	294	266	293	270	236	275	309
186	246	231	241	258	245	245	280	259
194	259	262	265	232	252	249	245	272
202	232	258	240	275	232	224	207	244
210	260	216	230	223	212	223	232	208
218	223	215	221	186	223	250	222	216
226	195	248	214	207	243	210	229	254
234	200	236	206	231	204	229	187	214
242	203	210	168	210	198	201	181	136
250	178	176	208	139	175	166	184	186
258	167	164	180	184	178	192	173	177
266	165	174	199	165	181	193	167	168
274	182	184	141	166	144	159	160	149
282	145	167	163	178	166	142	126	173
290	152	144	159	145	153	141	153	143
298	150	147	156	157	139	159	153	145
306	143	148	143	149	151	134	140	139
314	133	133	132	122	136	115	130	110
322	137	107	123	114	134	117	131	120
330	105	107	123	127	95	120	116	122
338	126	118	133	106	125	113	117	106
346	115	95	111	114	103	95	124	106
354	109	100	90	111	89	110	115	103
362	109	112	92	106	95	96	79	94
370	96	89	92	88	97	87	85	89
378	86	93	89	85	76	79	92	100
386	92	117	83	87	96	89	129	88
394	71	79	71	56	62	60	69	54
402	58	74	66	86	85	88	62	46
410	58	42	30	35	38	55	86	123
418	194	137	83	32	8	0	0	0
426	0	0	0	0	1	0	0	0
434	0	0	0	0	0	0	2	0
442	0	0	0	1	0	0	0	0
450	0	1	0	0	0	0	0	0
458	0	0	0	0	0	0	0	0
466	0	0	0	0	0	0	0	0
474	0	0	0	0	0	0	0	0
482	0	0	0					

DBG1 Random Spectrum 293°K, 0.1 μC

34	4364	4397	4250	4347	4148	4256	4172	3974
42	3874	3856	3732	3658	3580	3615	3632	3617
50	3517	3504	3516	3334	3317	3261	3298	3180
58	3215	3118	3187	3020	3032	2989	3019	2900
66	2942	2834	2879	2819	2828	2808	2765	2777
74	2598	2646	2690	2607	2561	2584	2447	2709
82	2570	2673	2473	2396	2394	2450	2356	2386
90	2300	2257	2316	2340	2272	2208	2260	2236
98	2230	2150	2109	2125	2173	2117	2244	2148
106	2088	2147	2114	2156	2106	2058	2095	2023
114	2048	1971	2052	1894	1909	1860	1916	1895
122	2037	1894	2058	1954	1943	1979	1962	1836
130	1867	1768	1767	1857	1831	1751	1884	1715
138	1812	1717	1724	1746	1663	1786	1765	1671
146	1620	1656	1710	1665	1626	1641	1664	1637
154	1692	1569	1676	1690	1633	1631	1638	1558
162	1637	1638	1552	1573	1517	1626	1535	1526
170	1565	1535	1575	1495	1525	1488	1458	1398
178	1492	1488	1511	1436	1427	1513	1384	1488
186	1428	1413	1465	1413	1427	1498	1388	1421
194	1374	1389	1378	1448	1454	1398	1374	1438
202	1399	1428	1324	1422	1405	1376	1394	1352
210	1311	1333	1318	1285	1287	1324	1318	1338
218	1336	1354	1266	1411	1355	1305	1269	1272
226	1280	1231	1323	1234	1296	1243	1251	1446
234	1202	1379	1312	1376	1245	1379	1198	1278
242	1191	1211	1182	1230	1153	1243	1151	679
250	805	840	895	738	759	779	907	1199
258	1176	1128	1177	1159	1148	1188	1158	1200
266	1165	1102	1184	1157	1129	1141	1116	1170
274	1105	1096	1124	1127	1108	1153	1147	1135
282	1097	1088	1076	1135	1110	1153	1114	1068
290	1155	1079	1109	1033	1021	1139	1091	1108
298	1051	1066	1049	1058	966	1035	997	1100
306	992	1066	1051	1045	1070	1065	1063	993
314	989	1105	1069	1055	1125	1010	1062	1033
322	1091	1036	976	1040	1024	1003	1068	1052
330	972	989	1039	1054	1020	946	1026	1021
338	989	927	1031	950	1055	974	1033	999
346	936	982	986	1009	960	1009	969	1023
354	974	1023	1007	1002	988	977	943	967
362	978	950	951	955	942	988	951	914
370	894	996	966	983	905	993	968	935
378	938	930	938	886	898	950	897	958
386	920	898	898	874	946	904	931	933
394	873	848	937	917	917	921	876	876
402	860	882	842	878	913	874	953	876
410	886	870	812	863	900	850	840	737
418	590	384	178	66	16	4	5	1
426	0	1	4	6	6	4	3	2
434	2	2	2	4	5	3	4	2
442	0	1	4	1	0	0	6	2
450	1	0	2	1	2	2	1	2
458	0	2	4	7	1	2	0	3
466	3	5	1	1	1	1	1	1
474	0							

DBG2 Aligned Spectrum (Virgin), 293°K, 0.095 μC

40	336	352	311	339	296	303	333	308
48	298	300	302	267	267	283	263	251
56	296	280	263	226	232	238	221	214
64	237	236	223	238	237	235	205	207
72	219	202	201	202	185	222	229	181
80	206	208	184	203	179	179	196	174
88	167	162	170	178	165	170	158	175
96	165	181	179	157	136	159	154	131
104	132	166	151	153	175	158	170	141
112	141	138	150	132	140	130	141	136
120	130	138	128	134	115	136	139	111
128	114	141	120	150	128	124	122	109
136	114	118	123	123	129	105	107	104
144	104	101	122	137	106	112	118	115
152	105	113	109	111	106	106	95	93
160	111	90	116	84	101	102	97	109
168	92	102	99	111	81	110	71	114
176	78	83	82	87	103	86	87	95
184	78	100	98	95	102	80	108	85
192	79	77	78	79	66	87	75	71
200	84	71	86	87	81	86	85	91
208	76	69	70	76	72	77	81	64
216	56	77	72	70	79	74	68	70
224	79	66	63	71	69	81	85	62
232	73	75	62	72	65	66	63	75
240	52	59	61	64	67	58	59	57
248	79	61	65	68	63	47	76	58
256	58	61	54	57	73	54	59	49
264	75	60	48	59	49	50	56	55
272	53	53	52	63	60	61	46	47
280	60	48	56	46	49	52	47	47
288	44	49	52	43	45	51	49	46
296	49	51	51	36	53	53	50	46
304	41	52	44	44	36	45	53	49
312	48	43	49	46	52	47	52	36
320	42	47	39	47	39	53	44	33
328	45	41	26	29	42	36	32	39
336	54	32	39	39	45	34	42	35
344	41	33	32	47	26	31	30	32
352	39	37	39	40	37	36	37	44
360	38	40	47	29	43	36	29	29
368	37	35	21	29	28	32	34	26
376	33	32	29	31	36	33	33	23
384	29	40	28	20	34	24	29	27
392	31	20	25	22	27	14	20	18
400	19	15	25	18	20	23	22	25
408	18	24	19	15	14	8	14	20
416	19	29	42	68	44	32	16	1
424	1	0	0	0	0	0	0	0
432	0	0	0	0	0	0	0	0
440	0	0	0					

DBG2 Aligned Spectrum, 52°K, 0.6 μC

34	948	876	880	858	807	829	803	803
42	773	760	710	724	725	719	690	632
50	684	676	672	646	644	605	585	582
58	565	558	567	572	602	544	519	583
66	577	520	520	493	498	502	489	497
74	502	519	495	483	455	398	533	441
82	467	479	440	433	389	383	433	391
90	404	414	429	411	402	372	378	417
98	392	374	385	395	378	377	383	347
106	338	352	340	369	336	341	374	356
114	327	349	292	357	322	324	326	292
122	320	289	282	305	304	290	285	289
130	282	318	300	312	286	289	299	271
138	270	284	298	263	276	245	264	252
146	275	259	229	268	273	263	245	241
154	237	273	247	210	222	273	241	267
162	256	233	240	229	237	209	204	250
170	227	208	229	233	189	207	209	237
178	211	242	206	240	225	220	203	198
186	212	194	213	183	214	223	205	201
194	232	187	230	180	159	181	199	177
202	180	215	188	186	201	192	195	197
210	183	169	178	181	181	153	171	186
218	158	196	172	202	163	163	169	160
226	167	182	156	185	160	176	177	167
234	169	188	156	150	158	178	155	134
242	160	138	172	166	177	164	175	146
250	118	156	131	149	136	132	132	139
258	141	140	115	141	136	137	145	163
266	155	140	140	127	133	134	143	121
274	136	125	140	129	135	120	127	135
282	130	146	126	110	138	125	125	122
290	109	132	134	121	116	147	124	115
298	133	119	130	119	129	113	118	131
306	117	115	110	123	131	97	126	118
314	116	110	111	103	115	112	139	123
322	110	129	113	104	125	103	114	102
330	105	91	130	117	109	134	120	96
338	127	106	105	99	108	102	102	118
346	111	88	79	90	95	109	119	97
354	103	101	108	93	111	123	95	89
362	107	100	102	81	93	87	85	92
370	106	103	94	100	83	106	116	97
378	89	88	93	96	128	96	108	112
386	93	105	90	91	71	83	67	61
394	41	53	49	32	20	41	39	31
402	23	37	32	33	44	54	53	54
410	25	43	30	25	22	20	54	100
418	149	197	136	57	21	5	1	0
426	0	0	0	0	0	0	0	0
434	0	0	0	0	0	0	1	0
442	0	0	0					

DBG2 Aligned Spectrum, 74°K, 0.3 μC

40	475	496	477	438	438	440	450	440
48	449	417	409	409	415	355	358	372
56	380	365	377	405	340	339	340	341
64	325	327	335	351	322	308	300	294
72	317	296	299	300	282	303	269	265
80	284	296	249	262	247	267	283	298
88	240	249	256	247	251	219	257	212
96	251	254	232	223	211	222	221	243
104	222	226	224	218	210	197	239	213
112	228	211	207	204	190	207	186	202
120	206	215	217	184	214	184	232	174
128	227	177	194	191	187	187	173	179
136	182	186	188	172	169	190	182	166
144	145	153	157	144	171	157	174	164
152	164	145	148	158	175	143	152	138
160	171	154	162	141	151	138	127	144
168	159	144	138	146	152	128	148	160
176	129	149	129	132	150	125	129	161
184	131	110	124	134	139	114	98	142
192	113	116	101	114	125	142	130	125
200	121	113	134	127	123	103	102	110
208	111	105	120	117	101	123	126	122
216	109	102	110	124	106	118	94	108
224	116	99	109	128	103	110	102	112
232	115	121	100	123	112	126	97	103
240	86	114	102	102	124	97	91	95
248	97	89	83	94	69	66	74	81
256	97	108	80	87	94	87	82	89
264	90	95	86	114	87	82	83	77
272	104	97	90	71	68	74	81	85
280	93	83	84	76	86	82	73	94
288	85	85	80	81	100	79	81	73
296	85	67	72	80	67	65	77	81
304	75	72	71	74	80	72	75	83
312	67	68	67	82	63	71	74	73
320	83	72	85	70	76	63	66	64
328	58	78	60	76	89	69	64	82
336	78	82	67	78	62	61	61	69
344	62	62	50	76	59	70	61	61
352	66	58	52	65	58	63	60	60
360	70	66	71	57	84	70	68	71
368	70	59	62	68	61	76	63	67
376	41	56	68	61	48	54	54	61
384	49	66	61	74	47	60	54	42
392	42	31	31	24	25	14	17	28
400	18	25	18	21	22	24	22	40
408	28	37	26	16	8	19	22	25
416	29	63	106	101	59	24	3	0
424	1	0	0	0	0	0	0	0
432	0	0	0	0	0	0	0	0
440	0	0	0	0				

DBG2 Aligned Spectrum, 114°K, 0.3 μC

31	691	663	625	621	612	648	617	592
39	532	549	532	545	547	527	515	477
47	483	498	470	454	486	453	504	449
55	486	441	427	449	445	431	398	435
63	397	396	396	388	421	394	370	379
71	362	391	363	329	350	340	315	360
79	324	312	310	313	342	314	277	313
87	275	297	280	285	277	298	279	282
95	263	278	295	274	244	246	259	278
103	244	282	271	233	268	275	250	231
111	250	255	256	226	238	222	245	225
119	232	235	266	253	211	213	219	244
127	222	208	203	191	201	206	210	193
135	186	194	241	218	182	197	219	188
143	208	193	199	188	181	199	195	184
151	173	180	205	172	195	196	166	189
159	175	214	206	180	165	162	200	186
167	169	167	183	188	158	167	160	164
175	129	169	151	160	170	145	139	140
183	142	155	163	147	134	148	148	121
191	148	162	144	159	156	145	141	128
199	140	126	135	147	150	146	138	139
207	138	135	139	131	124	130	136	117
215	139	128	118	118	119	153	136	131
223	139	110	120	114	108	118	98	109
231	116	113	112	129	132	106	119	117
239	117	118	105	91	113	118	111	99
247	105	103	86	77	93	101	82	77
255	80	82	94	96	107	106	108	127
263	106	96	98	95	93	100	97	100
271	90	88	101	109	87	102	103	102
279	96	87	94	81	73	89	91	90
287	91	69	89	92	80	97	87	75
295	86	79	84	84	70	102	66	94
303	94	94	67	92	69	88	76	68
311	72	88	72	83	77	87	81	76
319	63	89	82	68	75	72	85	78
327	65	78	65	89	74	68	83	77
335	83	82	68	64	63	66	64	66
343	69	69	62	86	65	72	67	59
351	66	73	73	56	63	74	69	69
359	74	70	62	57	67	77	63	54
367	63	63	66	68	73	66	56	55
375	56	53	59	59	73	61	50	69
383	54	78	53	56	53	75	59	64
391	65	51	40	47	39	29	23	22
399	35	25	27	22	20	22	38	31
407	32	43	29	25	19	17	14	14
415	30	32	76	132	94	74	26	4
423	0	0	1	0	0	0	0	0
431	0	0	0	0	0	0	0	0
439	0	0	0	0	1	0	0	0
447	0	0	0					

DBG2 Aligned Spectrum 187°K, 0.3 μC

31	956	938	946	937	912	931	901	863
39	910	861	774	770	801	742	758	764
47	769	702	740	737	691	687	658	660
55	703	667	647	615	649	633	600	600
63	561	563	570	541	544	535	567	549
71	571	501	528	522	495	515	462	508
79	493	483	522	483	522	476	466	487
87	455	427	437	438	463	437	446	405
95	392	450	404	404	424	413	442	418
103	370	405	391	388	387	336	328	350
111	345	392	360	387	351	359	354	369
119	332	315	366	350	317	327	333	329
127	319	351	314	314	320	299	295	291
135	330	317	299	284	292	277	291	279
143	284	280	274	297	279	259	249	276
151	294	277	257	259	233	278	264	264
159	259	257	240	243	235	264	248	230
167	257	236	228	220	224	216	222	248
175	203	229	248	232	213	217	221	209
183	246	212	202	190	243	236	205	207
191	239	216	211	199	218	201	223	206
199	201	220	201	201	188	187	201	175
207	166	168	225	186	198	172	179	192
215	178	174	177	162	177	164	180	168
223	173	169	158	178	166	170	163	144
231	166	167	186	179	184	171	151	171
239	169	181	175	166	144	147	167	140
247	151	130	110	122	133	129	102	136
255	111	154	153	154	163	155	131	136
263	127	135	150	141	138	133	127	120
271	142	148	118	105	148	131	119	124
279	121	122	136	130	131	137	127	127
287	113	119	123	125	121	125	129	130
295	119	120	106	114	114	97	114	126
303	116	105	101	128	105	110	104	105
311	108	104	117	100	109	101	114	118
319	112	100	99	106	105	100	107	107
327	94	94	118	101	96	115	112	130
335	136	104	108	95	99	92	108	103
343	89	121	105	83	79	81	84	96
351	88	93	99	71	69	89	95	98
359	87	79	83	87	84	82	71	86
367	99	66	98	68	68	71	78	80
375	81	81	91	77	86	79	63	56
383	76	75	78	63	69	93	58	71
391	63	71	54	60	56	47	50	35
399	32	38	35	36	31	47	53	60
407	53	48	42	40	31	32	34	26
415	35	54	127	146	131	82	33	6
423	1	1	0	1	0	0	1	0
431	0	0	0	0	0	0	0	0
439	0	0	0	0	0	0	0	1
447	0	0	0					

DBG2 Aligned Spectrum, 293°K, 0.3 μC

44	1025	1001	1032	1030	967	989	952	960
52	904	942	893	862	898	806	891	798
60	843	813	812	796	821	747	769	759
68	762	716	745	705	750	714	734	711
76	710	655	659	703	634	631	688	689
84	662	637	639	582	578	610	588	612
92	594	642	546	578	594	595	545	570
100	538	589	522	526	525	586	519	560
108	513	497	514	514	488	522	477	484
116	485	503	450	425	476	471	493	478
124	487	448	500	470	465	447	453	410
132	414	454	418	440	378	440	439	424
140	386	404	382	379	376	408	402	370
148	393	399	373	371	385	322	368	395
156	374	379	365	345	332	344	348	352
164	372	330	308	327	320	342	347	314
172	323	315	339	303	339	315	305	281
180	347	327	304	299	310	296	317	300
188	273	297	267	281	337	296	280	264
196	260	307	288	280	279	285	269	269
204	286	263	268	243	254	267	271	289
212	269	245	267	235	252	272	243	237
220	257	260	268	240	250	231	212	229
228	255	211	246	250	250	257	237	239
236	225	258	249	230	222	210	213	218
244	205	217	229	224	203	129	127	155
252	167	123	141	155	142	196	213	178
260	205	193	192	205	204	189	217	189
268	177	174	210	180	180	180	198	179
276	178	177	186	192	167	158	184	165
284	177	195	175	169	165	184	165	175
292	135	166	184	164	173	177	181	146
300	159	156	136	164	150	155	160	159
308	149	156	159	140	155	178	142	146
316	155	155	138	132	146	142	158	127
324	151	151	140	127	139	135	141	153
332	147	135	165	130	147	128	127	134
340	114	147	107	137	136	148	138	140
348	131	134	116	134	114	118	116	112
356	134	122	108	115	146	114	99	130
364	106	120	109	121	113	107	95	126
372	96	102	103	110	116	103	98	96
380	86	118	108	93	108	103	112	99
388	109	83	98	95	80	63	74	82
396	66	61	54	67	57	56	88	69
404	72	68	60	53	58	49	54	48
412	40	47	66	116	170	189	156	63
420	14	3	0	0	0	0	0	0
428	0	0	0	0	0	0	0	0
436	0	0	0	0	0			

DBG2 Random Spectrum, 293°K, 0.1 μC

31	4234	4158	3897	3924	3887	3804	3822	3901
39	3683	3702	3562	3452	3426	3379	3336	3322
47	3215	3169	3210	3126	3179	2999	2985	2898
55	2981	2977	2906	2709	2870	2785	2768	2686
63	2653	2573	2563	2474	2448	2515	2485	2456
71	2544	2451	2428	2393	2412	2464	2246	2252
79	2377	2253	2198	2256	2170	2210	2161	2217
87	2192	2078	2037	2164	1996	2084	2058	1992
95	2030	1988	1967	2024	1938	1932	1915	1889
103	1865	1955	1904	1935	1847	1784	1845	1839
111	1803	1768	1716	1823	1889	1784	1724	1761
119	1749	1645	1750	1781	1668	1702	1589	1692
127	1672	1659	1589	1570	1605	1717	1633	1664
135	1534	1590	1586	1571	1589	1567	1596	1578
143	1467	1511	1575	1534	1472	1428	1482	1496
151	1482	1501	1459	1458	1467	1390	1418	1383
159	1407	1429	1443	1422	1380	1353	1364	1362
167	1406	1380	1288	1359	1319	1304	1367	1345
175	1305	1387	1356	1347	1337	1409	1276	1281
183	1284	1252	1295	1308	1260	1268	1302	1329
191	1287	1252	1302	1226	1200	1189	1196	1246
199	1235	1251	1183	1243	1253	1198	1202	1176
207	1161	1214	1222	1226	1199	1236	1208	1220
215	1138	1164	1162	1134	1182	1137	1190	1155
223	1123	1153	1143	1177	1106	1102	1125	1131
231	1183	1120	1229	1167	1245	1082	1296	1087
239	1239	1085	1103	1118	1184	1106	1096	1072
247	1058	1075	904	961	1012	1028	877	878
255	866	1017	1014	1042	1044	1036	991	1046
263	1051	1024	1050	1124	971	1017	981	958
271	1024	1012	1011	997	1099	970	999	1095
279	990	938	995	952	996	986	981	981
287	970	1022	1003	1009	984	1000	956	1000
295	1023	951	1013	999	977	938	966	934
303	982	977	955	1014	995	988	989	948
311	953	967	966	914	935	949	933	939
319	970	924	898	966	925	976	950	926
327	890	869	886	910	949	919	898	908
335	917	921	876	923	944	897	920	853
343	893	902	873	947	860	890	882	824
351	878	948	829	859	899	893	928	875
359	860	863	889	888	853	905	786	868
367	855	881	845	828	907	845	900	837
375	858	838	863	863	863	849	818	832
383	869	830	864	805	840	818	808	833
391	793	786	810	827	751	804	817	777
399	798	816	795	761	824	786	774	741
407	813	792	757	787	719	779	776	769
415	761	681	580	370	193	64	16	6
423	3	4	5	3	5	2	2	3
431	5	2	2	5	4	3	2	6
439	2	2	2	1	3	3	0	1
447	1	4	3					

REFERENCES

1. Rol, P.K. et al., Proc. Fourth Inter. Conf. on Ionisation Phenomena in Gases. 257 (North-Holland, Amsterdam, 1960).

2. Davies, J.A. et al., Can. J. Chem. 38 1526 (1960).

3. Davies, J.A. et al., Can. J. Chem. 38 1538 (1960).

4. Piercy, G.R. et al., Phys. Rev. Lett. 10 399 (1963).

5. Piercy, G.R. et al., Can. J. Phys. 42 1116 (1964).

6. Lutz, H.O. and Sizmann, R., Phys. Lett. 5 113 (1963).

7. Dearnley, G., I.E.E.E. Trans. Nucl. Sci. NS-11 249 (1964).

8. Bøgh, E. et al., Phys. Lett. 12 129 (1964).

9. Thompson, M.W., Phys. Rev. Lett. 13 756 (1964).

10. Gemmell, D.S., Rev. Mod. Phys. 46 129 (1974).

11. Dearnley, G. et al., Ion Implantation (North-Holland, 1973).

12. Morgan, D.V., Channeling (Wiley, 1973).

13. Mayer, J.W. et al., Ion Implantation in Semiconductors (Academic, New York, 1970).

14. Lindhard, J., K. Dan. Vidensk. Selsk. Mat.-Fys. Medd. 34, Nr. 14 (1965).

15. Bonderup, E.H. et al., Rad. Eff. 12 261 (1972).

16. Björkqvist, K. et al., Rad. Eff. 12 267 (1972).

17. Campisano, S.U. et al., Phys. Lett. A 33 433 (1970).

18. Foti, G. et al., Phys. Rev. B 3 2169 (1971).

19. Behrisch, R. et al., Phys. Lett. A 35 181 (1971).

20. Pronko, P.P., Nucl. Instr. Meth. 132 249 (1976).

21. Picraux, S.T., J. App. Phys. 44 587 (1973).

22. Bohr, N., K. Dan. Vidensk. Selsk. Mat.-Fys. Medd. 18 Nr. 8 (1948).

23. Schiøtt, H.E. et al., Atomic Collisions in Solids Vol. 1, 843 (Plenum, N.Y., 1975).

24. Pederson, M.J. et al., Atomic Collisions in Solids Vol. 1, 863 (Plenum, N.Y., 1975).

25. Merkle, K.L. et al., Phys. Rev. B 8 1002 (1973).

26. Nelson, R.S. and Thompson, M.W., Phil. Mag. 8 1677 (1963).

27. Bøgh, E., Can. J. Phys. 46 653 (1968).

28. Ziegler, J. and Andersen, H., Private Communication.

29. Kane, P., and Larrabee, G., Characterization of Solid Surfaces, (Plenum, New York, 1974).

30. Lonsdale, K., Acta Cryst. 1 142 (1948).

31. Cullitty, B.D., Elements of X-ray Diffraction (Addison-Wesley, Massachusetts, 1956).

32. Newman, R.C. and Pashley, D.W., Phil. Mag. 46 927 (1955).

33. Heidenreich, R.D. and Shockley, W., Report of a Conference on Strength of Solids, 57 (Phys. Soc., London, 1948).

34. Davies, J.A. and Swanson, M.L., Chalk River N. L.

35. Swanson, M.L., Private Communication.

36. Practical Methods in Electron Microscopy, Vol. 1, (ed. A.M. Glaubert, North-Holland, 1972).

37. Seeger, A., Theory of Crystal Defects, 37 (ed. B. Gruber, Academic Press, 1966).

38. Cottrell, A.H., Dislocations and Plastic Flow in Crystals (Oxford, 1963).

39. Barrett, J.H., Phys. Rev. B 3 1527 (1971).

40. Barrett, J.H., Atomic Collisions in Solids, Vol. 1, 841 (Plenum, New York, 1975).

ADDENDUM

In the discussion of the calculations using the SITE approximation, we considered certain parameters ($E_{\perp_c}$ and C) used in the calculation and also the applicability of using $p(E_{\perp_o})$ to describe the initial transverse energy distribution. However, we did not discuss the derivation of the expressions used in the calculation of $\langle dE_\perp/dz \rangle$, which were approximated by Lindhard[14] and Foti et al.[18]

The dominant term in $\langle dE_\perp/dz \rangle$ is $\langle (dE_\perp/dz)_n \rangle$ for high transverse energies, as can be seen in Figures I.1(a) and III.1.

$\langle (dE_\perp/dz)_n \rangle$ is given by $\frac{d}{4E}\langle \delta\vec{K}(r)^2 \rangle$ and Lindhard gives

$$\langle \delta\vec{K}(r)^2 \rangle = \frac{\rho^2}{2}\left\langle \frac{K^2(r)}{r^2} + K'(r)^2 \right\rangle \quad \text{, see Equation (III.8).}$$

This was derived by summing the squares of the momentum transfers (corresponding to the $\delta\vec{K}$ values) along the path of the particle and expanding to the lowest contributing order in s/r, where $\vec{s}$ is the distance of a thermally-displaced atom from its static position.

The Aarhus group[23] has extended the calculation to include the next contributing order of the force fluctuation, with the averaging again taken over the distribution in the thermally displaced string atoms, $P(\vec{s})$, and over the positions $\vec{r}$ in the area accessible to particles of transverse energy $E_\perp$.

When these first two contributing terms are added to give a new value for $\langle (dE_\perp/dz)_n \rangle$, and this is used to modify the calculated Random

Fraction versus depth spectrum, then the calculated and measured Random Fraction versus depth spectra are found to be in good agreement, see Figure AD.1.

Hence the gold single crystals, which we have prepared, show all the dechanneling characteristics of well-ordered defect-free gold as expected from theory.

Figure AD.1.

Calculated (— Lindhard's E_{1c}), (- - - Barrett's E_{1c})
and Measured Random Fraction Spectra.